Advances in Axial Motion-like Artefact correction in Optical Coherence Tomography Imaging

by

Adrian Fernandez Uceda

A thesis presented for the degree of

Doctor of Philosophy

Applied Optics Group

School of Physical Sciences

University of Kent

July 2024

Declarations

The contents of this thesis, titled "Advances in High Resolution Optical Coherence Tomography Imaging of Moving Targets", have been composed by the author, Adrian Fernandez Uceda, and performed under the supervision of Prof. Adrian Gh. Podoleanu. I declare that:

- The work was done wholly or mainly while in candidature for a research degree at this University.
- No content has been submitted for the purposes of a qualification at any other institution or for any other degree.
- Where I have consulted the published work of others, this is always clearly attributed.
- Where the thesis is based on work done by myself jointly with others, I have made clear exactly what was done by others and what I have contributed myself.
- The author is listed as one of the co-inventors for a patent in the name of the University of Kent derived from the work presented in the Chapter 4

Last corrections accepted in February 2026.

Abstract

Since its development back in the 1990s, Optical Coherence Tomography (OCT) has been an invaluable tool for biomedical imaging, more so in the area of ophthalmology, thanks to its ability to retrieve structural information from within a scattering sample in a non-destructive, non-invasive, and contactless way. Nonetheless, in order to fully comprehend the nature of a biological sample, it must be studied in its own environment, or *in-vivo*, and as most living things, they are susceptible to motion.

This thesis focuses on different approaches and advances performed in motion detection and correction from three different points of views, starting from artefacts due to the motion of the device used for imaging, followed by the artefacts caused by the motion inherent to the sample, to finalise with a different type of artefact caused by the internal movement of the imaging system. Within these pages, different set-ups are presented, all working in the near infrared part of the optical spectrum.

For the first point of view, motion caused by the displacement of the device, this thesis presents results obtained in an endoscopic set-up, in which the optical probe can be moved by the hand of the operator or using some mechanically actuated endoscope. In the case of the second point of view, the device employed consists on a free space Swept Source OCT (SS-OCT) in two different configurations, one described for skin applications, called configuration (s), and a second one described for ophthalmology applications, referred as configuration (e). These same configurations, except for the removal of a dichroic filter, are the ones explored in the third point of view, pairing the optics from the SS-OCT system with an extra swept source. The final study presented in this thesis led to another application, described in the same chapter, to characterise the sweeping direction of any swept source in an indirect way.

Acknowledgments

This journey of a PhD has not been what I would have imagined, from the isolation of leaving my home town, to a global pandemic in between disrupting so many lives and work in between and the ups and downs of the mental health struggles that nowadays seem to become part of most of us. That being said, I wouldn't have changed it for anything else, while these times may have been a challenge, the support and love of all of you have kept me afloat, so as it is commonly said in these type of acknowledgments, none of this would have been possible without any of you. My lack of sleep of these days might make me forget some names, but even if yours is not here, you still have been invaluable to me.

Firstly, I'd like to thanks my main supervisor, Professor Adrian Podoleanu, who not only watches over the AOG as a research leader, but sometimes almost like a father figure. I know I have gotten in your nerves many times, but I hope to return back all those sleepless nights.

And how not to mention all the rest of the Applied Optics Group, specially eternal helper and jack-of-all-trades, in-and-out of the lab, and recently promoted to lecturer (not any longer colleague then?), Dr. Manuel J. Marques, followed by the rest of lecturers and postdocs of the group, starting with the sole UK representative Dr. Mike Hughes followed by the romanian delegation at front formed by Dr. Adrian Bradu, Dr. George Dobre, Dr. Ramona Cernat, and Dr. Radu Stancu. Special thanks go to my fellow students, some of them now doctors, beginning with the frenchman who made me start thinking positively of France, Julien Camard, while we haven't been writing our theses at the same time, our shared pain was a helpful resting place, our paths might be in different places now, but I won't forget any of the every day shenanigans that so much life gave me. It is a common joke in many places to blame or complain about the french, so parisians can be the target of double trouble. They clearly didn't met Sacha Grelet, for if his friendliness and charisma were synonyms of France, we would need to find a different country to joke about. Also thanks to Lucy Abbott, whose passion for aircrafts, making her ran for the ocassional B-52 flying around, taught me the craze of flightradar. And Dr. Marco Santopietro, your arrival may have been one of the most recent ones to photonics, yet I feel like I've known you for years. I may not join your dancing cult ever, but I hope to get to see all your steps in this dancefloor we call office.

I must change paragraph to be able to keep track, but can't leave out the wonderful Taylor Sanderson. Few times in my life I've met people with such a calm capacity to support and help in any day or moment, I swear one day I'll follow instructions properly and understand minimally a car. And through him, Chiara Kawohl, the vampire with near perfect sense of smell who has been a special glue outside of the labs, thank you both for so much every day. And while he hasn't have a picture on the wall yet, also special mention to Josh Fennell, who every time I think I've got him and his chill, a new story or moment comes up that breaks his good old grandpa vibes into one of the wildest stories I've heard. While the czech delegation has been probably the most variable in numbers of them all, special thanks goes to Rene Riha, theoretician expert in lasers who still has to find a way to implement them in ice hockey. And not for being last is less important, quite the opposite, special thanks to Dr. Alejandro Martinez Jimenez, the spaniard who has brought back the sun and warmth that I ever missed from home. Since I arrived I tried to avoid spaniards, and yet there you went and shattered that thought. Your chill and calmness may have been absent while dominating the road on your car, but you have become almost a role model to my everyday life.

Those are the ones who remain, but can't forget either those who already left. Specially Dr. Sophie Caujolle, who while I keep forgetting to reply to her messages, awaits eager the day that I pass my viva so my hair gets its fateful meeting with a pair of scissors. Also thanks to my buddy, Dr. Andrew Thrapp, who while we started together, his impressive pace was impossible for me to keep up with and showed that America is more than guns and freedom, is also the land of Dr. Pepper and Pepsi Max. And not to forget Gianni Nteroli, whose passion in life and research are of admiration and with whom I regret not being able to spend more time before the pandemic. Finally, also thanks to Dr. Mike Everson, whose skills in the lab are only met by his skills developing maps for doom, and Hal Dorrington, our always free spirit of the labs.

In the personal side, I want to give special thanks to my partner, my other 3 legs of the table, Cassie Haughton-James. If anyone could be more central to getting past this ordeal, is definitely you. Words can't convey how helpful you have been for every part of my being. Thank you so much for every single day, Rakastan sua. And thanks also to your family, who has become a second home in a foreign country, literally during the darkest times of the pandemic, and for accepting me as one of your own. You have all given me a new place to call home.

And my friends, at the other side of the sea, with the front lead taken by my best friends Antonio Benito, Carlos Garcia y Pedro Gullon, you three have been my most important link back home, one never removed neither by kilometres nor by data streams, surviving in the shape of virtual boats and digging nightmares. I miss every day not being able to just join for a beer or simply walking around. One day we'll travel together to Japan, that trip that has been thought thousand times and never fulfilled.

Last but not least, special thanks to my family, my parents, Maria del Carmen Uceda Grela and Luis Miguel Fernandez Lopez, and my siblings, David and Ruben. I wouldn't be an inch of who I am today if it wasn't for all the nurture and growth that you all instilled on me. Thank you so much for having shown me how a person should be and for being my moral compass in any kind of waters, I love you all.

As I said before, I'm leaving so many people behind, the list would never end, specially from people back in Spain, but the sleep deprivation takes a hold on me, and the same way I kept putting off finishing, I need to end the acknowledgments at some point! So while it may be underwhelming to finish this section like this, I'll thank you all in person.

Thesis outline

With Optical Coherence Tomography (OCT) being already established as a non-invasive, contactless imaging technique with results akin to those of a biopsy, hence referred sometimes as an optical biopsy, more and more developments in high resolution systems appear in both research and medical settings. While extremely high speed has been reported at higher wavelengths, at 850 nm most sources are still behind, either due to the sensors or to technicalities in the manufacturing of the swept source, which leaves OCT open to motion artefacts when these are not accounted for.

In this thesis I approached the study and correction of motion artefacts in the axial axis from three different point of views, starting for the artefacts generated due to the translation of the field of view of the OCT across the sample, followed by the artefacts generated by the inherent motion of a living sample, such as the eye, and then finishing with axial distortions that present themselves in the same fashion as those before, but that are not generated by the translation of either the sample or the system. Instead, these final distortions are generated by the design of the detection system paired with a scanning laser.

Organisation of the thesis

This thesis is divided into 6 chapters, with chapters 1 and 6 being a brief introduction and a brief future work sections respectively, chapter 2 being the main theory chapter, and chapters 3, 4 and 5 being the experimental chapters in which my personal work has been described. Each chapter is described more in depth below:

- Chapter 1: This brief introduction presents a few snippets of the origins of biological imaging and OCT, as well as the concept of "biological window", and the narrative link between the chapters, being centred in axial motion artefacts.

- Chapter 2: While throughout the experimental chapters, the main imaging modality of OCT used was Master-Slave OCT (MS-OCT), introduced in 2013, in this chapter the main theory behind the main different modalities of OCT as well as MS-OCT is presented: Time Domain OCT, Spectrometer Based OCT, and Swept Source OCT. There is also a description of Point Scanning OCT and Full Field OCT.

- Chapter 3: As the first chapter in the experimental section, this chapter comprises the results of the paper "Endoscopic en-face optical coherence tomography and fluorescence imaging using a correlation-based probe tracking"[1], in which a novel image stitching algorithm was presented being applied to a dual-clad OCT/fluorescence endoscope designed for lung imaging. While the peer reviewed paper that this chapter was developed from was written in collaboration with several other authors, my contributions were mainly on the Region of Interest (ROI) positioning, evaluating different strategies for compensating the axial motion of the probe, as well as testing, characterising, and finishing the assembly of the dual OCT/fluorescence imaging system. As the ROI was an initial necessary step for the stitching algorithm, a brief description of the whole algorithm was included.

- Chapter 4: In this chapter I expanded upon the results presented in the conference proceedings "Non-mechanical Axial Motion Compensation using Master-Slave Optical Coherence Tomography" [3]. Here I present an OCT system paired with an extra interferometer for axial tracking, referring the imaging components as Imaging Sub-system (IS) and the tracking interferometer as Tracking Sub-system (TS). Both IS and TS share part of their sample arms, with the IS operating at 850 nm and the TS at 1300 nm. The conjugation of these two sub-systems was tested for two configurations: one for skin imaging and other for retinal imaging.

- Chapter 5: The peer reviewed paper "Spatial distortions in swept source optical coherence tomography due to lateral scanning" [3] was used for this section. Here a type of artefact is described and analysed, seemingly missed by the OCT community so far, in which a swept source OCT paired with a point scanning approach experiences a deviation in the axial position related to the scanning speed. Experiments with both unidirectional and bidirectional swept sources are presented, in both retinal imaging and skin imaging configurations, as they are the most common interface optics present in OCT devices. The distortions discussed in this chapter seem to be a result of the rate of variation of OPD across the scanning direction, paired with the sweeping speed and direction of the swept source.
- Chapter 6: In this brief section I mention possible avenues of future work that could stem from the previously reported work, mainly from the chapter 5.

Thesis outputs

The publications resulting from the research carried through my PhD programme are listed below, and as previously mentioned in the organisation of the thesis, each chapter is linked to a publication. The chapter 4 is also linked to a patent, US 2021/0145285 A1, with Prof. Adrian Podoleanu. Through the course of the PhD programme, I attended different conferences, such as the Biophotonics conference in Florida in 2020 (online, due to the pandemic), the international day of light talks organised in Madrid, Spain, in 2022, and CRATER in Poland in 2023. I also participated in the organisation of a student led conference Optics and Photonics for Scientific Progress (OPSP) in 2021, organised jointly with the University of Surrey and backed by both Optica and South-East Physics Network (SEPNet), organised several industrial visits through the Optica Student Chapter at Kent, and participated several outreach events. I also participated in demonstrating labs in physics and programming as part of my PhD agreement with the University of Kent.

Peer-reviewed articles published during the course of the doctoral programme

1. Marques, Manuel J. and Hughes, Michael R. and **Fernandez Uceda, Adrián** and Gelikonov, Grigory and Bradu, Adrian and Podoleanu, Adrian ”Endoscopic en-face optical coherence tomography and fluorescence imaging using correlation-based probe tracking”, *Biomed. Opt. Express*, Vol. 13, Issue 2, February 2022.
   DOI: https://doi.org/10.1364/BOE.444170

2. **Fernandez Uceda, Adrián** and Venugopal, Gopika and Podoleanu, Adrian ”Spatial distortions in swept source optical coherence tomography due to lateral scanning,”, *Opt. Express*, Vol. 32, Issue 13, June 2024.
   DOI: https://doi.org/10.1364/OE.520099

Peer-reviewed conference proceedings

3. **Fernandez Uceda, Adrián** and Marques, Manuel J. and Bradu, Adrian and Podoleanu, Adrian, ”Non-mechanical Axial Motion Compensation Using Master-Slave Optical Coherence Tomography”, in *Biophotonics Congress:*

Biomedical Optics 2020 (Translational, Microscopy, OCT, OTS, BRAIN), OSA Technical Digest (Optica Publishing Group, 2020), paper OTu1E.6. DOI: https://doi.org/10.1364/OCT.2020.OTu1E.6

4. E. A. Proano Grijalva, A. Martínez Jiménez, A. Bradu, **A. Fernandez**, B. O. Meyer, A. Jensen, E. Semenova, T. Ansbæk, K. Yvind, A. Podoleanu, "Novel 1.6 MHz swept source for real-time volumetric in-vivo OCT imaging of the human retina," Proc. SPIE 12367, Optical Coherence Tomography and Coherence Domain Optical Methods in Biomedicine XXVII, 1236704 (8 March 2023); https://doi.org/10.1117/12.2649142

Non peer-reviewed conference presentations

5. "Endoscopic en-face optical coherence tomography and fluorescence imaging using correlation-based probe tracking" - Conference on Recent Advances in Translational Eye Research (CRATER) 2023 - Warsaw, Poland, September 2023.

6. "Quietud en una vida móvil: compensación de movimiento en OCT", International Day of Light talks organised by the Univesidad Complutense de Madrid. 18 of May 2022.

7. Optics and Photonics for Scientific Progress (OPSP) 2021. Student-led conference organised jointly by the Optica Student Chapters of the University of Kent and the University of Surrey, sponsored by Optica and by the South-East Physics Network (SEPNet). Held online on the 13 and 14 of April in 2021 due to the pandemic.

8. International Optica Network of Students (IONS) held at the Institute of Photonic Sciences (ICFO) in Barcelona, Spain, on the 26-29 of June 2019.

---

9. IV International School on Light Sciences and Technologies (ISLIST) organised by the Universidad Internacional Menendez Pelayo in Santander, Spain, on the 17 - 21 June 2019.

Contents

Chapter 1

Introduction

Ever since the invention of the first compound microscope by the end of the 16th century [1], humankind has been looking into the structure of living matter, with the first inert cell being discovered in 1665 [2] and the first living algae cells reported in 1674 [3]. Early microscopy required the slicing of the material under examination and the first roadblocks encountered revolved around the understanding of optics and aberrations. It was thanks to the technological advances of the 19th and 20th centuries when the first look into the living body occurred, with the first X-ray of a human hand in 1895 [4]. Before the first X-ray, all medical devices investigated ex-vivo images, and while x-ray allowed in-vivo imaging, these were still invasive due to the high levels of radiation required for imaging.

With the invention of the laser in 1960 [5], optical imaging gained a new momentum, with the development of the first laser scanning microscope in 1969 [6] used just 2 years later, in 1971, to image biological samples [7]. Motivated by a desire to obtain a non-invasive imaging system, by mid-1970s start appearing the first research in optical reflectivity that eventually led to the creation of Optical Coherence Tomography (OCT) in 1991, with also the first OCT image of a human retina [8]. OCT images obtain the depth profile of the sample, and by scanning through an area, reconstruct a full volume.

The retrieval of depth information from a sample is related to its capacity to absorb and scatter the radiation employed. In order to reach deep into biological samples, the wavelength of the optical imaging device is selected accordingly to low levels of absorption, which is determined by the composition and structure of the sample under investigation. This leads to the so-called "biological window", a region of the light spectrum in which the main components of biological samples present minimal absorption.

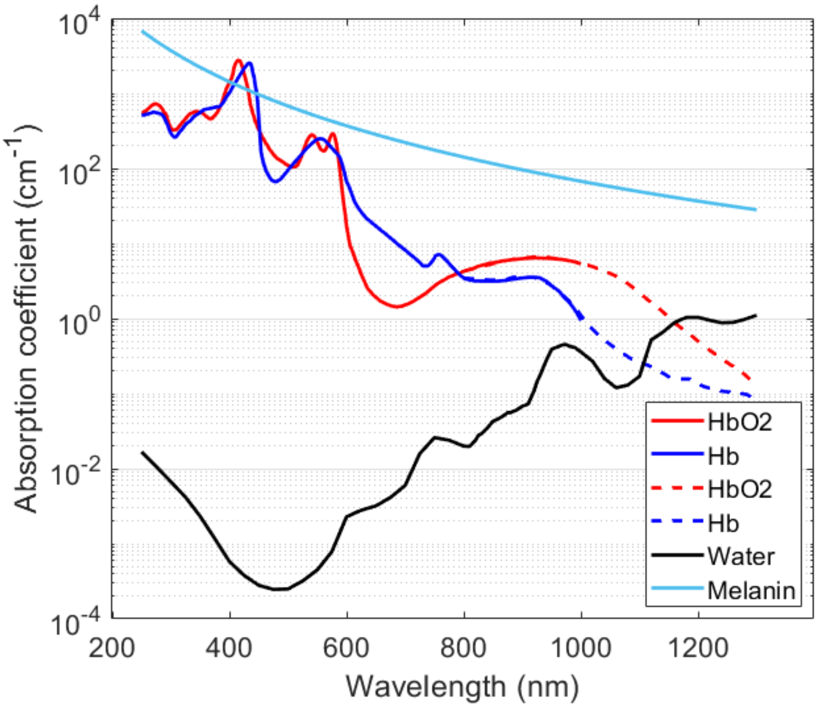

Figure 1.1: Adapted graph of absorption coefficients of a generic tissue from Scott Prahl and Steve Jacques [9]. The components of the tissue have been reduced to oxyhaemoglobin (HbO2), deoxyhaemoglobin (Hb), water and melanin between 250 and 1300 nm.

Fig.1.1 presents some of the main elements that contributes to light absorption in biological tissues. These elements are the two variations of haemoglobin [10, 11], oxyhaemoglobin (HbO2) and deoxyhaemoglobin (Hb), water [12] and melanin [13]. Depending on the idiosyncrasies of the imaged tissue, the best wavelength for imaging might vary, but the biological window is defined between 600 nm and

1300 nm [14].

In-vivo imaging allowed for new levels of understanding, but living tissue tends to present motion artefacts. In certain cases, motion can be fixed, but some tissues have their motion linked to their function, such as lungs, heart and eyes. This can lead to different type of artefacts in the retrieved image, both laterally and axially. In other cases, the field of view (FOV) of a system might be small, and the device requires to be moved across the sample to analyse large regions, therefore motion artefacts can appear even if the sample is stationary. Analysis and correction of motion artefacts has been studied almost since the first OCT image, with the first reports of corrected images dating back in 1993 [15].

In general, there are two ways to approach motion artefacts. A first approach consists on increasing the acquisition speed, which enables the retrieval of information before the motion has occurred, removing the need to compensate for it. Another approach is to analyse the nature of the artefacts presented in the image, and correct them appropriately, either post acquisition, or mechanically adjusting the device so that the device moves in sync with the sample.

In this thesis, we explore the second approach, evaluating the nature of the artefacts in three separate scenarios, with my work focusing on those artefacts created along the z axis: firstly, when a probe or device is translated across a stationary sample; secondly, when the motion artefact is inherent to the sample; and thirdly, when the artefact along the z axis is produced by a secondary effect related to the nature of the laser source and imaging method employed, even when both the device and the sample are stationary.

References

1. Ball, C. S. The Early History of the Compound Microscope. *Bios* **37,** 51–60. ISSN: 00053155. `http://www.jstor.org/stable/4606667` (2024) (1966).
2. Hooke, R. *Micrographia* `https://books.google.co.uk/books?id=0DYXk_9XX38C` (London: Royal Society, 1665).
3. Cocquyt, T. Positioning Van Leeuwenhoek's microscopes in 17th-century microscopic practice. *FEMS Microbiology Letters* **369,** fnac031. ISSN: 0378-1097. eprint: `https://academic.oup.com/femsle/article-pdf/369/1/fnac031/44371863/fnac031.pdf`. `https://doi.org/10.1093/femsle/fnac031` (Mar. 2022).
4. Glasser, O. WC Roentgen and the discovery of the Roentgen rays. *AJR. American journal of roentgenology* **165,** 1033–1040 (1995).
5. Rawicz, A. H. *Theodore Harold Maiman and the invention of laser* in *Photonics, Devices, and Systems IV* (eds Tománek, P., Senderáková, D. & Hrabovský, M.) **7138** (SPIE, 2008), 713802. `https://doi.org/10.1117/12.817966`.
6. Davidovits, P. & Egger, M. D. Scanning laser microscope. *Nature* **223,** 831–831 (1969).
7. Davidovits, P. & Egger, M. D. Scanning Laser Microscope for Biological Investigations. *Appl. Opt.* **10,** 1615–1619. `https://opg.optica.org/ao/abstract.cfm?URI=ao-10-7-1615` (July 1971).

8. Huang, D. *et al.* Optical Coherence Tomography. *Science* **254,** 1178–1181. eprint: `https://www.science.org/doi/pdf/10.1126/science.1957169`. `https://www.science.org/doi/abs/10.1126/science.1957169` (1991).
9. Scott Prahl, Steve Jacques. *Generic tissue optical properties* `https://omlc.org/news/feb15/generic_optics/index.html`. 2015.
10. W. B. Gratzer, N. Kollias. *Blood spectra for oxy- and deoxy- whole blood (150 g hemoglobin/liter)* `https://omlc.org/spectra/hemoglobin/summary.html`. Data compiled by Scott Prahl. 1998.
11. Suzaki, H. *et al. Noninvasive measurement of total hemoglobin and hemoglobin derivatives using multiwavelength pulse spectrophotometry -In vitro study with a mock circulatory system* in *2006 International Conference of the IEEE Engineering in Medicine and Biology Society* (2006), 799–802.
12. Hale, G. M. & Querry, M. R. Optical Constants of Water in the 200-nm to 200-μm Wavelength Region. *Appl. Opt.* **12,** 555–563. `https://opg.optica.org/ao/abstract.cfm?URI=ao-12-3-555` (Mar. 1973).
13. Jacques, S. L. & McAuliffe, D. J. THE MELANOSOME: THRESHOLD TEMPERATURE FOR EXPLOSIVE VAPORIZATION AND INTERNAL ABSORPTION COEFFICIENT DURING PULSED LASER IRRADIATION. *Photochemistry and Photobiology* **53,** 769–775. eprint: `https://onlinelibrary.wiley.com/doi/pdf/10.1111/j.1751-1097.1991.tb09891.x`. `https://onlinelibrary.wiley.com/doi/abs/10.1111/j.1751-1097.1991.tb09891.x` (1991).
14. Huang, Y.-Y., Chen, A. C.-H. & Hamblin, M. Low-level laser therapy: an emerging clinical paradigm. *SPIE Newsroom* **9,** 1–3. `https://www.spie.org/news/1669-low-level-laser-therapy-an-emerging-clinical-paradigm#_=_` (2009).

15. Swanson, E. A. *et al.* In vivo retinal imaging by optical coherence tomography. *Opt. Lett.* **18,** 1864–1866. `https://opg.optica.org/ol/abstract.cfm?URI=ol-18-21-1864` (Nov. 1993).

Chapter 2

Optical Coherence Tomography (OCT)

Author's note: All the theoretical calculations and formulas showcased in this chapter have been extracted from two well known books, the latest edition of the three volumes of "Optical Coherence Tomography: Technology and Applications" books from Drexler and Fujimoto [1], and "Biomedical Optics: principles and imaging" from Wang and Wu [2], with the nomenclature being adapted as needed. Cites have been added wherever papers have been used rather than these books.

2.1 Introduction to OCT

Optical Coherence Tomography (OCT) is a contactless, non-invasive imaging technique based on interferometry that allows to retrieve depth information from a given sample, similar to a biopsy, in a non-destructive way. OCT owes its origins to the Michelson interferometer back in 1881 [3], in which the light of a broadband source is split in two different paths, one in which light reaches a mirror at a known distance from the splitting point, z_r, and is reflected back, and another path in which the sample under investigation is placed. The first path is the reference arm and the second is the sample arm. The back-scattering points within the sample will each reflect light back through the arm, each traversing an optical distance z_s, and recombine with the light reflected from the reference arm into a detector.

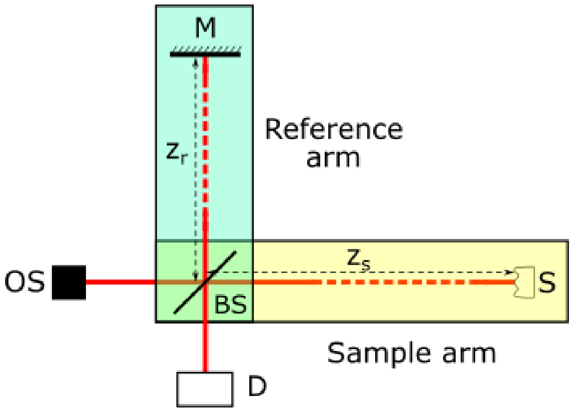

Figure 2.1: Schematic representation of a simple Michelson Interferometer. In light blue the reference arm is marked, and in light yellow the sample arm is highlighted. Both arms are measured from the beamsplitter. BS: Beamsplitter; D: Detector; M: Mirror; OS: Optical Source; S: Sample; z_r: Reference arm distance from BS to M; z_s: Sample arm distance from BS to S.

In Fig. 2.1 a basic Michelson interferometer is depicted, in which z_r and z_s are depicted. No optical elements apart of the beamsplitter (BS) have been represented, as the principle for the interferometer is valid for any design. The light from the optical source (OS) is drawn in red, with the discontinuity segments representing a length that might be different than the one depicted.

Each refractive index change inside a sample constitutes a scattering point, thus existing an electric field reflectivity profile dependent on depth inside the tissue $r_s(z_s)$. In real case scenarios, this $r_s(z_s)$ profile is continuous, but for ease of explanation, we will consider a discrete scenario, in which the changes occur only at specific distances inside the sample N times according to the equation:

$$r_s(z_s) = \sum_{n=1}^{N} r_{s_n} \delta\left[(z_s - z_{s_n})\right] \tag{2.1}$$

Where δ refers to the Dirac delta function, due to the scattering points being considered discrete. The focus of OCT is on the reconstruction of the function $r_s(z_s)$ out of the measured interferometric signal, whose square modulus $|r_s|^2$ corresponds to the power reflectivity of each reflector R_s so that $r_s(z_s) = \sqrt{R_s(z_s)}$. Given a complex electric field by:

$$E_i = s(k,\omega)e^{i(kz-\omega t)} \tag{2.2}$$

Where $s(k,\omega)$ is the electric field amplitude as a function of the wave number $k = 2\pi/\lambda$ and the angular frequency $\omega = 2\pi v$, the electric field affected by the scattering points defined by eq. 2.1 would be:

$$E_s = \frac{E_i}{\sqrt{2}}\left[r_s(z_s) \circledast e^{i2kz_s}\right] \tag{2.3}$$

In which $\circledast$ represents convolution, the term $-\omega t$ has been removed considering $t = 0$ and the factor of 2 in the exponential refers to the round trip in the arm between the beamsplitter and the sample under examination.

The interference experienced at the detector by the convergence of the waves from the reference, E_r, and the sample arm, E_s, will be proportional to the square sum of the incident fields, described as:

$$\begin{aligned} I_D(k,\omega) &= \frac{\rho}{2}\langle |E_r + E_s|^2 \rangle \\ &= \frac{\rho}{2}\langle (E_r + E_s)(E_r + E_s)^* \rangle \\ &= \frac{\rho}{2}\left\langle \left| \frac{s(k,\omega)}{\sqrt{2}} r_r e^{i(2kz_r - \omega t)} + \frac{s(k,\omega)}{\sqrt{2}} \sum_{n=1}^{N} r_{s_n} e^{i(2kz_{s_n} - \omega t)} \right|^2 \right\rangle \end{aligned} \tag{2.4}$$

Expanding eq. 2.4 the terms related to ω cancel each other, reducing to $I_D(k,\omega)$ to I_D being only dependent on k, $I_D(k)$, so that:

$$\begin{aligned} I_D(k) =& \frac{\rho}{4}\left[S(k)\left[R_r + R_{s_1} + R_{s_2}...\right]\right] \quad \text{"(A)"} \\ &+ \frac{\rho}{2}\left[S(k)\sum_{n=1}^{N}\sqrt{R_r R_{s_n}}\left(\cos\left[2k(z_r - z_{s_n})\right]\right)\right] \quad \text{"(B)"} \\ &+ \frac{\rho}{4}\left[S(k)\sum_{n \neq m=1}^{N}\sqrt{R_{s_n} R_{s_m}}\cos\left[2k(z_{s_n} - z_{s_m})\right]\right] \quad \text{"(C)"} \end{aligned} \tag{2.5}$$

Where $S(k)$ corresponds to $\langle |s(k,\omega)|^2\rangle$ and represents the power spectral dependence of the light source [4]. In eq. 2.5 we can observe 3 distinct components, labelled as (A), (B) and (C) in the equation, that corresponds to the DC, Cross-correlation and Auto-correlation respectively. The DC term does not depend on the interference, just on the power associated with each reflector individually. The Cross-correlation corresponds to the interference component between reference and sample arm, being this part of the equation the one OCT uses to reconstruct the reflectivity profile of the sample in most designs. The Auto-correlation term is obtained by the self interference of the different waves coming from different layers within the sample, being considered artefacts or noise in some setups, while in common-path interferometers it is the interference signal used for the reconstruction of the sample.

Upon further analysis of $S(k)$, most sources used in OCT presents either a Gaussian or a square profile for their spectrum shape. As Gaussian profiles are more common, $S(k)$ and its inverse Fourier transform, $\gamma(z)$, are represented by the equation:

$$\gamma(z) = e^{-z^2\Delta k^2} \overset{F}{\longleftrightarrow} S(k) = \frac{1}{\Delta k\sqrt{\pi}} e^{-\left[\frac{k-k_0}{\Delta k}\right]^2} \tag{2.6}$$

Simplifying the scenario to a single reflection from the sample and a monochromatic light and applying eq. 2.5, the component E_i can be expressed as E_0 as no dependencies are present in k nor ω, and the intensity observed by the detector employed in the system can be simplified to the expression:

$$I = E_{r0}^2 + E_{s0}^2 + 2E_{r0}E_{s0}\cos\left(2\pi n 2(z_s - z_r)\right) \tag{2.7}$$

Where $2\pi n$ in the phase difference corresponds to the propagation constant along the arms, assuming both arms in the same medium, where n is the refractive index of the medium. Any intensity variation will depend solely on the mismatch between the distance travelled by the light on each arm, called Optical Path Difference (OPD) as:

$$OPD = 2n\Delta z = 2n\left(z_s - z_r\right) \tag{2.8}$$

When the OPD approaches 0, the interference will result on a maximum. Scattering samples will return several beams with different optical lengths travelled, either by the scattering experienced inside the sample, or by the axial location inside the sample being different between each back-scattering point. By obtaining the OPD of each of these back-scattered beams, a depth profile of the sample, called A-scan, is created.

While based on eq. 2.7 the interference should present maximums and minimums periodically, two beams will only interfere as long as they are sufficiently coherent. A coherence length, l_c, is defined as the length along the propagation direction over which the electric field is substantially correlated. Similarly, a coherence time, t_c, is defined as the interval of time in which the correlation of a stationary point of the propagation is maintained. Therefore, t_c and l_c are related through the speed at which light is being propagated, c if assuming vacuum, such as $l_c = c * t_c$.

Extending the definition of coherence length to a polychromatic source, considering a Gaussian shape, the coherence length will be given by the full width half maximum, FWHM, of the profile defined by the eq. 2.6:

$$l_c = \frac{2\sqrt{\ln 2}}{\Delta k} = \frac{2\ln 2}{\pi}\frac{\lambda_0^2}{\Delta\lambda} \tag{2.9}$$

For a theoretical purely monochromatic source similar to a dirac delta function, the coherence length would be infinite, leading to a interference at any OPD, with periodical maximum and minimums. As the FWHM of the spectrum increases, the l_c diminishes, reducing the OPD over which the two beams interfere. This is the basis of the first type of OCT described later, Time-Domain OCT (TD-OCT).

2.1.1 Nomenclature of scanning

Describing the space in terms of x, y and z, being x the horizontal lateral axis, y the vertical lateral axis, and z the axial axis, we can define different types of data retrieval from the sample. The building block of OCT is the depth profile of a sample, or A-scan, in which the OPD of each back-scattering point along the z axis is obtained. The name was taken from ultrasound imaging or sonograms, first used medically in 1949 by George Ludwig [5], in which the information is retrieved via sound waves.

When retrieving consecutive A-scans along one of the two lateral axis, either x or y, a cross-section is obtained, typically represented with z in vertical and the lateral axis in horizontal. This cross-section is called B-scan, and at the top of the B-scan we encounter OPD = 0. By obtaining every B-scan on the other lateral coordinate we obtain a full 3D volume of the sample.

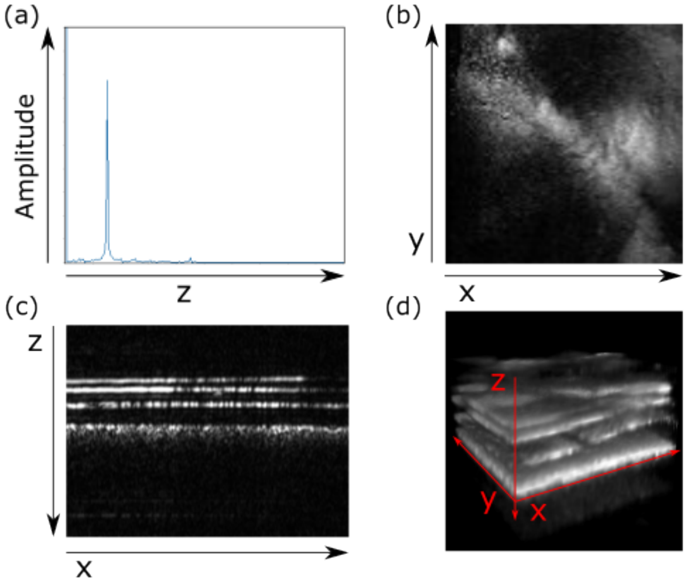

Figure 2.2: Graphical depiction of the main types of images obtained with OCT, with the size of the volume acquired being 200x200x200 voxels. (a) A-scan, (b) *en-face*, (c) B-scan, (d) 3D volume. While (a) has been obtained out of a single surface sample, (b), (c) and (d) were obtained from a ROWE retina model [6] using the OCT set-up described later on in chapter 4.

We can create a C-scan or *en-face* image by obtaining every lateral point along the x and y axis that shares the same OPD or z position. This representation usually has the y axis in the vertical dimension and the x axis in the horizontal dimension, obtaining a “surface plane”. Fig. 2.2 presents examples of each type of image obtained in OCT.

Lastly, we can perform an analysis over time by repeating any of the previously defined scans over the same positions in the sample. This is referred as “m-mode” OCT. An m-mode A-scan will be a 2D image, in which the vertical dimension corresponds to z and the horizontal dimension is time. Consequently an m-mode B-scan and m-mode *en-face* will retrieve 3D volumes, in which the first two dimensions corresponds to the traditional B-scan and *en-face* and the 3rd dimension corresponds to time. By applying m-mode to a volume, a 4D structure is retrieved.

We can distinguish between two main approaches in order to investigate larger sections of a given sample: Point scanning OCT and Full Field OCT.

Point scanning OCT

In point scanning OCT, a mechanical element is added to the basic optical design presented in Fig. 2.1, conventionally in the form of a pair of galvanometer scanners, one responsible of displacing the optical beam through the line axis to create a B-scan, and the other across the remaining lateral axis to acquire the frame, either for *en-face* or 3D volumes. The galvanometer scanners are positioned after the BS in the sample arm. As the beam returns from the sample, the displacement caused by the galvanometer scanners is countered, as long as the scanners are in a conjugated plane with the sample under examination.

Since each lateral position is illuminated at once, point scanning OCT does not suffer from cross-talk between adjacent points of the sample, but as a drawback, the imaging speed is limited by the maximum speed of the scanners. Despite this limitation, point scanning OCT has been applied in multiple biomedical applications, such as imaging tear thickness [7], deformations on the cornea for the analysis of metabolic diseases [8], and even infectious diseases at the retina level [9], but some other techniques, such as scanning multiple separated points at once [10], have been developed in order to use this strategy with faster laser sources. Miniaturisation of the scanning elements allowed for endoscopic scanning probes being used for OCT [11, 12]. In the experimental sections of this thesis, only point scanning OCT has been employed.

Full-field OCT

By applying a different variation of the Michelson Interferometer from Fig. 2.1, in which the interface optics are positioned before the BS, and therefore are shared by both arms of the interferometer, we can project a large illumination area over the sample, and project those points over a 2D camera as a detector. Therefore, full-field OCT systems reduce cost and maintenance by removing mechanical parts on the system, and bypass the speed limitation imposed by the scanners in the previous design, but in exchange, there can be cross-talk between adjacent pixels in the image under certain conditions [13, 14] and spectrometer based OCT set-ups, defined in following sections, are not suitable as they would require 3D pixel arrays as detectors.

Nonetheless, there has been extensive research on how to minimise cross talk in full-field OCT. Between some of the examples, there have been reports of the usage of deformable membranes to introduce random phase illumination [15] paired with different filtering methods [16] that effectively minimises cross talk. Recent reports using multicore fibre with small core diameters [17] seem to provide better results with simpler OCT designs.

2.2 Types of OCT

While OCT owes its origin to the Michelson interferometer, different procedures have been developed over time, each with their strengths and limitations.

2.2.1 Time Domain OCT (TD-OCT)

In order to recreate an A-scan in a TD-OCT system, the axial positions of each back-scattering point are obtained sequentially, one at a time, by matching the optical length of each arm to each other. As long as the OPD between both arms is below the coherence length, l_c, of the source used, the interference will occur in what is called "coherence gating". Hence, the capability to accurately determine the axial position of any given point, is inversely proportional to l_c.

In order to reconstruct a full A-scan, the reference arm must be modified to match the OPD for each individual back-scattering point along the z axis per lateral coordinate. There are several ways to modify the optical length of the reference arm, but they all respond to the same properties. Thus, in order to simplify the explanations, we can focus on a design as depicted in Fig. 2.3, in which the reference arm is a round-trip in which at one of the ends there is a mirror mounted on a fast moving linear translation stage.

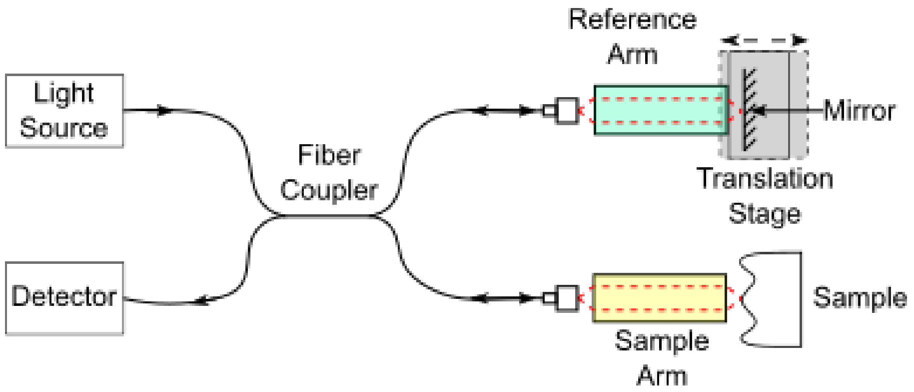

Figure 2.3: Schematic design of a simple TD-OCT system.

Given a single back-scattering point in a sample, as the reference arm length varies, the OPD shortens and lengthens, for as long as the coherence length, l_c, with a maximum in OPD= 0. This creates an envelope which FWHM determines the axial resolution, Δz_r, or the capability to discern between two consecutive back-scattering points along the z axis, of the system, as each back-scattering point will have its own associated envelope, and they will be detected as two distinct points only when their envelopes are sufficiently separated.

Assuming the envelope of interference follows a Gaussian distribution with an standard deviation of σ_l, the FWHM or axial resolution Δz_r is defined by:

$$\Delta z_r = (2\sqrt{2\ln 2})\sigma_l \tag{2.10}$$

In which σ_l is the standard deviation of the variation of OPD, given by

$$\sigma_l = \frac{c\sigma_t}{2} \tag{2.11}$$

Where c is the speed of light in vacuum and σ_t is the temporal standard deviation, defined by:

$$\sigma_t = \frac{\lambda_0^2}{2\pi c\sigma_\lambda} \tag{2.12}$$

Where λ_0 is the central wavelength of the source and σ_λ is the standard deviation of λ. If the spectrum of the source also follows a Gaussian, eq. 2.10 can be applied, having:

$$\sigma_\lambda = \frac{\Delta\lambda}{2\sqrt{2\ln 2}} \tag{2.13}$$

By applying eq. 2.11, 2.12 and 2.13 into eq. 2.10, we obtain that the axial resolution of a conventional TD-OCT is defined by:

$$\Delta z_r = \frac{2\ln 2}{\pi}\frac{\lambda_0^2}{\Delta\lambda} \tag{2.14}$$

When compared eq. 2.14 with eq. 2.9, we can see that the axial resolution is the coherence length of the source.

In terms of spatial resolution across the lateral coordinates x and y, the lateral resolution will be the minimum distance between two adjacent points such as both can be resolved as individual points. Based on this definition, there are several approaches to mathematically determine the lateral resolution. The most common approach is that followed by the Rayleigh criterion, in which the minimum resolved distance between two adjacent points will be when the centre of the Airy disc of the first point overlaps with the first minimum of the Airy disc of the second:

$$\Delta l_r = \frac{m_1}{2}\frac{\lambda_0}{NA} = 0.61\frac{\lambda_0}{NA} \tag{2.15}$$

Where m_1 is the radius constant for the first minimum of any given Airy disc, and NA is the numerical aperture of the system defined as:

$$NA = \frac{nD}{2f'} \tag{2.16}$$

Where n is the refractive index of the medium, D is the diameter of the beam, and f' is the focal length of the objective lens used.

Based on Rayleigh criterion, the two points to be distinguished will have a small region in between with a significant drop in intensity. Since the centre of the spots can be determined with a smaller drop on the intensity profile, other definitions uses a smaller constant than 0.61, such as the Abbe limit, in which 0.5 is preferred, or using the FWHM of the profile of the beam, which requires an analysis of the profile of the wavefront emitted, but in many cases yield a smaller value for the lateral resolution up to 0.41. In the following sections of this thesis, the criteria applied for the lateral resolution is that of the Rayleigh criterion, since it errs on the side of caution, and usually better approximates the situation encountered during an experiment, as some parameters can be difficult to fully control outside of a laboratory setting.

2.2.2 Fourier domain OCT (FD-OCT)

In contrast to TD-OCT systems, in which each depth in an A-scan was obtained sequentially, in Fourier Domain OCT (FD-OCT) systems, all depths are acquired simultaneously using spectral interferometry, without varying the length of the reference arm. Primarily two distinct types of FD-OCT exist based on the method to separate the spectra of the source. If the spectra is separated spatially, using a focusing element and a diffraction element, we have Spectral Domain OCT (SD-OCT), also called Spectrometer Based OCT in some sources. If the spectra is separated temporally, by sweeping the spectrum in the source using different types of filtering, and then obtain the interference element sequentially, using a photodetector, we talk about Swept Source OCT (SS-OCT).

Spectral Domain OCT (SD-OCT)

A typical SD-OCT system employs a low coherent source that is split into two different arms, as in TD-OCT, but differs in the usage of a spectrometer as a detector. A spectrometer is made up of a focusing lens, a diffraction element, such as a diffraction grating, and a photodiode array, conventionally a 1D line camera. A conventional design of such system is shown in Fig. 2.4.

After recombining the two beams, the diffraction element, from now on a diffraction grating, separates the recombined beam into its spectral components. The spectral components of the reference beam interferes with the spectral components of the sample arm, creating an interference pattern that is projected onto the 1D line camera. As the interference is now generated at the spectral components, the linewidth of each spectral component, determined by the density of lines of the

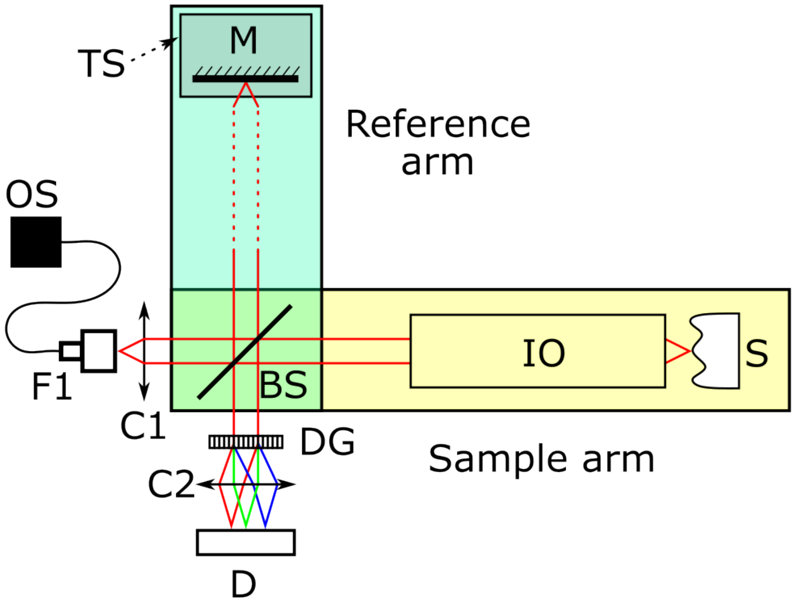

Figure 2.4: Schematic design of a spectrometer based SD-OCT system. The reference arm, marked in light blue, reflects on a mirror mounted on a translation stage (TS). The TS is used to fine adjustments on the OPD between both arms, remaining stationary during operation. BS: Beamsplitter; C1,C2: Collimators; DG: Diffraction grating; D: Detector; F1: Fibre mount; IO: Interface optics; M: Mirror; OS: Optical source; S: Sample; TS: Translation stage

diffraction grating, determines the sensitivity of the SD-OCT, which is expected to be improved over the TD-OCT counterpart [18].

The interference signal acquired by the camera follows eq. 2.5, so in order to reconstruct the A-scan, a Fourier transform is required, obtaining:

$$\begin{aligned} i_D(z) =& \frac{\rho}{8}\left[\gamma(z)\left[R_r + R_{s_1} + R_{s_2}...\right]\right] \\ &+ \frac{\rho}{4}\left[\gamma(z) \circledast \sum_{n=1}^{N} \sqrt{R_r R_{s_n}}\left(\delta\left[z \pm 2(z_r - z_{s_n})\right]\right)\right] \\ &+ \frac{\rho}{8}\left[\gamma(z) \circledast \sum_{n\neq m=1}^{N} \sqrt{R_{s_n} R_{s_m}}\left(\delta\left[z \pm 2(z_{s_n} - z_{s_m})\right]\right)\right] \end{aligned} \tag{2.17}$$

In order to recover the reflectivity profile, previously mentioned in eq. 2.1, the cross-correlation term of eq. 2.17 can be benefited from the sifting property of the delta function, so that:

$$\begin{aligned} i_D(z) =& \frac{\rho}{8}\left[\gamma(z)\left[R_r + R_{s_1} + R_{s_2}...\right]\right] \quad \text{"(A)"} \\ &+ \frac{\rho}{4}\sum_{n=1}^{N}\sqrt{R_r R_{s_n}}\left[\gamma\left[2(z_r - z_{s_n})\right] + \gamma\left[-2(z_r - z_{s_n})\right]\right] \quad \text{"(B)"} \\ &+ \frac{\rho}{8}\sum_{n\neq m=1}^{N}\sqrt{R_{s_n} R_{s_m}}\left[\gamma\left[2(z_{s_n} - z_{s_m})\right] + \gamma\left[-2(z_{s_n} - z_{s_m})\right]\right] \quad \text{"(C)"} \end{aligned} \tag{2.18}$$

A few key differences can be found in (B) against eq. 2.1. While some of these differences, such as the axial position of each scattering point in the sample being now measured against the position of the reflector in the reference arm, or the relative distances inside the sample being doubled, due to the double-pass configuration, are to be expected from the previous analysis in TD-OCT, there are extra details to account for. For instance, the reflectivity from the sample, $R_s(z_s)$, is amplified by the reflectivity from the reference arm, R_r, but the biggest one is the apparent broadening of each reflector due to the convolution with the gamma function, $\gamma(z)$. This effect is in itself the definition of the point spread function, PSF, of an imaging system. It is related to the coherence length of the source, meaning that the axial resolution is still linked to the FWHM of the full spectrum, following eq. 2.14.

On top of these differences, as any inverse Fourier transform of a real number produces positive and negative frequencies that are complex conjugates of each other, a duplicity or mirror terms appear in the cross-correlation terms. These mirror terms will appear at an exact opposite from the OPD = 0, so in order to avoid them as artefacts, the OPD = 0 must be placed outside of the sample.

Swept Source OCT (SS-OCT)

All the previous theory described for SD-OCT still applies in SS-OCT, as once the interferometric signal has been retrieved by the detector, both interferometric signals share the same properties and can be processed into an A-scan in the same manner. Therefore, all the differences we will discuss here are in the source choices and the setup designs.

Different approaches to build Swept Sources can be found in the literature. From SS-OCT systems employing micro-electromechanical systems (MEMS) paired in vertical cavity surface-emitting lasers (VECSEL) [19, 20], in which the MEMS vibrates at high speeds inside the cavity, changing the tuning wavelength, to Acousto-Optical tunable filter (AOTF) based systems [21, 22], in which a birefringent crystal's properties are modulated with an acoustic wave, filtering the incident optical spectrum, to pairing a polygon mirror with a diffraction grating inside the cavity of the source [23].

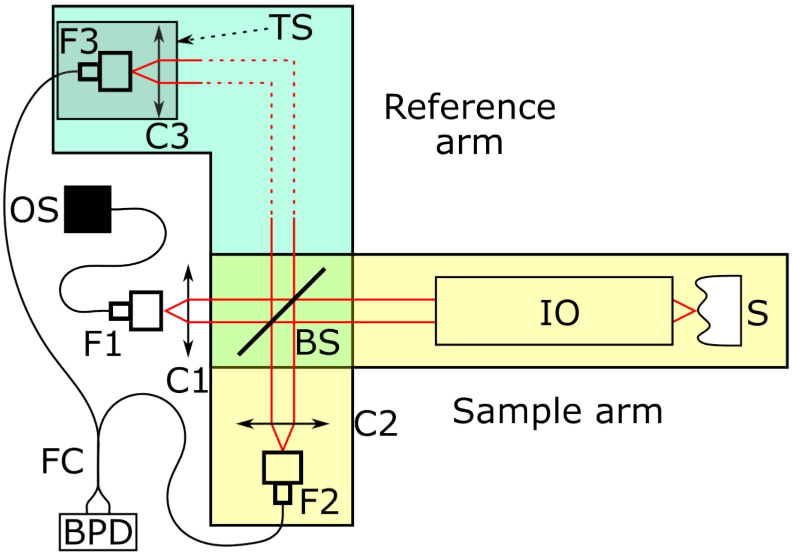

Figure 2.5: Schematic diagram of a conventional SS-OCT setup. Both the fibre end and its corresponding collimator lens on the receiving end of the reference arm is mounted on a translation stage (TS) for fine adjustments of the OPD, but remains stationary during operation. BPD: Balanced photodetector; BS: Beamsplitter; C1-3: Collimators; F1-3: Fibre mounts; FC: 50/50 Fibre coupler; IO: Interface optics; OS: Optical source; S: Sample; TS: Translation stage

In Fig. 2.5 a typical SS-OCT setup is presented. In comparison with Fig. 2.4, a photodetector, in this case a balanced photodetector (BPD), is used to detect the interferometric signal instead of a spectrometer. The 1D-line cameras used in SD-

OCT read out all the spectrum at once, which results in a signal roll-off. The usage of a photodetector allows to avoid this shortcoming, improving depth and range of imaging.

The Fourier transform required for the reconstruction of the A-scan in FD-OCT implies a maximum imaging depth and a sensitivity falloff related to the spectral resolution of the setup. In addition to the spectral resolution, as the spectral interferogram is digitally analysed, sampling of the interferogram is required, following Nyquist criterion.

The instantaneous linewidth and the sweeping speed of the sources designed for SS-OCT determines the spectral resolution and the A-scan rate respectively. These parameters vary greatly between each design, with narrower and uniform linewidths improving the spectral resolution and faster sweeps improving the A-scan rate. In SD-OCT the spectral resolution is determined by the design of the spectrometer, improving when using denser gratings, longer distances between grating and camera, and higher pixel-density camera arrays, while the A-scan rate is linked to the acquisition speed of the camera readout.

Both FD-OCT systems experience non-linearity effects due to the spectral dispersion required by design, in SD-OCT due to the non-linear distribution of the light by the grating, and the SS-OCT non-linearities linked to slightly different linewidths across the spectrum sweep. These non-linearities translate into a loss of axial resolution. In order to correct this artefact, a relinearisation step is added on the A-scan retrieval algorithm that can be speed up by the addition of k-clocks on the source, secondary interferometers that interrogate the spectrum shape in real time.

2.2.3 Master-Slave OCT (MS-OCT)

First introduced in 2013 as Master-Slave Interferometry (MSI) [24], and later on 2016 improved to Complex Master-Slave Interferometry (CMSI) [25], Master-Slave

OCT (MS-OCT) operates in the same regime as the FD-OCT set-ups described above, but instead of reconstructing the A-scan using an FFT, MS-OCT relies on a direct product of the interference spectra with a previously recorded set of spectra, called masks.

Each masks is, simply put, an interference spectra corresponding to a particular OPD that carries all the non-linearities and dispersion encountered in the specific optical set-up being used. MS-OCT is executed in two stages, a first stage of calibration, called Master, in which the sample arm is also fitted with a mirror, similar to the one of the reference arm. In these conditions, spectra is recorded at different OPDs which will be used as masks. After storing this spectra we move to the second stage of operation, or Slave, in which the mirror in the sample arm is replaced back with the sample to investigate. The interference spectra obtained is then correlated with the masks obtained in the previous Master stage, generating the A-Scan. Originally, each OPD to be evaluated in an A-scan required a mask obtained experimentally, recorded as a set of masks, which required large amounts of time, so for real-time applications, another interferometer could be set up out of the same optical source with a specific OPD, generating that specific mask in real-time, with no recording needed, and retrieving each depth from the A-scan by modifying the OPD in the Master interferometer.

The correlation based algorithm described in [26] consists on comparing the spectra recorded as masks with the spectra obtained from the sample. The whole set of masks is multiplied with the spectra at from the sample, now referred as slave spectra, and the closer the resemblance between the slave spectra and a mask, the higher the intensity returned for that particular OPD. This allows MS-OCT to operate in more regimes than a regular FD-OCT, as an *en-face* can be retrieved without requiring a full volume acquisition of the sample by simply multiplying the interrogated spectra with a single mask, which determines the depth to which the *en-face* corresponds. Fig. 2.6, obtained from the original article "Master-Slave interferometry for parallel spectral domain interferometry sensing and versatile 3D optical coherence tomography" authored by Adrian GH. Podoleanu and Adrian Bradu [24], presents a simplified view of the operation of MS-OCT.

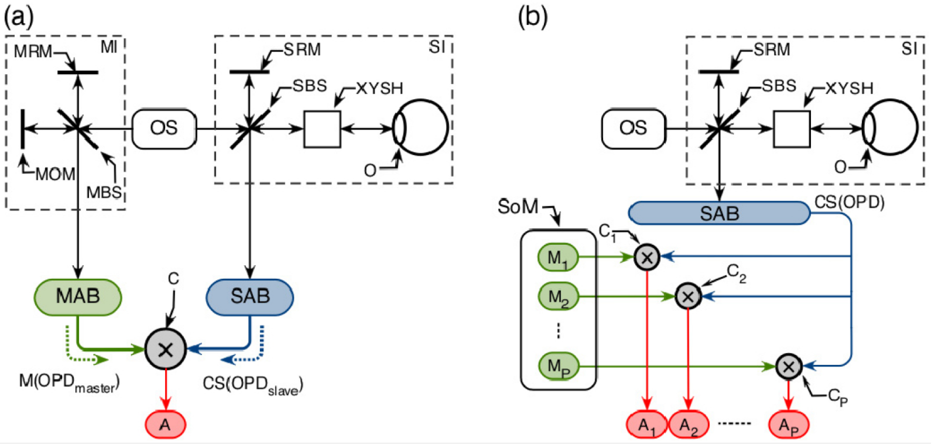

Fig. 1

Citation
Adrian Gh. Podoleanu, Adrian Bradu, "Master–slave interferometry for parallel spectral domain interferometry sensing and versatile 3D optical coherence tomography," Opt. Express **21,** 19324-19338 (2013);
https://opg.optica.org/oe/abstract.cfm?URI=oe-21-16-19324

Figure 2.6: "Illustration of the MSI principle. (a) Implementation of the MSI method using two interferometers, a master interferometer (MI) and a slave interferometer (SI). OS: optical source; MBS: master beam-splitter; SBS: slave beam-splitter; MRM: master reference mirror; SRM: slave reference mirror; O: object under investigation; MOM: master object mirror; XYSH: two-dimensional lateral scanning head; MAB: master acquisition block; SAB: slave acquisition block; C: comparison block. (b) Parallel implementation of the MSI principle, where the MI in (a) is replaced with SoM: storage bank of P memories, M1, M2, . . . MP, a memory for each point in depth in the object, O. C1, C2, . . . CP: P comparison blocks; A1, A2,. . . AP: amplitudes of sampled points of the A-scan from scattering points inside the object O from respective depths z1, z2, . . . zP." quoted from - Podoleanu et. al. [24]

By this point, MS-OCT had already a set of advantages over other FFT based systems, such as higher tolerance to dispersion, no need to resample data, and even tailor the depth resolution by using sets of masks, but the Master stage required still too much time, causing issues for any changes or readjustments in the set-up could render the system unusable for hours, until a full new set of masks was reacquired. CMSI solved the issue of the slow mask generation by reconstructing the storage of masks out of a few pre-recorded channelled spectra. The method, described extensively in [25] is based on the generation of two functions, a first function g that responds to the non-linearities experienced by the decoder element of the OCT, i.e. the spectrometer itself in SD-OCT or the non-linear sweep of the swept source in SS-OCT, and a second function h that represents the unbalanced dispersion present in the interferometer. These two functions are embedded into each experimental channelled spectra, therefore, they can be extracted out of a selected number of OPDs and used to reconstruct the masks for the rest of OPDs not evaluated in the Master stage.

To obtain g and h functions, we follow the steps described in [25], by starting obtaining the complex exponential form of the channelled spectra at a particular z. The phase obtained from this spectra can be expressed as:

$$\phi^{\exp}(\tilde{v}, z) = \frac{2\pi}{c} g(\tilde{v}) 2z + h(\tilde{v}) + \phi_{rand}(z) \tag{2.19}$$

where $\tilde{v}$ is the non-uniform distribution along the axis of the detector. Then we proceed to remove the random phase by performing a derivative in respect of $\tilde{v}$:

$$\frac{\delta}{\delta\tilde{v}} \phi^{\exp}(\tilde{v}, z) = \frac{2\pi}{c} g'(\tilde{v}) 2z + h'(\tilde{v}) \tag{2.20}$$

where $g'(\tilde{v})$ and $h'(\tilde{v})$ are the derivatives of g and h respectively. By applying a linear regression over a few experimental channelled spectra, we obtain the slope of the function g' and the y-intercept of h' and we rebuild them along the spectral coordinate $h'(\tilde{v})$. Finally, following an indefinite integration, g and h can be used to reconstruct a phase to build a matrix M of masks at any given z. With this new procedure, the time taken by the master stage in CMSI is reduced to just a few minutes. On top of that, some adjustments in h can be performed without requiring new acquisitions, allowing for some improvements even in post-processing.

In summary, the procedure to obtain a depth profile in MS-OCT can be explained as follows: First, a flat mirror is placed in focus on the position of the sample in the sample arm. Second, the OPD is matched with the reference arm and the interference spectra is collected via a digitiser. Third, the length in the reference arm is displaced a known quantity and a new spectra is collected. Fourth, for CMSI, we repeat the previous step 3 to 4 times, and then collect the non-interferometric signal of the reference and sample arm separately, blocking one arm at a time, while for MSI we would repeat step 3 as many times as depths to evaluate in our A-scan. Fifth, if using CMSI, we generate g and h out of the spectra collected and then generate as many masks as depths wanted to evaluate in our A-scan, then we save this stack. Sixth, now with our stack of masks, either in CMSI or MSI, we remove the mirror in the sample arm and place the object to study. Finally, the channelled spectra returned from the object is now compared to the masks using a correlation-based algorithm, returning the intensity for each OPD returning from the different layers inside the sample, which constitutes the A-scan.

This methodology has been applied via LabVIEW code on the experimental chapters of this thesis. While most of the reports on MS-OCT currently implement complex master-slave OCT algorithm, some research is being done following similar designs as the two parallel interferometers presented in the original paper for downconversion [27, 28].

2.3 Sensitivity and Signal-to-Noise Ratio (SNR)

As the name itself implies, Signal-to-Noise Ratio (SNR) is the ratio between the signal power and the background noise. It is commonly used as an indicator of the sensitivity of an OCT device, and it has slight differences based on the OCT type employed.

Starting with TD-OCT systems, the total detected photocurrent responds to:

$$I_D(z_r) = \frac{\rho S_{TDOCT}}{2}\left[R_r + R_s + 2\sqrt{R_r R_s}\exp -(z_r - z_s)^2 \Delta k^2 \cos\left[2k_0(z_r - z_s)\right]\right] \tag{2.21}$$

Where $S_{TDOCT} = S_0/2$ is the instantaneous source power incident in both arms. The maximum intensity is given when $z_r = z_s$, given by $\langle I_D \rangle^2_{TDOCT} = \frac{\rho^2 S^2_{TDOCT}}{2}\left[R_r R_s\right]$, so the noise present in TD-OCT is mainly shot noise, which is given by $\sigma^2_{sh} = 2e\bar{I}B$, where e is the electronic charge, $\bar{I}$ the mean detector photocurrent and B the electronic detection bandwidth. As in a traditional TD-OCT system, the reference arm is translated across z axis, a doppler shift given by $f_D = 2v_{ref}/\lambda_0 = k_0\_max/\left(\pi\Delta t\right)$. Hence, the optimal detection bandwidth is around twice the FWHM of f_D, given by $B_{TDOCT} \approx 2\Delta k_{FWHM} z_{max}/\left(\pi \Delta t\right)$. As any backscattered signal from the sample arm will be much smaller than the reference arm power, the main source of noise comes from the reference arm itself as $\sigma^2_{TDOCT} = \rho e S_{TDOCT} R_r B_{TDOCT}$, which gives us the final formula of:

$$SNR_{TDOCT} = \frac{\langle I_D \rangle^2_{TDOCT}}{\sigma^2_{TDOCT}} = \frac{\rho S_{TDOCT} R_s}{2eB_{TDOCT}} \tag{2.22}$$

Which means that the SNR will be linked to the bandwidth of the detector used in the set-up. Meanwhile, FD-OCT has been presented with an advantage in sensitivity over the TD-OCT counterpart [29]. Starting with a simplified equation for a single reflector and no autocorrelation, in order to compare with the eq. 2.21 from TD-OCT, we obtain:

$$I_D[K_m] = \frac{\rho}{2} S_{FDOCT}[k_m] \left[R_r + R_s + 2\sqrt{R_r R_s} \cos\left[2k_m(z_r - z_s)\right] \right] \tag{2.23}$$

where $S_{FDOCT}[k_m] = (S(k)|_{k=k_m})/2$ corresponds to the portion of the instantaneous power of the central spectral channel m. After an inverse Fourier transform operation, with a single reflector, maximum intensity will appear when $z_r = z_s$, following assuming a Gaussian distribution of the spectral power:

$$\begin{aligned} i_D[z_m = (z_r - z_s) = 0] &= \frac{\rho}{2}\sqrt{R_r R_s} \sum_{m=1}^{M} S_{FDOCT}[k_{M/2}] \\ &= \frac{\rho}{2}\sqrt{R_r R_s} S_{FDOCT}[k_{M/2}] \cdot M \cdot 0.598 \end{aligned} \tag{2.24}$$

Based on eq. 2.24, we infer that the spectral interference pattern from each detection channel adds coherently, leading to a mean-square peak signal power of $\langle i_D \rangle^2_{FDOCT} = \frac{\rho^2 S^2_{FDOCT}[k_m]}{4} [R_r R_s] \cdot M^2$. Noise, on the other hand, will be dependant on the spectral channel, i.e. the noise in each spectral channel is uncorrelated, and will add incoherently in the inverse discrete Fourier summation, giving:

$$\sigma^2_{FDOCT}[z_m] = \sum_{m=1}^{M} \sigma^2_{FDOCT}[k_m] = e\rho S_{FDOCT}[k_m] R_r B_{FDOCT} \cdot M \tag{2.25}$$

Thus, the equation for the SNR in FD-OCT systems is described by:

$$SNR_{FDOCT} = \frac{\langle i_D \rangle^2_{FDOCT}}{\sigma^2_{FDOCT}} = \frac{\rho S_{FDOCT}[k_m] R_s}{4eB_{FDOCT}} \cdot M \tag{2.26}$$

where a square distribution of power has been assumed, to simplify the equation, as any other shape would alter a coefficient added to M. In order to compare the three systems, TD-OCT, SD-OCT and SS-OCT, a few considerations must be taken into account: For SS-OCT, where each spectral channel is acquired sequentially, assuming a scanning range $\Delta k = 2k_{FWHM}$ and that an anti-aliasing filter is in place for B_{SSOCT}, then $B_{SSOCT} = B_{TDOCT}$. For SD-OCT, where all the spectral channels are acquired simultaneously, $S_{SDOCT}[k_m] = S_{TDOCT}/M$ and $B_{SDOCT} = B_{TDOCT}/M$ since there is an integration of all the signals over the full A-scan.

$$SNR_{SDOCT} = SNR_{SSOCT} = \frac{\rho S_{FDOCT}[k_m] R_s}{4eB_{FDOCT}} \cdot M = SNR_{TDOCT} \cdot \frac{M}{2} \tag{2.27}$$

The improvement of a factor of M is attributed to the sampling of all depths at once constantly. Nonetheless, it is important to note that several of the assumptions taken on the calculations, such as the power distribution or the shot noise condition at all wavelengths, are unrealistic. Despite this, FD-OCT systems are theoretically capable of up to 20 dB greater sensitivity [4].

References

1. *Optical Coherence Tomography: Technology and Applications* en (eds Drexler, W., Fujimoto, J. G. & Greenbaum, E.) ISBN: 978-3-540-77550-8. `http://link.springer.com/10.1007/978-3-319-06419-2` (Springer, 2015).
2. Wang, L. V. *Biomedical optics: principles and imaging* ISBN: 978-0-470-17700-6 (Wiley-Blackwell, Sept. 2012).
3. Shankland, R. S. Michelson and his interferometer. *Physics Today* **27,** 37–43. ISSN: 0031-9228. eprint: `https://pubs.aip.org/physicstoday/article-pdf/27/4/37/10950262/37\_1\_online.pdf`. `https://doi.org/10.1063/1.3128534` (Apr. 1974).
4. Izatt, J. A., Choma, M. A. & Dhalla, A.-H. in *Optical Coherence Tomography: Technology and Applications* (eds Drexler, W. & Fujimoto, J. G.) 65–94 (Springer International Publishing, Cham, 2015). ISBN: 978-3-319-06419-2. `https://doi.org/10.1007/978-3-319-06419-2_3`.
5. Campbell, S. A short history of sonography in obstetrics and gynaecology. *Facts, views & vision in ObGyn* **5,** 213 (2013).
6. Rowe, T. S. *Phantom for rendering biological tissue regions* US Pat. 8,480,230. 2013. `https://patents.justia.com/patent/8480230`.
7. Werkmeister, R. M. *et al.* Measurement of Tear Film Thickness Using Ultrahigh-Resolution Optical Coherence Tomography. *Investigative Ophthalmology & Visual Science* **54,** 5578–5583. ISSN: 1552-5783. eprint: `https://arvojournals.`

org/arvo/content_public/journal/iovs/932987/i1552-5783-54-8-5578.pdf. https://doi.org/10.1167/iovs.13-11920 (Aug. 2013).

8. Temstet, C. *et al.* Corneal epithelial thickness mapping using Fourier-domain optical coherence tomography for detection of form fruste keratoconus. *Journal of Cataract & Refractive Surgery* **41,** 812–820. ISSN: 0886-3350. https://www.sciencedirect.com/science/article/pii/S0886335015002199 (2015).
9. Kurup, S. P., Khan, S. & Gill, M. K. Spectral domain optical coherence tomography in the evaluation and management of infectious retinitis. *Retina* **34,** 2233–2241 (2014).
10. Wieser, W., Biedermann, B. R., Klein, T., Eigenwillig, C. M. & Huber, R. Multi-Megahertz OCT: High quality 3D imaging at 20 million A-scans and 4.5 GVoxels per second. *Opt. Express* **18,** 14685–14704. https://opg.optica.org/oe/abstract.cfm?URI=oe-18-14-14685 (July 2010).
11. Xu, Y. *et al.* Design and development of a 3D scanning MEMS OCT probe using a novel SiOB package assembly. *Journal of Micromechanics and Microengineering* **18,** 125005 (2008).
12. Huo, L., Xi, J., Wu, Y. & Li, X. Forward-viewing resonant fiber-optic scanning endoscope of appropriate scanning speed for 3D OCT imaging. *Opt. Express* **18,** 14375–14384. https://opg.optica.org/oe/abstract.cfm?URI=oe-18-14-14375 (July 2010).
13. Bonin, T., Franke, G., Hagen-Eggert, M., Koch, P. & Hüttmann, G. In vivo Fourier-domain full-field OCT of the human retina with 1.5 million A-lines/s. *Opt. Lett.* **35,** 3432–3434. https://opg.optica.org/ol/abstract.cfm?URI=ol-35-20-3432 (Oct. 2010).

14. Wang, J., Bradu, A., Dobre, G. & Podoleanu, A. Full-Field Swept Source Master-Slave Optical Coherence Tomography. *IEEE Photonics Journal* **7,** 1–14 (2015).

15. Stremplewski, P. *et al.* In vivo volumetric imaging by crosstalk-free full-field OCT. *Optica* **6,** 608–617. `https://opg.optica.org/optica/abstract.cfm?URI=optica-6-5-608` (May 2019).

16. Li, J. *et al.* Cross-free in both lateral and axial directions for Fourier-domain full-field optical coherence tomography. *Journal of Physics D: Applied Physics* **55,** 195401 (2022).

17. Auksorius, E. *et al.* Multimode fiber as a tool to reduce cross talk in Fourier-domain full-field optical coherence tomography. *Opt. Lett.* **47,** 838–841. `https://opg.optica.org/ol/abstract.cfm?URI=ol-47-4-838` (Feb. 2022).

18. Leitgeb, R., Hitzenberger, C. K. & Fercher, A. F. Performance of fourier domain vs. time domain optical coherence tomography. *Opt. Express* **11,** 889–894. `https://opg.optica.org/oe/abstract.cfm?URI=oe-11-8-889` (Apr. 2003).

19. Zhang, J. *et al.* Multi-MHz MEMS-VCSEL swept-source optical coherence tomography for endoscopic structural and angiographic imaging with miniaturized brushless motor probes. *Biomed. Opt. Express* **12,** 2384–2403. `https://opg.optica.org/boe/abstract.cfm?URI=boe-12-4-2384` (Apr. 2021).

20. Grijalva, E. A. P. *et al.* *Novel 1.6 MHz swept source for real-time volumetric in-vivo OCT imaging of the human retina* in *Optical Coherence Tomography and Coherence Domain Optical Methods in Biomedicine XXVII* (eds Izatt, J. A. & Fujimoto, J. G.) **12367** (SPIE, 2023), 1236704. `https://doi.org/10.1117/12.2649142`.

21. Rinehart, M., Zhu, Y. & Wax, A. Quantitative phase spectroscopy. *Biomed. Opt. Express* **3,** 958–965. `https://opg.optica.org/boe/abstract.cfm?URI=boe-3-5-958` (May 2012).

22. Machikhin, A. S. *et al. Acousto-optical tunable filter for a swept light source with variable transmission function* in *Optical Design and Testing VIII* (eds Wang, Y., Kidger, T. E. & Tatsuno, K.) **10815** (SPIE, 2018), 108150L. `https://doi.org/10.1117/12.2502756`.

23. Everson, M., Duma, V.-F. & Dobre, G. *Optimisation of a polygon mirror-based spectral filter for swept source optical coherence tomography (SS-OCT)* in *2nd Canterbury Conference on OCT with Emphasis on Broadband Optical Sources* (eds Podoleanu, A. & Bang, O.) **10591** (SPIE, 2018), 105910V. `https://doi.org/10.1117/12.2283034`.

24. Podoleanu, A. G. & Bradu, A. Master–slave interferometry for parallel spectral domain interferometry sensing and versatile 3D optical coherence tomography. *Opt. Express* **21,** 19324–19338. `https://opg.optica.org/oe/abstract.cfm?URI=oe-21-16-19324` (Aug. 2013).

25. Rivet, S. *et al.* Complex master slave interferometry. *Opt. Express* **24,** 2885–2904. `https://opg.optica.org/oe/abstract.cfm?URI=oe-24-3-2885` (Feb. 2016).

26. Bradu, A. & Podoleanu, A. G. Imaging the eye fundus with real-time en-face spectral domain optical coherence tomography. *Biomed. Opt. Express* **5,** 1233–1249. `https://opg.optica.org/boe/abstract.cfm?URI=boe-5-4-1233` (Apr. 2014).

27. Podoleanu, A., Cernat, R. & Bradu, A. Down-conversion en-face optical coherence tomography. *Biomed. Opt. Express* **10,** 772–788. `https://opg.optica.org/boe/abstract.cfm?URI=boe-10-2-772` (Feb. 2019).

28. Martinez Jimenez, A. *et al.* Downconversion master slave OCT with a bidirectional sweeping laser. *Journal of Biophotonics* **17** (July 2024).

29. Bail, M. A. *et al. Optical coherence tomography by spectral radar for the analysis of human skin* in *Optical and Imaging Techniques for Biomonitoring III* **3196** (1998), 38–49.

Chapter 3

Handheld OCT Probe

Author's note: Most of the work presented in this chapter resulted in a peer reviewed article called "Endoscopic *en-face* optical coherence tomography and fluorescence imaging using correlation-based probe tracking" [1]. The chapter has been partially rewritten, in order to highlight the work done by this author, bringing some of the contributions in the supplementary material to the forefront. The main contributions of the author were on the assembly, ROI detection, validation, and results, with the least work done in the stitching algorithm, as the author only worked on the axial compensation part of the algorithm.

3.1 Introduction

Endoscopic optical coherence tomography (E-OCT) allows high-resolution imaging of tissue to a depth of 1-2 mm beneath the surface. E-OCT was first demonstrated [2] in the 1990s, a few years after the very first report of OCT on the eye [3]. Since then, E-OCT has been commercialized for use in coronary arteries, complementing intravascular ultrasound for interventional guidance [4]. Other potential applications of E-OCT include imaging the epithelium of internal organs, particularly for early diagnosis of cancerous lesions or for lateral margin identification during endoscopic surgery [4].

E-OCT probes can be broadly divided into 'side-viewing' and 'forward-viewing' designs. Figure 3.1 presents common schematic designs for both type of scanning probes. Side-viewing probes involve deflecting the beam exiting a fibre by 90 degrees, using a prism or mirror or by angle-cleaving the fibre. Scanning can be achieved by rotating the fibre using a motor at the proximal end, outside of the patient [2, 5, 6]. Alternatively, the deflecting element may be fixed onto a micro-motor at the distal end of the probe, in which case the fibre and lens assembly itself does not need to rotate [7–9]. To improve tolerance to probe bending, it is possible to implement the side-viewing probe as a common-path interferometer [10]. Different optical configurations in the distal end, such as those involving the use of a diffractive lens [6], can also help to mitigate spectral losses when large spectral bandwidths are required for increased axial resolution. 3D imaging is achieved by moving the probe axially, obtaining 'tunnel-like' images. The side-viewing probe can be incorporated into a capsule for oesophageal imaging without an endoscope [11]. Side-viewing probes can also have very small diameters; needle probes with diameters as small as a few hundred microns having been demonstrated [12]. Using distal motors, they can also achieve high scan rates (up to 4000 frames/s), particularly when coupled with optical sources allowing MHz A-line rates, such as Fourier-domain Mode-Locked Lasers [9]. A comprehensive review of side-viewing probes is provided in Ref. [4].

Side-viewing probes are ideal for imaging tubular-shaped structures such as vasculature or parts of the gastrointestinal tract. They are less well-suited to general endoscopic use where it may be desirable to have a forward-looking image, such as at branches of the airways, in organs such as the bladder or the stomach, or for image-guided surgery. For this reason, forward-viewing probes have also been developed, although not successfully commercialized. There are two common approaches to miniaturization of forward-viewing scanning probes. The first, and most common, is to scan the fibre itself laterally, usually behind a lens [13]. It is also possible

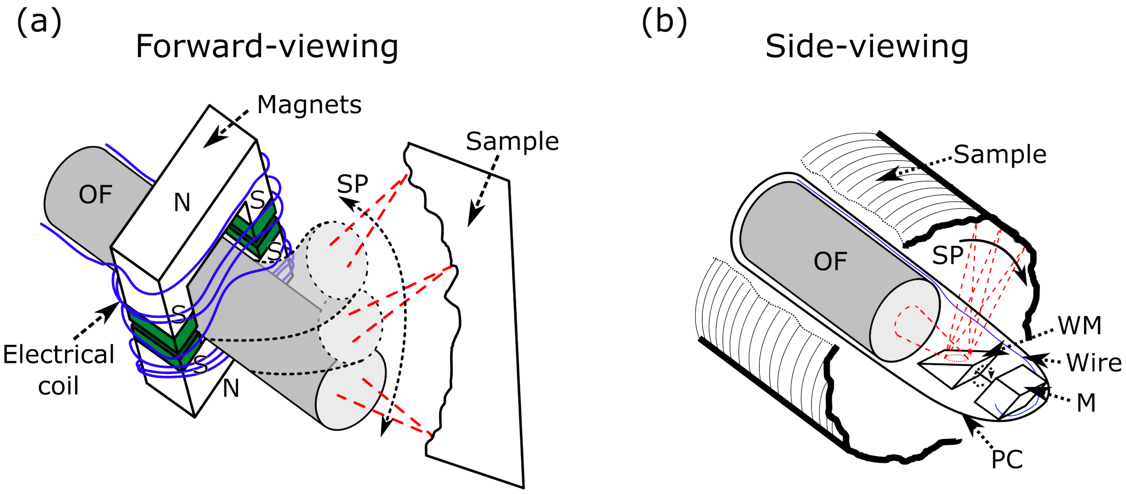

Figure 3.1: Schematic designs of the usual working principle for 1-D scanning endoscopic probes, with the optical fibre coloured in gray, any wires in blue and the light source in red. (a) Forward-viewing probe. Scanning is based on a voice coil, with the optical fibre set through a pair of magnets surrounded by electrical coil. N: North pole of the magnet; S: South pole of the magnet, also coloured in green; SP: Scanning path of the B-scan; OF: Optical fibre. (b) Side-viewing probe. The scanning mechanism is based on a distal wedged mirror connected to a small motor, with the optical fibre, the mirror and the motor all encased in a transparent material that forms the probe. The motor rotates the wedge mirror that deviates the light towards the sides of the probe and into the sample, which in this case is represented in a tubular way around the probe. The motor is connected through a wire to the proximal end of the probe, with the cable casting a shadow in the B-scans. PC: Plastic cover, used as the external element encasing the probe; WM: Wedged mirror.

to integrate a miniature fibre-based lens into the fibre itself [14]. The second is to incorporate a miniature beam-scanning element using a micro-electromechanical (MEMS) mirror surface [15], although the need to fold the beam makes this less suitable for narrow-diameter probes. In either case, the scanning can either be in one direction only, producing 2D cross-sectional OCT images, or in two directions, allowing 2D *en-face* images and volumes to be assembled.

The design of forward-viewing OCT endoscopic probes is challenging in several respects. The probe would normally be introduced to the body via the working channel of an endoscope, limiting both the maximum possible probe diameter (to around 3 mm) and the length of the rigid tip. It is technically difficult to build a fast 2D scanning element at low cost and in a sufficiently small package. The field-of-view tends to be small since, unlike side-viewing probes which can rotate a full 360°, forward-viewing probes only scan over a small arc. For example, while recent state-of-the-art forward-scanning compact probe heads can acquire several volumes per second, typical image sizes are 0.8-3.5 mm [13, 14, 16–20]. To maintain an acceptable depth-of-field for endoscopic use, lateral resolution is typically 10-30 µm, resulting in a relatively small number of lateral resolution elements in the image.

In this chapter a recently published concept [1] is introduced, in which an endoscopic probe designed for lung exploration was fitted with a 1D distal scanning mechanism (the fast scan), and the raster scanning (or scanning along the orthogonal axis) was completed by a manual bending mechanism located at the distal end of a flexible endoscope. This relaxes the requirements on the distal scanning mechanism (reducing it to a single axis scan), and means that OCT volumes can be much larger along the manual-scan (slow-scan) direction than those that could be produced by any feasible miniaturized distal scanning mechanism within the probe itself. This new approach comes with its own challenges, particularly the difficulty of assembling volumes during manual scanning without artefacts due to irregular motion along the manual-scan direction and unwanted axial motion of the probe (discussed in more detail below). Contrary to other devices [21] in which the slow-scan is produced by a robotic actuator, the volumes acquired with the system described here will present variable speed and direction in the slow-scan, as well as axial position displacements. In order to ensure an artefact-free image, the instantaneous speed of the probe must be determined and any motion, lateral or axial, must be accounted for.

In this chapter I will briefly introduce the full method reported, in which the motion in the direction out-of-plane of the B-scans was corrected by applying a speckle correlation-based algorithm, and focus on the axial motion analysis and validation, as this was, alongside the characterisation of the system, my main contributions to the article in which this chapter is based upon. The probe was designed with the idea of analysing not just the structural condition of lung tissue, but also assess other biological processes associated with a normal metabolic function of the tissue. Healthy lung tissue exhibits autofluorescence, while damaged tissue will start stopping the autofluorescence signal before we can observe any structural damage, therefore, the idea from the other researchers involved in the project was to use a dual-clad fibre for a forward viewing probe, allowing the collection of the autofluorescence signal of the specific B-scan explored. Due to different constraints in the development of the project, we were unable to tested on an *in-vivo* scenario, so we used a staining agent on chicken breast to simulate and characterise the fluorescence sensitivity of the OCT setup.

3.1.1 State of the art in volume assembly

The problem of assembling volumes from 2D B-scans has previously been studied in the context of manually-scanned 2D ultrasound probes, and algorithms based on speckle correlation have been suggested [22]. Conversely, most reports on the assembly of OCT images with some elements of manual scanning focus on building

B-scans from A-scans. This is in contrast to the situation faced here, where we have one axis of mechanical scanning, producing high-quality B-scans, and we wish to assemble volumes and *en-face* images via manual scanning in the second, slow-scan, direction. Nevertheless, there are some clear similarities between the two tasks.

For assembly of B-scans from A-scans, in 2009 Ahmad *et al.* [23] demonstrated a simple algorithm in which the Pearson cross-correlation coefficient is calculated between a reference A-scan and each subsequent A-scan. Once the correlation drops below an experimentally determined threshold, the current A-scan is added to the B-scan and the process is repeated (with the current A-scan becoming the new reference). To reduce the impact of structural features, the A-scan had a moving average filter of several resolution elements in size applied, and this filtered A-scan was subtracted from the unfiltered A-scan. Liu *et al.* extended this work in 2012 [24] by incorporating a theoretical model of speckle to determine the probe displacement corresponding to a specific correlation value without experimental calibration. In 2015, Wang *et al.* [25] showed that improved performance could be achieved by taking multiple correlations between pairs of A-scans with different time separations.

While these A-scan assembly techniques were developed mainly for manually-scanned OCT probes, similar techniques have been applied to proximally-driven side-viewing endoscopes in order to correct non-uniform rotational distortions (NURDs). Of particular relevance to this work, Uribe-Patarroyo *et al.* [26] noted difficulties with patient motion, occasional under-sampling and areas of tissue with low signal which inevitably mean that image-based tracking cannot provide a perfect correction. Aboeui *et al.* [27] adopted a more complex algorithm involving dynamic time warping. Other approaches to correct NURDs in side-viewing endoscopes include tracking reflections from the endoscopic sheath [28] or fiducial markers [29]; these methods are not applicable to a forward-viewing probe or the work reported in this manuscript.

The task faced here of assembling volumes from B-scans, where the slow-scan direction is manually scanned, is also related to the task of assembling volumes in side-viewing endoscopic OCT, where a manual pull-back of the probe acts as the second axis of scanning. Variations in the speed of the pull-back cause distortions in the resulting volume. Lee *et al.* [30] proposed an approach in which two B-scans are acquired at two axial positions of the probe. As the probe moves axially, at some point the rear B-scan images the same point on the tissue as the front B-scan, and the time difference between these two events allows for the axial speed of the probe to be determined. A similar method was applied to a forward looking galvanometer-based [31] bench-top system but would be difficult to implement in a compact forward-viewing probe. More recently, Nguyen *et al.* [32] proposed a method to correct both for NURDs and longitudinal speed variations in side-viewing OCT. The longitudinal correction involved analysing the statistical variation of intensity in the *en-face* image within a sliding window to estimate the pull-back speed.

As discussed below, the method we adopted is closely related to the cross-correlation technique previously used to assemble B-scans from A-scans with manual scanning [23], but with the difference that mechanically-scanned B-scans are assembled into volumes (and fluorescence T-scans are assembled into fluorescence images). The lower frame rate of B-scans compared with the line rate of A-scans necessitates some modifications to the approach to allow for difficulty in ensuring over-sampling during manual scanning along the slow axis. As demonstrated below, this allows volumes to be successfully built when the probe is manually scanned using an endoscope at speeds of up to 4 mm/s.

3.2 Materials and methods

A schematic diagram of the OCT/fluorescence endoscopic system used in this study is presented in Fig. 3.2. The system, loosely based on a configuration reported by Scolaro *et al* [33], combines a swept-source OCT sub-system operating at a central wavelength $\lambda_0 = 1310\,\text{nm}$ with a fluorescence imaging sub-system, with a $\lambda_e = 488\,\text{nm}$ solid-state laser providing the excitation. The two sub-systems share the same endoscopic probe (detailed in the next section), combined by means of a double-clad fibre coupler (DCFC, Thorlabs, model DC1300LEFA).

Briefly, in the OCT sub-system, the output from a MEMS swept-source (Axsun Technologies, central wavelength $\lambda_0 = 1310\,\text{nm}$, tuning range $\Delta\lambda = 100\,\text{nm}$, sweep rate 100 kHz) is sent to a fused fibre coupler DC1, with a splitting ratio of 90/10. 10% of the optical power is routed to a custom-built optical delay line (ODL) forming the reference arm of the interferometer, and is afterwards reunited with the power returning from the object arm at DC2, which has a 50/50 split ratio to ensure balanced detection at the photo-detector BPD (Thorlabs, model PDB480C-AC).

In the object arm of the OCT interferometer, the optical signal from the swept source is routed to a fibre-based wavelength division multiplexer (WDM, Font Canada, custom 488/1310 nm fibre optic combiner) via a circulator, CIRC (AFW Technologies, model CIR-3-13-B-1-2-VR01), where it is combined with the output power from a 488 nm solid-state laser providing the fluorescence excitation (JDSU, FCD488FC-020, 488 nm wavelength, $\approx 20\,\text{mW}$ CW output power). Both optical signals are directed to the double-clad fibre coupler, DCFC (Thorlabs, model DC1300LEFA), where the combined OCT/fluorescence excitation power is routed to the double-clad fibre output, connected to the OCT/fluorescence probe, which is described in greater detail in Section 3.2.1.

The first cladding mode of the double-clad fibre collects any fluorescence signal

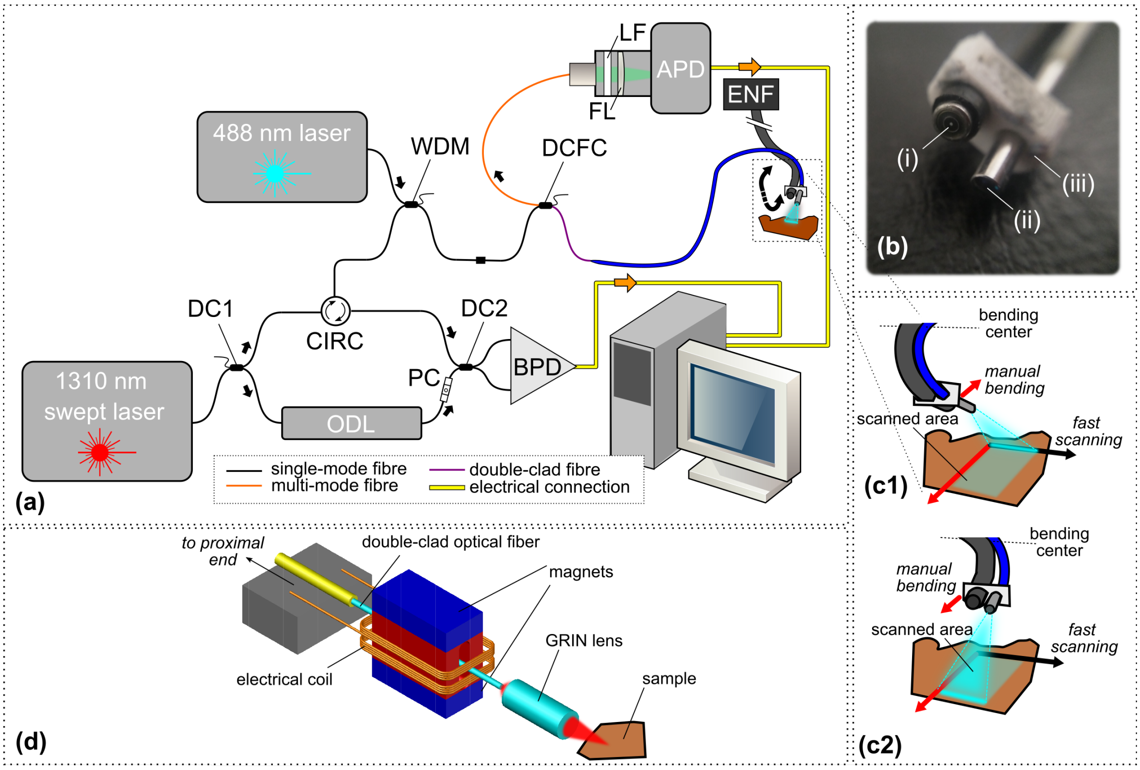

Figure 3.2: (a) Schematic diagram of the endoscopic SS-OCT/fluorescence system used in this study. DC1-2: fused fibre directional coupler; CIRC: optical fibre circulator; WDM: wavelength division multiplexer/combiner; DCFC: double-clad fibre directional coupler; LF: emission filter; FL: achromatic lens; APD: avalanche photodetector; ODL: optical delay line; BPD: balanced photo-detector; ENF: Olympus ENF endoscope proximal controls. (b) Photograph of the Olympus ENF-P4 endoscope distal end (i), showing the OCT/fluorescence probe (ii) mounted to it using a 3-D printed bracket (iii). (c1)-(c2) Detail from (a), showing a close-up of the combined probe end with the Olympus endoscope at two manual scan positions. (d) schematic diagram showing the voice coil operated 1-D scanning probe.

from the sample, whereas the back-scattered OCT signal is routed through the core (fundamental) mode. In this way, the DCFC is capable of separating the returned OCT signal from the fluorescence signal. The latter is sent to an avalanche photodiode amplifier module (APD, Hamamatsu model C5460-01, frequency response from DC to 100 kHz) via an emission filter LF (Thorlabs, model FBH520-40) and an achromat $f = 200\,\mathrm{mm}$ lens FL (to ensure an optimum spot size on the active area of the APD), whereas the former is sent to the OCT interferometer via the WDM and CIRC. To provide fluorescence signal, the tissue in Section 4 was stained for approximately 2 minutes with acriflavine hydrochloride before rinsing with water.

Following detection of both OCT and fluorescence signals, their electrical representations are digitized into the computer (using, respectively, an AlazarTech model 9350 sampling at 500 MS/s and a National Instruments model PCIe-6321, sampling at 200 kS/s).

3.2.1 OCT/fluorescence probe

The endoscopic probe is a forward-viewing, 1-D scanning probe, with an outer diameter of approximately 3 mm and a working distance of approximately 1 mm. Its working principle has been described elsewhere [21, 34, 35]; briefly, the probe operates on the voice coil principle, employing a cantilevered optical fibre which oscillates when driven by an alternating electric current (schematically shown in Fig. 3.2 (d)). The fibre tip is imaged onto the sample by means of a gradient-index (GRIN) lens (Edmund Optics, #64-545, 0.46 mm working distance), creating a linear scan of up to 2 mm in length, depending on the amplitude of the drive signal. Whereas the similar probe employed in our previous work [21] used a single-mode, SMF-28e fibre, in this case, due to the need to detect the fluorescence signal, we instead used a 1250-1600 nm double-clad fibre (DCF13, Thorlabs, Newton, NJ, USA, core diameter 9 µm, first cladding diameter 105 µm, second cladding diameter 125 µm).

3.2.2 OCT image reconstruction

In order to reconstruct OCT B-scans, the raw channelled spectra are processed using the Complex Master-Slave (CMS) method [36]. CMS replaces the Fourier transform usually employed in conventional OCT signal processing, presenting advantages such as tolerance to dispersion in the interferometer [37], long depth imaging due to the requirement for a swept-source k-clock being dropped [38], and improved reconstruction speed when only a small number of depth points are needed [39]. This last point is of potential relevance to this work, as the image reconstruction could be made to operate over a subset of the axial range, allowing *en-face* images to be assembled in real-time even for very high B-scan rates. However, this selective depth reconstruction was not necessary for the frame rates reported here. Further processing was also required to correct the distortion in the lateral direction due to the sinusoidal probe scanning drive signal. This was corrected by linear interpolation, assuming a sinusoidal scan, and was performed in real-time.

3.2.3 Endoscope integration

While the OCT probe is small enough to fit through a standard endoscope working channel, a suitable endoscope was not available when conducting this study. Instead, the OCT probe was fixed externally to an Olympus MODEL ENF-P4 endoscope, using a 3-D printed bracket as shown in Fig. 3.2(b)(iii). The Olympus endoscope has an outer diameter of 3.6 mm and a bending range of up to 130 degrees, which allows the OCT/fluorescence probe to be scanned in the out-of-plane direction with respect to the B-scans. A similar approach of external fixing was previously employed for combined endoscopic and OCT imaging of the larynx [35]. In practice the OCT/fluorescence probe would normally be inserted through the working channel of a compatible endoscope, but otherwise the procedure would be similar.

When fixing the probe to the endoscope it was necessary to ensure that the direction of endoscope bending was approximately perpendicular to the OCT probe scanning direction. This was achieved by viewing the laser scanning line on an infrared viewing card, rotating the OCT probe until the line was correctly oriented, and then fixing the probe in place.

3.2.4 Algorithm for assembly of volumes and en-face images

Axial positioning

The method to determine the out-of-plane speed requires that a region of interest (ROI) is extracted from within a scattering region of the sample. In practice this means placing the ROI just under the top surface. I compared five different approaches for determining the location of the top surface of the sample in the B-scan:

- **Method 1.** Convolution of each A-scan in the B-scan with a step function (5 pixels of -1, 5 pixels of 1). The position of the peak intensity of the result for each A-scan is then taken as the position of the surface for that A-scan.
- **Method 2.** As Method 1, but using correlation instead of convolution.
- **Method 3.** As Method 2, but using normalized cross correlation.
- **Method 4.** Binarisation of the B-scan (using a threshold of twice the mean pixel value for the image) followed by morphological open and close operations with disc-shaped structuring element of 30 × 30 pixels (285 × 300 µm). The first non-zero pixel in each A-scan is then taken to be the surface position for that A-scan.
- **Method 5.** Applying a Sobel filter and then taking the position of the peak intensity in the result for each A-scan as the location of the surface position for that A-scan.

For each approach, three different pre-processing steps were also tested: an auto intensity adjustment (Matlab imadjust, using 1% saturation high and low), a Wiener filter, and a 3x3 moving average filter.

All methods were compared against manual segmentation of a test set of B-scans extracted from 10 data volumes, with three B-scans analysed per volume. The first three volumes were taken from *in-vivo* human skin imaging, while the other seven were taken from *ex-vivo* ox tripe. The RMS difference between the manual and automatic surface position was then averaged across all the datasets. The results, grouped by method and image pre-correction, are shown in Fig. 3.3(a).

The Sobel filter with pre-processing using the Wiener filter (Fig. 3.3(a)(ii)) resulted in the lowest average RMS error across the datasets (0.13 mm). However, while this was slightly better than the binarisation and morphological operations method (0.29 mm), the binarisation method is computationally much simpler. Small errors with respect to the manual segmentation are not of great importance as the ROI will still cover approximately the desired area of tissue. The binarisation and morphological method (Fig. 3.3(a)(i)) was therefore used throughout this study.

Fig. 3.3(b) compares the results of these two methods on the images on which they performed best and worst: an example of *in-vivo* human skin, on the left, and *ex-vivo* tripe, on the right. In both cases, the median top surface position (and hence the location used for the top of the ROI) is the same to within a few pixels (i.e. a few 10s of µm). While some methods seem to present large RMS, the images used had more than 5 mm depth. The step function in methods 1 to 3 has to be optimised for the sample under investigation, which in this case could not be done as the surface could change abruptly. Therefore, these methods had break points in many B-scans, which drove the RMS up as it could be identified as a maximum of 5 mm jump. Method 4 seemed unaffected by the irregularity of the surface, which made the approach more efficient on this sample.

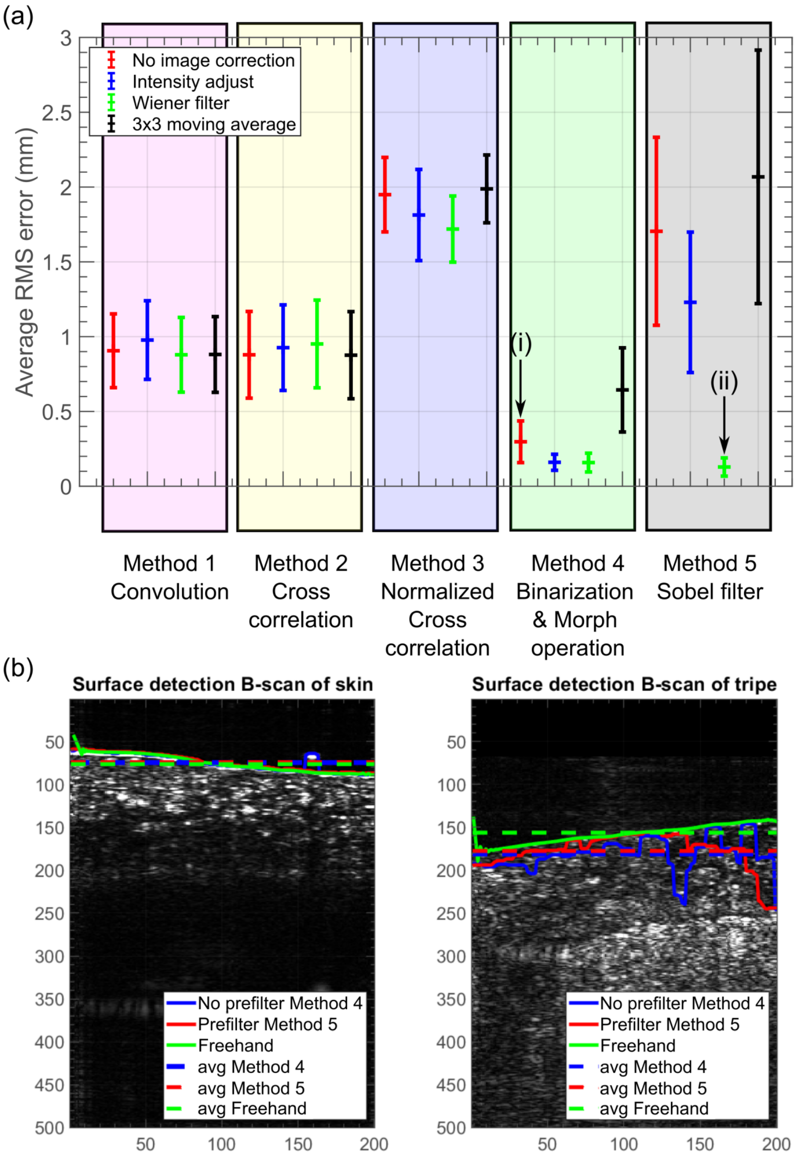

Figure 3.3: (a) Average RMS error with respect to manual segmentation for each combination of surface detection approach and image pre-correction. The error bars are the standard deviation of the RMS values across 30 different test images. Arrows indicate: (i) Method 4 with no pre-correction, which was employed in the chapter, and (ii) Method 5 with a Wiener pre-filtering, which provides slightly better results at the expense of more complex processing. The RMS in some methods, while large, is to be expected, as breaks in the surface detection can drive the errors up. (b) Examples of B-scans of human skin (left) and ox tripe (right). The dashed lines indicate the median position of the surface across the sample while the continuous lines show the position detected at each A-scan. The freehand registration is shown in green, the Sobel method in red, and the binarisation in blue. The units are image pixels, in the vertical scale 1 pixel is 10 µm, in the horizontal scale 1 pixel is 9.5 µm, leading to images of 1.9 mm by 5 mm.

As an example, the processing steps for locating the approximate axial position of the tissue surface in a B-scan using the selected method are shown for *ex vivo* imaging of porcine lung tissue in Fig. 3.4. The raw image shown in Fig. 3.4(a) is thresholded and binarised, as shown in Fig. 3.4(b), and morphological open and close operations are performed, as shown in Fig. 3.4(c). The location of the first non-zero pixel in each column is shown overlaid on the B-scan in Fig. 3.4(d). The median value of these surface heights, which is used to position the region of interest (ROI) for correlation measurements, is shown in Fig. 3.4(e).

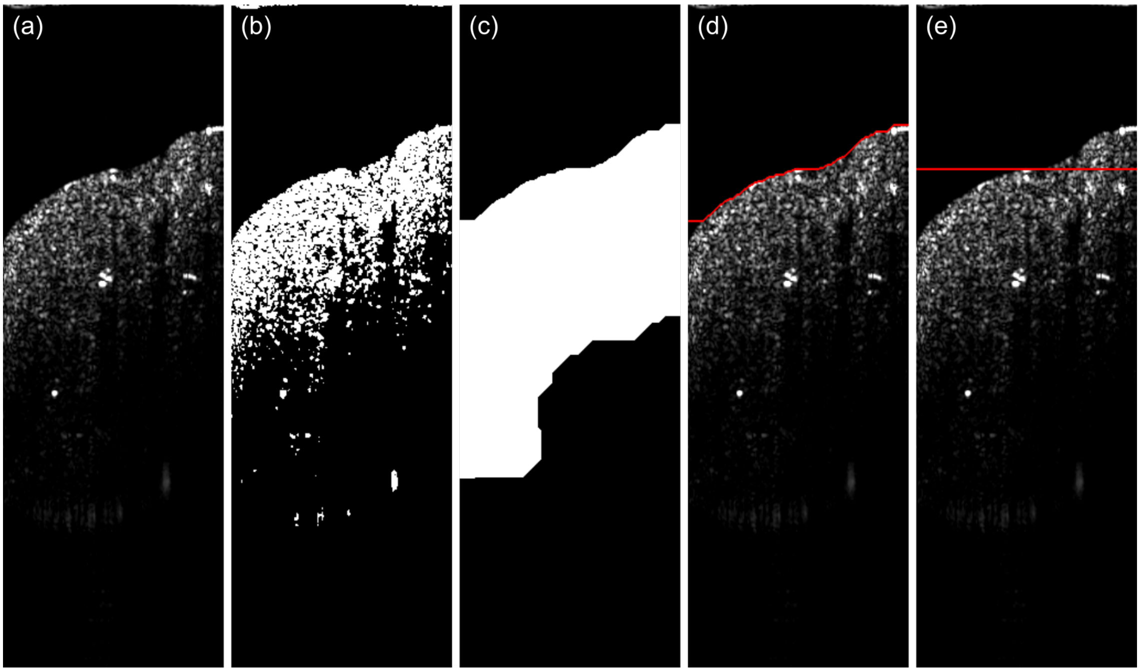

Figure 3.4: Example of surface finding in a B-scan of porcine lung tissue. (a) B-scan. (b) Thresholded and binarised B-scan. (c) Morphological close and open. (d) Estimated surface overlaid on B-scan (e) Median surface overlaid on B-scan.

The step-by-step process for the assembly of volumes is summarise as following and represented graphically in Fig. 3.5: First, a ROI (Fig. 3.5(b)) is extracted from the B-scan (Fig. 3.5(a)) using the methods explained above. Secondly, the mean filtered version of this ROI, Fig. 3.5(c), is subtracted from the original ROI to obtain an image with increased speckle contrast, Fig. 3.5(d). This is then Gaussian filtered to reduce noise, as shown in Fig. 3.5(e). Thresholding, followed by a morphological open operation, produces a mask which is shown in Fig. 3.5(f) and overlaid as red pixels on the ROI in Fig. 3.5(g).

Only pixels which are not masked, i.e. those which are black in Fig. 3.5(f), are used in the correlation calculation, to avoid saturated pixels affecting the results. The cross-correlation is taken between the masked image and a masked reference image to determine the in-plane shifts. After correction for the in-plane shifts, the correlation is calculated between the reference image and the current image (with the mask still used to remove bright pixels). If the correlation is below the threshold, the B-scan is added to the volume and the current image becomes the reference image.

3.2.5 Real-time implementation

To demonstrate the feasibility of assembling *en-face* images in real-time during endoscopic investigations, a simplified form of the algorithm was implemented in LabVIEW (National Instruments). While the majority of the algorithm was implemented using standard LabVIEW functions (including the Vision Development Module), cross-correlation and image filtering prior to speckle correlation measurement was performed using the OpenCV4 library, accessed from LabVIEW via DLLs compiled from C++. The implementation functioned similarly to the method described above, including tissue flattening in the slow-scan direction and interpolation. Probe tilt correction (i.e. flattening in the fast-scanning lateral direction) was not performed, as this requires information from the entire volume scan and hence cannot be implemented in a real-time *en-face* preview. OCT B-scans can be streamed directly to the *en-face* assembly algorithm from the OCT acquisition and processing software or from a saved datafile. Images were successfully processed in real-time at B-scan frame rates of 250 Hz, and the *en-face* image extracted at a fixed depth relative to the estimated tissue surface was displayed with line-by-line

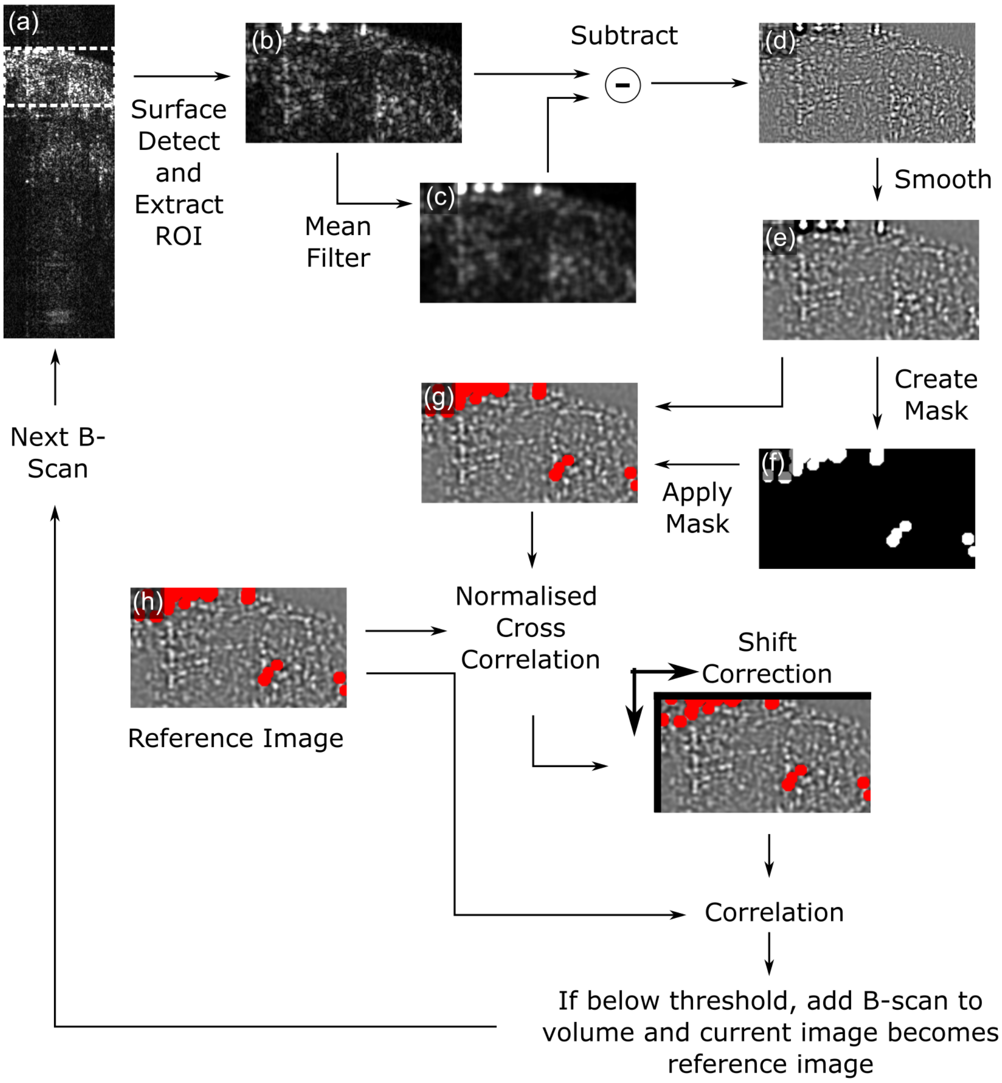

Figure 3.5: Illustration of processing steps in shift calculation. (a) Complete B-scan of chicken breast tissue showing region of interest (ROI) as dashed box. (b) Extracted ROI. (c) Mean-filtered ROI. (d) Result of subtracting mean-filtered ROI from original ROI. (e) Result of a applying a 2D Gaussian filter to (d). (f) Mask calculated by thresholding and morphological open operation on (b). (g) Mask overlaid on the filtered ROI. (h) Reference image.

update as the probe was scanned. A video of the real-time display is provided in Supplementary Video 1 of the associated publication [1] and the LabVIEW code is provided on Figshare [40].

3.3 Quantitative characterisation and validation

3.3.1 Optical coherence tomography probe and system

The procedure to quantify the sensitivity of the OCT channel was the same as in a previous study from Marques *et al.* [21]. An A-scan was obtained from a brushed metal target and the signal to noise ratio (SNR) of the A-scan peak was measured with respect to the average noise floor to be 39.8 dB. The reference arm was then blocked and the optical power was measured at the BPD first from the brushed metal and then from a mirror. The ratio of these measured powers was 35.5 dB, and this was used to correct the measured signal-to-noise ratio of the signal from the metal to obtain a sensitivity of 75.3 dB. This is much lower than $85 - 92$ dB in our other MS systems previously reported in the literature. This may be due to lower efficiency in re-injecting light back into the DCF inside the custom-made probe. The width of the A-scan peak was measured to be 28 µm, which effectively dictates the axial resolution of the system.

To measure the signal level of the fluorescence channel as function of distance from the probe, the probe was mechanically translated at constant speed away from a piece of paper stained with a 0.05 g/100 mL solution of acriflavine hydrochloride. The average signal across the fluorescence T-scan is plotted as a function of distance from the probe tip (determined from the position of the OCT-scan surface peak) in Fig. 3.6(a). Peak signal was obtained at 1.5 ± 0.1 mm from the probe, and there is no significant selection in depth for the fluorescence channel.

To characterize the lateral resolution of the probe, a positive United States Air

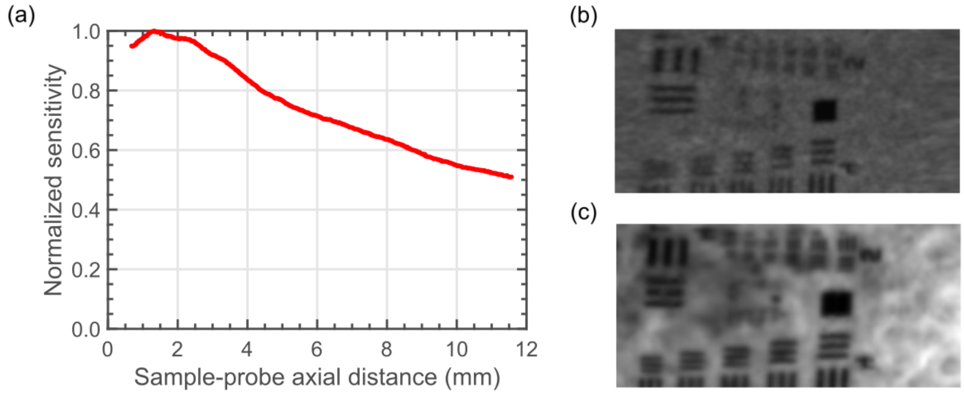

Figure 3.6: (a) Fluorescence signal as a function of distance from probe tip. A moving average filter of 5 points was applied to smooth the fluorescence sensitivity profile. (b) *En-face* OCT image of a positive USAF target. (c) Fluorescence image of positive USAF target placed over fluorescently-stained paper.

Force (USAF) resolution target was placed on top of the stained paper. The probe was mechanically translated at constant speed across the sample at an optical distance of 2.5 mm, without resorting to the B-scan-based reconstruction method. To this goal, a translation stage (Newport, model LTA-HS) was used. An *en-face* slice from the OCT channel and a fluorescence image are shown in Fig. 3.6(b) and (c), respectively. In the OCT channel, element 4 of group 4 can be resolved in both scanning directions, giving a lateral resolution of 22.1 µm. In the fluorescence channel, element 1 of group 5 can be resolved, giving a lateral resolution of 15.63 µm.

3.3.2 Characterisation of volume/en-face assembly

To determine the relationship between speckle correlation and out-of-plane motion, the probe was translated over a scattering phantom (paper resolution target) and chicken breast tissue at 0.5 mm/s using the same motorized translation stage as in the previous section, perpendicular to the fast-scan direction (i.e in a direction that is out-of-plane of the OCT B-scan). The normalized cross correlation between the first image and a region of interest of 180×100 pixels (1710×1000 µm) extracted from each subsequent image was then calculated to determine in-plane shifts. The shift-corrected images were then processed as described above in Section 3.2.4, and the correlation as a function of out-of-plane motion distance was then calculated. This was performed 50 times, each with a different starting point within the scan, leading to a mean coefficient of variation of 14% across all data points, The correlation for zero shift was calculated by averaging the correlation between 20 pairs of images when the probe was not in motion to account for the effect of random noise.

The mean correlation is shown as a function of out-of-plane distance for the chicken breast tissue in Fig. 3.7(a). The correlation drops to 0.5 at a distance of 10.4 µm. The curve is approximately linear between correlations of 0.7 and 0.3. For the paper target, the correlation drops to 0.5 at a distance of 10.8 µm, suggesting that this calibration is not highly dependent on the sample properties, and so this data is not shown.

A Gaussian fit to the data of the form

$$f(x) = (f_{max} - f_{min}) \exp(-x^2/2\sigma^2) + f_{min} \tag{3.1}$$

is also shown. σ, f_{max} and f_{min} are free parameters, found to be 12.0 µm, 0.952 and 0.052 for paper and 12.5 µm, 0.891 and 0.114 for the tissue, respectively. f_{max} is the correlation between images when there is no out-of-plane motion, f_{min} is the residual correlation at large distances, and σ is an estimate of the speckle grain size and hence the lateral resolution. Using the conventional definition of resolution as the full-width half-maximum (FWHM) of the point-spread function, this corresponds to an expected lateral resolution of approximately 21 µm in the out-of-plane direction, compared to the experimentally determined value of 22 µm in the in-plane direction.

This curve can be used to determine an appropriate value for the correlation threshold, c_t. Clearly the value must lie in the range between f_{min} and 1 or it will never be reached. As the threshold approaches f_{min} the separation between B-scans

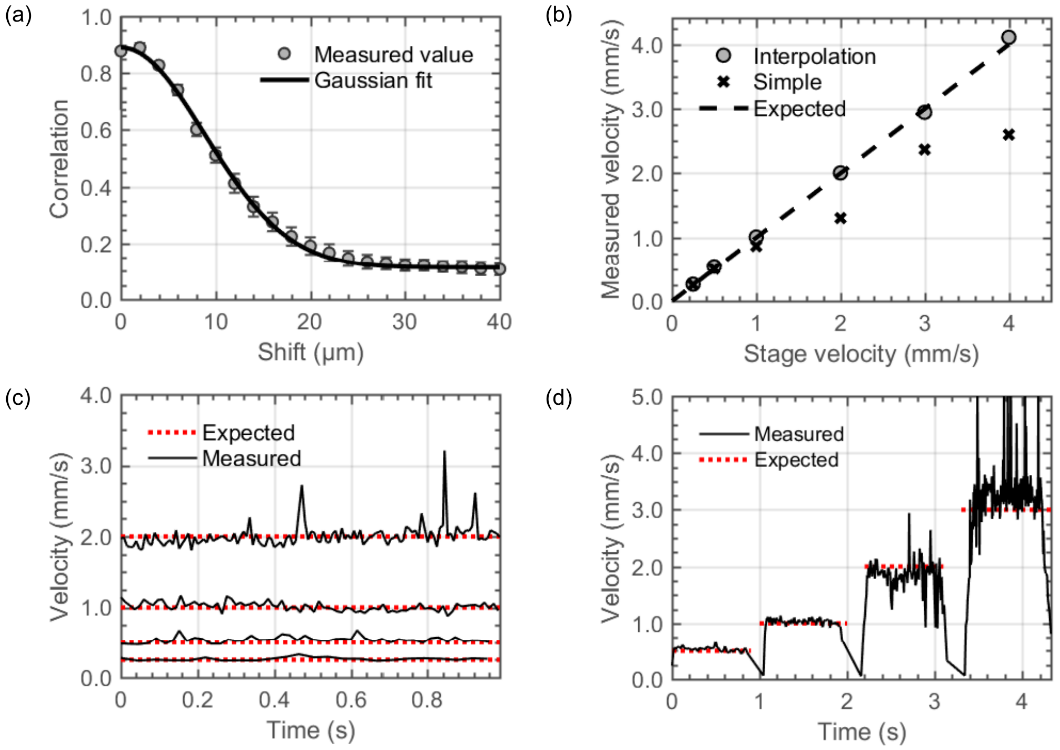

Figure 3.7: Validation of speed estimation in the out-of-plane direction via speckle decorrelation, using a mechanical translation stage to move the OCT probe over chicken breast tissue. (a) Correlation as a function of out-of-plane movement distance, average of 50 starting points. Error bars are standard deviation across 50 runs. A least-squares Gaussian fit is shown. (b) Measured speed using simple and interpolation based methods for six different velocities. (c) Speed measured as a function of time using interpolation method for four different translation stage speeds. (d) Speed measured as a function of time using interpolation method for probe motion with varying speed. Drops to zero speed are a mechanical feature of the way in which the stage was programmed, and are not artifacts of the method.

will become reasonably large compared to the lateral resolution, while a threshold close to 1 will be more subject to random noise or other variations unrelated to out-of-plane motion. To follow the convention of sampling approximately twice per resolution element, a threshold of $c_t = 0.5$ was adopted for the following work. The out-of-plane movement required to reach this decorrelation threshold is then $z_{dec} = 10.4\,\mu\text{m}$.

The speed of the probe in the out-of-plane direction can be estimated by determining how many B-scan frames are required for the correlation to drop below the threshold (n). The measured average speed, $\bar{v}$, is then given by

$$\bar{v} = \frac{R z_{dec}}{n} \tag{3.2}$$

where R is the B-scan frame rate. The number of frames, n, can be calculated using either the simple method, taking the first frame where the correlation falls below the threshold, or the interpolation method, in which a non-integer number of frames is calculated. For both methods, Fig. 3.7(b) shows the average estimated speed when the stage was set to move at several constant speeds. The simple method underestimates larger speeds quite significantly as expected. The maximum possible speed which can be predicted by the simple method is that corresponding to when a single frame ($n = 1$) is sufficient to drop below the threshold, which is approximately 2.6 mm/s with the parameters used here. In comparison, the interpolation method continues to accurately estimate speeds as high as 4 mm/s, even though the probe is under-sampling by a factor of 1.5 at this speed.

The instantaneous speed estimated as a function of time is shown in Fig. 3.7(c) for four velocities. The standard deviation is approximately 10% of the mean for all velocities in the range 0.25 to 4 mm/s, but there are an increased number of spurious high and low speed points for the larger speeds. Figure 3.7(d) shows the results of setting the motorized stage to change speed during the acquisition. Due to the way the stage was programmed, the speed briefly dropped to zero between each segment, as can be seen in the estimated speed. The processing step of masking bright pixels prior to measuring the correlation between images was found to be critical when specular reflections occurred from the tissue surface, otherwise the probe speed would be significantly under-estimated at these points.

The OCT probe was then moved freehand over a printed grid phantom with fluorescent highlighter applied. An example of the raw *en-face* OCT and fluorescence images are shown in Fig. 3.8(a,b). Severe distortion is present due to lateral motion and inconsistent out-of-plane motion, as expected. Figure 3.8(a) also shows the effect of axial motion of the probe; this is less apparent in Fig. 3.8(b) due to the lack of optical sectioning in the fluorescence channel (see Section 3.3.1). Figure 3.8(c) shows the reconstructed *en-face* image correcting only for out-of-plane and lateral motion, while Fig. 3.8(d) shows the result if surface-flattening is also employed. Finally, Fig. 3.8(e) shows the reconstructed fluorescence image. While some artifacts can be observed in the reconstructed *en-face* views, the algorithm successfully recovers the broad morphology of the sample.

3.4 Imaging Results Under Simulated Conditions

An example of an OCT volume and fluorescence images of porcine lung tissue (stained with acriflavine hydrochloride, as described in Section 3.2), manually acquired using the endoscope for the slow-scan (as described in Section 3.2.3), is shown in Figure 3.9. Figure 3.9(a-d) show raw acquisitions, while Fig. 3.9(e-g) show reconstructed images after processing. Figure 3.9(c,g) show B-scans along the fast-scan direction, while Fig. 3.9(a,e) show B-scans extracted from the volume along the slow-scan direction. Figure 3.9(b,f) show *en-face* images extracted from the vol-

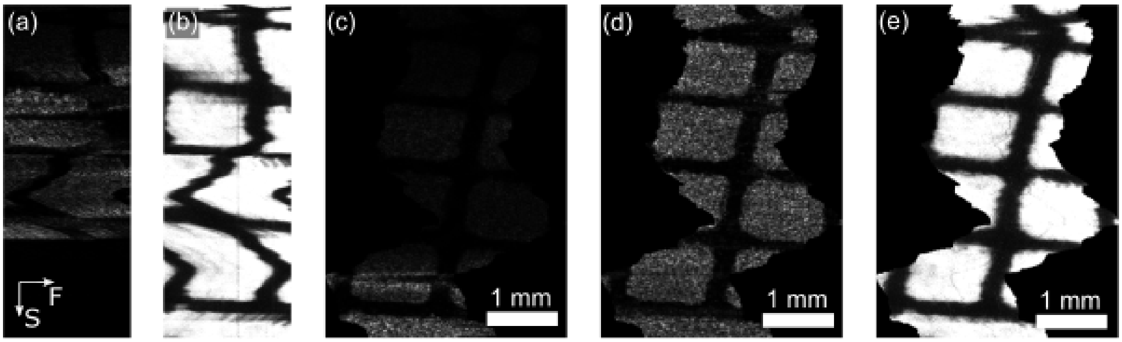

Figure 3.8: Reconstruction of OCT and fluorescence images following freehand probe scan over fluorescently-stained printed grid phantom. (a) *En-face* slice extracted from raw volume. (b) Raw fluorescence image. (c) *En-face* slice from motion-corrected volume without surface correction. (d) *En-face* slice from motion-corrected volume with surface correction. (e) Motion-corrected fluorescence image. (a)-(b) have the same horizontal scale as (c)-(e) but have no vertical scale since this depends on the instantaneous probe speed. The arrows in (a) show the direction of the fast lateral (F) and slow manual endoscope (S) scans.

ume. There was considerable in-plane lateral motion during this scan, and so the *en-face* and fluorescence images have been rotated by 37 degrees for convenient display. The effect of the algorithm in removing the motion artifacts near the top of the images can clearly be seen. The surface flattening effect can also be clearly observed by comparing the slow-axis B-scans and by observing the more constant intensity along the *en-face* image in Fig. 3.9(f).

Figure 3.9(i) shows the relative probe position as a function of time calculated by the algorithm, while Fig. 3.9(j) shows the calculated speed in the slow-scan (out-of-plane) direction. For most of the scan the measured probe speed in the out-of-plane direction was approximately 1 mm/s, although there are a large number of spikes up to around 2 mm/s which could be a result of jerky motion leading to sudden decorrelation.

Further example of images manually acquired using the endoscope are shown in Fig. 3.10. *En-face* and fluorescence images are shown from porcine trachea in Fig. 3.10(a), lung in Fig. 3.10(b) and oesophagus in Fig. 3.10(c). The tissue was prepared and stained as before, with the difference that, in order to simulate a typical

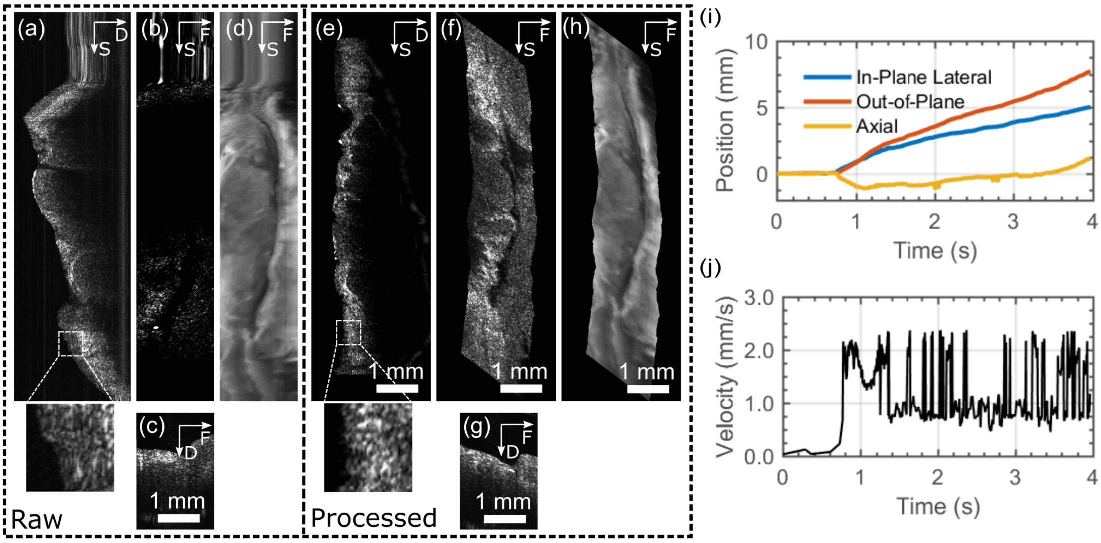

Figure 3.9: Example reconstruction from manual acquisition using endoscope for slow-axis scanning over porcine lung tissue. The raw volume is represented in (a), (b) and (c), which shows a B-scan along the slow-scan direction (a), an *en-face* slice (b) and a B-scan along the fast-scan direction (i.e. a raw B-scan) (c). The raw fluorescence data is also shown in (d). The reconstructed OCT volume is shown in (e), (f) and (g), which again shows a slow-axis B-scan (e), an *en-face* view (f) and a fast-axis B-scan (g). The reconstructed fluorescence is shown in (h). The *en-face* and fluorescence images have been rotated by 37° for display purposes. The insets show zooms on parts of the slow-axis B-scans, where the improved uniformity of the speckle pattern can clearly be seen in the processed image. Labeled arrows indicate the directions of the fast lateral (F) and slow manual lateral (S) scans and axial depth (D). The in-plane lateral, out-of-plane lateral and axial shifts detected by the algorithm are shown in (i), and the measured out-of-plane speed is shown in (j). (a) and (b) are at the same horizontal scale as the other images, but have no vertical scale since the vertical position corresponds to the time of acquisition of each B-scan. Raw data and reconstruction code is available in Ref. [41].

usage scenario for this probe, we ran the probe through a plastic tube with an inner diameter of 12 mm, which was placed against the opened and pinned stained tissue. All three sets of images are shown at the same scale, except for the zoom insets which show an area of 1 mm x 1 mm.

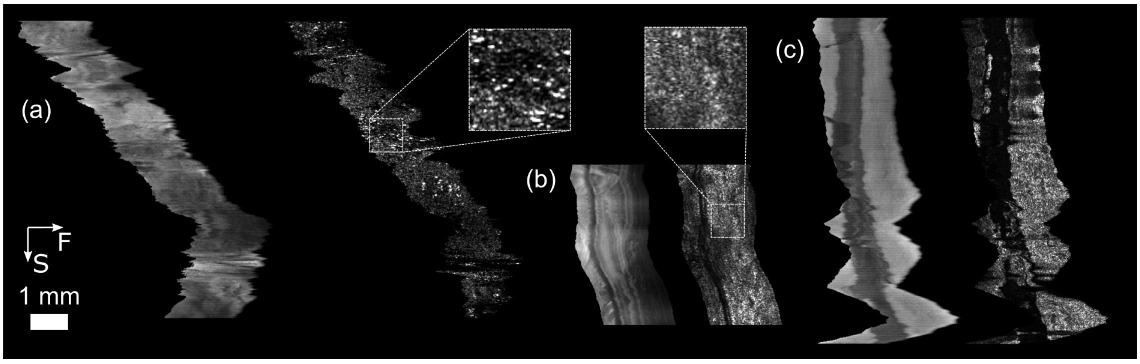

Figure 3.10: Representative pairs of fluorescence (left) and OCT images (right) from porcine *ex vivo* tissue generated when using an endoscope and manual acquisition for the slow-axis scanning. (a) Lung, (b) oesophagus, and (c) trachea. The samples were stained with acriflavine hydrochloride for 2 minutes and then rinsed prior to imaging. *En-face* slices were manually selected for display from reconstructed volumes. For display purposes, *en-face* OCT slices were contrast adjusted using the ImageJ auto-contrast tool. Fluorescence images were auto-contrasted to show the full dynamic range of the image. Zoomed insets show 1 x 1 mm regions. Arrows show direction of fast lateral (F) and slow manual endoscope (S) scans.

3.5 Discussion and Conclusions

We have demonstrated the feasibility of using a conventional endoscope to provide the slow-axis scan for simultaneous 3D OCT and fluorescence endoscopic imaging. In experiments designed to simulate clinical imaging, slow-axis scans over ranges of up to 1 cm were performed, and *en-face* images successfully reconstructed using the speckle decorrelation and registration algorithms. While some image artifacts are often present, and the method is not robust to certain kinds of motion, the *en-face* images generally appear congruent and are much larger in the slow-scan direction than could be achieved using any miniaturized 2D endoscopic scanning mechanism. The probe was validated only using tissue labelled with a fluorescent contrast agent;

further work will be required to evaluate the SNR for applications requiring imaging of intrinsic fluorescence.

Importantly, the method does not require any additional tracking systems, potentially simplifying clinical translation by allowing for more straightforward integration with existing clinical workflows. This is in comparison to other methods of tracking freehand-scanned probes such as with cameras [42], optical encoders [43] or magnetic tracking systems [44].

The reconstruction performance is primarily limited by the fast-axis scanning rate of the endoscopic OCT probe. With a B-scan frame rate of 250 Hz and a lateral resolution of approximately 20 µm, the (manual) slow-axis scan is limited to a speed of approximately 2.5 mm/s before under-sampling and hence degradation of the lateral resolution in the out-of-plane direction. The resolution determined in section 3.3.1 can therefore be considered a best case given that the probe was translated at a constant speed below this threshold. At speeds greater than 5 mm/s the adjacent B-scans will be almost entirely decorrelated and it is no longer possible to estimate the speed correctly. These scanning speeds are rather low and may be difficult to achieve in clinical practice. However, a relatively modest increase in the speed of the B-scan frame, for example to 1 kHz (which is technically feasible), would increase the permitted scanning speed to between 10 mm/s and 20 mm/s. The maximum speed is therefore not a limitation of the approach in general. However, sudden or jerky motion during a scan will also lead to missed areas of tissue, and even with very high fast-axis scanning speeds it is unlikely that these artifacts could be avoided entirely.

The manual slow-scan direction must be roughly perpendicular to the fast-scan direction. While some in-plane motion parallel to the fast-scan direction can be tolerated, and is corrected by the registration procedure, large amounts of in-plane motion will reduce the accuracy of the speckle decorrelation algorithm and lead to a smaller area of tissue being imaged. It would therefore not be possible to simply insert the OCT probe into the working channel of an endoscope; there would need to be some way to check that the orientation aligns with one axis of the endoscope bending motion. This could be intrinsic, through mechanical design forcing the probe to be inserted correctly, or by visualizing the fluorescence excitation on the endoscope camera view and manually rotating the probe. Alternatively, it may be desirable to permanently build the OCT probe into the endoscope, it which case the alignment would be fixed during manufacture.

The speckle decorrelation algorithm cannot detect a change in the direction of the out-of-plane motion. While in principle the endoscope operator could ensure that the endoscope is translated only along a single direction during the scan, patient motion or inadvertent endoscope motion could result in the same area of tissue being scanned over more than once. However, it may be possible to detect and remove these occurrences through image analysis, and real-time display would help the operator to identify when they have occurred.

These limitations are partially mitigated by allowing the operator to see the *en-face* image being assembled in real-time, providing visual feedback on the scanning speed and direction and allowing any errors to be more easily identified as they occur. We have demonstrated that the algorithm is computationally inexpensive and can readily be applied in real-time for a B-scan rate of 250 Hz. To allow for higher frame rates, Complex Master-Slave OCT could be used to reconstruct only a limited axial range around the known surface height.

We have therefore shown that manual slow-axis scanning in combination with correlation-based probe tracking is a promising approach for endoscopic forward-viewing OCT and fluorescence imaging. The validation studies reported here make use of simple phantoms that do not accurately simulate patient anatomy, using relatively large lumens. The true target anatomy will influence the range and stability of endoscope motion, and patient motion will also introduce an additional challenge to motion correction. The next steps in development should therefore involve more extensive studies using more realistic phantoms incorporating simulated patient motion, or animal models. To aid these further investigations, we have made the code for reconstructing OCT volumes and fluorescence images available with this report.

The approach may also have other applications, such as for lower-cost hand-held probes for external body imaging or industrial inspection and non-destructive testing. Alternatively, it may be applied to endoscopic probes designed to be operated with mechanical or robotic scanning systems (such as robotic surgical systems). Indeed, for robotic systems it should be possible to use the speed estimation from the OCT speckle decorrelation for closed-loop robot control, leading to more precise and controlled imaging.

References

1. Marques, M. J. *et al.* Endoscopic en-face optical coherence tomography and fluorescence imaging using correlation-based probe tracking. *Biomed. Opt. Express* **13,** 761–776. `https://opg.optica.org/boe/abstract.cfm?URI=boe-13-2-761` (Feb. 2022).
2. Tearney, G. J. *et al.* Scanning single-mode fiber optic catheter–endoscope for optical coherence tomography. EN. *Optics Letters* **21,** 543–545. ISSN: 1539-4794. `https://www.osapublishing.org/ol/abstract.cfm?uri=ol-21-7-543` (2021) (Apr. 1996).
3. Huang, D. *et al.* Optical coherence tomography. *Science* **254,** 1178–1181 (1991).
4. Gora, M. J., Suter, M. J., Tearney, G. J. & Li, X. Endoscopic optical coherence tomography: technologies and clinical applications [Invited]. en. *Biomedical Optics Express* **8,** 2405. ISSN: 2156-7085, 2156-7085. `https://www.osapublishing.org/abstract.cfm?URI=boe-8-5-2405` (2021) (May 2017).
5. Rollins, A. M. *et al.* Real-time in vivo imaging of human gastrointestinal ultrastructure by use of endoscopic optical coherence tomography with a novel efficient interferometer design. EN. *Optics Letters* **24,** 1358–1360. ISSN: 1539-4794. `https://www.osapublishing.org/ol/abstract.cfm?uri=ol-24-19-1358` (2021) (Oct. 1999).
6. Mavadia-Shukla, J. *et al.* High-speed, ultrahigh-resolution distal scanning OCT endoscopy at 800 nm for in vivo imaging of colon tumorigenesis on murine models. en. *Biomedical Optics Express* **9,** 3731. ISSN: 2156-7085, 2156-7085.

`https://www.osapublishing.org/abstract.cfm?URI=boe-9-8-3731` (2021) (Aug. 2018).

7. Tran, P. H., Mukai, D. S., Brenner, M. & Chen, Z. In vivo endoscopic optical coherence tomography by use of a rotational microelectromechanical system probe. EN. *Optics Letters* **29,** 1236–1238. ISSN: 1539-4794. `https://www.osapublishing.org/ol/abstract.cfm?uri=ol-29-11-1236` (2021) (June 2004).
8. Tsai, T.-H. *et al.* Ultrahigh speed endoscopic optical coherence tomography using micromotor imaging catheter and VCSEL technology. EN. *Biomedical Optics Express* **4,** 1119–1132. ISSN: 2156-7085. `https://www.osapublishing.org/boe/abstract.cfm?uri=boe-4-7-1119` (2021) (July 2013).
9. Wang, T. *et al.* Heartbeat OCT: in vivo intravascular megahertz-optical coherence tomography. EN. *Biomedical Optics Express* **6,** 5021–5032. ISSN: 2156-7085. `https://www.osapublishing.org/boe/abstract.cfm?uri=boe-6-12-5021` (2021) (Dec. 2015).
10. Sharma, U. & Kang, J. U. Common-path optical coherence tomography with side-viewing bare fiber probe for endoscopic optical coherence tomography. *Rev. Sci. Instrum.* **78,** 113102. ISSN: 0034-6748. `https://aip.scitation.org/doi/abs/10.1063/1.2804112` (2021) (Nov. 1, 2007).
11. Gora, M. J. *et al.* Tethered capsule endomicroscopy enables less invasive imaging of gastrointestinal tract microstructure. *Nat. Medicine* **19,** 238–240 (2013).
12. Li, X., Chudoba, C., Ko, T., Pitris, C. & Fujimoto, J. G. Imaging needle for optical coherence tomography. EN. *Optics Letters* **25,** 1520–1522. ISSN: 1539-4794. `https://www.osapublishing.org/ol/abstract.cfm?uri=ol-25-20-1520` (2021) (Oct. 2000).

13. Liu, X., Cobb, M. J., Chen, Y., Kimmey, M. B. & Li, X. Rapid-scanning forward-imaging miniature endoscope for real-time optical coherence tomography. EN. *Optics Letters* **29,** 1763–1765. ISSN: 1539-4794. `https://www.osapublishing.org/ol/abstract.cfm?uri=ol-29-15-1763` (2021) (Aug. 2004).

14. Schulz-Hildebrandt, H. *et al.* High-speed fiber scanning endoscope for volumetric multi-megahertz optical coherence tomography. EN. *Optics Letters* **43,** 4386–4389. ISSN: 1539-4794. `https://www.osapublishing.org/ol/abstract.cfm?uri=ol-43-18-4386` (2021) (Sept. 2018).

15. Jung, W. *et al.* Three-dimensional endoscopic optical coherence tomography by use of a two-axis microelectromechanical scanning mirror. *Applied Physics Letters* **88,** 163901. ISSN: 0003-6951. `https://aip.scitation.org/doi/full/10.1063/1.2195092` (2021) (Apr. 2006).

16. Liang, K. *et al.* Ultrahigh speed en face OCT capsule for endoscopic imaging. EN. *Biomedical Optics Express* **6,** 1146–1163. ISSN: 2156-7085. `https://www.osapublishing.org/boe/abstract.cfm?uri=boe-6-4-1146` (2021) (Apr. 2015).

17. Wurster, L. M. *et al.* Endoscopic optical coherence tomography angiography using a forward imaging piezo scanner probe. en. *Journal of Biophotonics* **12,** e201800382. ISSN: 1864-0648. `https://onlinelibrary.wiley.com/doi/abs/10.1002/jbio.201800382` (2021) (2019).

18. Wu, T. *et al.* Miniaturized precalibration-based Lissajous scanning fiber probe for high speed endoscopic optical coherence tomography. EN. *Optics Letters* **45,** 2470–2473. ISSN: 1539-4794. `https://www.osapublishing.org/ol/abstract.cfm?uri=ol-45-8-2470` (2021) (Apr. 2020).

19. Huo, L., Xi, J., Wu, Y. & Li, X. Forward-viewing resonant fiber-optic scanning endoscope of appropriate scanning speed for 3D OCT imaging. EN. *Optics Express* **18,** 14375–14384. ISSN: 1094-4087. `https://www.osapublishing.org/oe/abstract.cfm?uri=oe-18-14-14375` (2021) (July 2010).

20. Sun, C. *et al. Neurosurgical hand-held optical coherence tomography (OCT) forward-viewing probe* in *Photonic Therapeutics and Diagnostics VIII* **8207** (SPIE, Feb. 2012), 689–696. `https://www.spiedigitallibrary.org/conference-proceedings-of-spie/8207/82074V/Neurosurgical-hand-held-optical-coherence-tomography-OCT-forward-viewing-probe/.full` (2021).

21. Marques, M. J. *et al.* En-face optical coherence tomography/fluorescence endomicroscopy for minimally invasive imaging using a robotic scanner. *J. Biomed. Opt.* **24,** 066006 (2019).

22. Tuthill, T. A., Krücker, J., Fowlkes, J. B. & Carson, P. L. Automated three-dimensional US frame positioning computed from elevational speckle decorrelation. *Radiology* **209,** 575–582 (1998).

23. Ahmad, A., Adie, S. G., Chaney, E. J., Sharma, U. & Boppart, S. A. Cross-correlation-based image acquisition technique for manually-scanned optical coherence tomography. eng. *Optics Express* **17,** 8125–8136. ISSN: 1094-4087 (May 2009).

24. Liu, X., Huang, Y. & Kang, J. U. Distortion-free freehand-scanning OCT implemented with real-time scanning speed variance correction. EN. *Optics Express* **20,** 16567–16583. ISSN: 1094-4087. `https://www.osapublishing.org/oe/abstract.cfm?uri=oe-20-15-16567` (2020) (July 2012).

25. Wang, Y. *et al.* Robust motion tracking based on adaptive speckle decorrelation analysis of OCT signal. EN. *Biomedical Optics Express* **6,** 4302–4316. ISSN:

2156-7085. `https://www.osapublishing.org/boe/abstract.cfm?uri=boe-6-11-4302` (2020) (Nov. 2015).

26. Uribe-Patarroyo, N. & Bouma, B. E. Rotational distortion correction in endoscopic optical coherence tomography based on speckle decorrelation. EN. *Optics Letters* **40,** 5518–5521. ISSN: 1539-4794. `https://www.osapublishing.org/ol/abstract.cfm?uri=ol-40-23-5518` (2020) (Dec. 2015).
27. Abouei, E. *et al.* Correction of motion artifacts in endoscopic optical coherence tomography and autofluorescence images based on azimuthal en face image registration. *J. Biomed. Opt.* **23,** 016004 (2018).
28. Sun, C. *et al.* In vivo feasibility of endovascular Doppler optical coherence tomography. EN. *Biomedical Optics Express* **3,** 2600–2610. ISSN: 2156-7085. `https://www.osapublishing.org/boe/abstract.cfm?uri=boe-3-10-2600` (2021) (Oct. 2012).
29. Ahsen, O. O. *et al.* Correction of rotational distortion for catheter-based en face OCT and OCT angiography. EN. *Optics Letters* **39,** 5973–5976. ISSN: 1539-4794. `https://www.osapublishing.org/ol/abstract.cfm?uri=ol-39-20-5973` (2021) (Oct. 2014).
30. Lee, A. M. D., Hohert, G., Angkiriwang, P. T., MacAulay, C. & Lane, P. Dual-beam manually-actuated distortion-corrected imaging (DMDI) with micromotor catheters. EN. *Optics Express* **25,** 22164–22177. ISSN: 1094-4087. `https://www.osapublishing.org/oe/abstract.cfm?uri=oe-25-18-22164` (2021) (Sept. 2017).
31. Harlow, M., MacAulay, C., Lane, P. & Lee, A. M. D. Dual-beam manually actuated distortion-corrected imaging (DMDI): two dimensional scanning with a single-axis galvanometer. EN. *Optics Express* **26,** 18758–18772. ISSN: 1094-

4087. `https://www.osapublishing.org/oe/abstract.cfm?uri=oe-26-14-18758` (2020) (July 2018).

32. Nguyen, T. H. *et al.* Correction of circumferential and longitudinal motion distortion in high-speed catheter/endoscope-based optical coherence tomography. EN. *Biomedical Optics Express* **12,** 226–246. ISSN: 2156-7085. `https://www.osapublishing.org/boe/abstract.cfm?uri=boe-12-1-226` (2021) (Jan. 2021).
33. Scolaro, L. *et al.* Molecular imaging needles: dual-modality optical coherence tomography and fluorescence imaging of labeled antibodies deep in tissue. en. *Biomedical Optics Express* **6,** 1767. ISSN: 2156-7085, 2156-7085. `https://www.osapublishing.org/abstract.cfm?URI=boe-6-5-1767` (2019) (May 2015).
34. Feldchtein, F. I., Gelikonov, V. M. & Gelikonov, G. V. in *Handbook of Optical Coherence Tomography* (eds Bouma, B. E. & Tearney, G. J.) 125–142 (Marcel Dekker, 2001).
35. Cernat, R. *et al.* Dual instrument for in vivo and ex vivo OCT imaging in an ENT department. en. *Biomedical Optics Express* **3,** 3346. ISSN: 2156-7085, 2156-7085. `https://www.osapublishing.org/boe/abstract.cfm?uri=boe-3-12-3346` (2020) (Dec. 2012).
36. Rivet, S. *et al.* Complex master slave interferometry. en. *Optics Express* **24,** 2885. ISSN: 1094-4087. `https://www.osapublishing.org/abstract.cfm?URI=oe-24-3-2885` (2019) (Feb. 2016).
37. Bradu, A., Maria, M. & Podoleanu, A. G. Demonstration of tolerance to dispersion of master/slave interferometry. en. *Optics Express* **23,** 14148. ISSN: 1094-4087. `https://www.osapublishing.org/abstract.cfm?URI=oe-23-11-14148` (2019) (June 2015).

38. Marques, M. J., Rivet, S., Bradu, A. & Podoleanu, A. Complex master-slave for long axial range swept-source optical coherence tomography. en. *OSA Continuum* **1,** 1251. ISSN: 2578-7519. `https://www.osapublishing.org/abstract.cfm?URI=osac-1-4-1251` (2019) (Dec. 2018).

39. Bradu, A. *et al.* Recovering distance information in spectral domain interferometry. en. *Scientific Reports* **8,** 15445. ISSN: 2045-2322. `http://www.nature.com/articles/s41598-018-33821-0` (2019) (Dec. 2018).

40. Hughes, M. R. *En-face optical coherence tomography and fluorescence imaging using correlation-based probe tracking - LabVIEW Code* `https://doi.org/10.6084/m9.figshare.16579007` (2021).

41. Hughes, M. R. *En-face optical coherence tomography and fluorescence imaging using correlation-based probe tracking - Matlab Code and Data* `https://doi.org/10.6084/m9.figshare.16578953` (2021).

42. Ren, J., Wu, J., McDowell, E. J. & Yang, C. Manual-scanning optical coherence tomography probe based on position tracking. EN. *Optics Letters* **34,** 3400–3402. ISSN: 1539-4794. `https://www.osapublishing.org/ol/abstract.cfm?uri=ol-34-21-3400` (2021) (Nov. 2009).

43. Iftimia, N. *et al.* Hand scanning optical coherence tomography imaging using encoder feedback. EN. *Optics Letters* **39,** 6807–6810. ISSN: 1539-4794. `https://www.osapublishing.org/ol/abstract.cfm?uri=ol-39-24-6807` (2020) (Dec. 2014).

44. Yeo, B. Y., McLaughlin, R. A., Kirk, R. W. & Sampson, D. D. Enabling freehand lateral scanning of optical coherence tomography needle probes with a magnetic tracking system. EN. *Biomedical Optics Express* **3,** 1565–1578. ISSN: 2156-7085. `https://www.osapublishing.org/boe/abstract.cfm?uri=boe-3-7-1565` (2021) (July 2012).

Chapter 4

Axial Tracking for a MS-OCT system

Author's note: Some of the work presented here led to a peer reviewed article under the conference proceedings "Non-mechanical Axial Motion Compensation Using Master-Slave Optical Coherence Tomography" [1] and patent registered as US 2021/0145285 A1 with Prof. Adrian Podoleanu. The chapter has been expanded with more material related to both publications, with all work presented in this chapter being performed by the author.

4.1 Introduction

As a non-invasive, contactless imaging technique, OCT has become almost a standard procedure in ophthalmology, used for the monitoring and study of visual function as well as diseases and other ocular conditions. Nonetheless, as discussed in previous chapters, stabilization of the sample to be observed is required in order to acquire a well-resolved image, free of any motion artefacts, but due to the nature of *in-vivo* samples, such as the human retina, it is impossible to ensure its complete immobilization, thus being necessary to accurately compensate its inherent motion.

While movements during the acquisition of an A-scan are rare due to the A-scan acquisition rate in modern OCT systems, motion artefacts can be an issue to account for in B-scans and *en-face* images, since despite some recent research achieving ultrahigh speeds, most commercially available sources range between 70 kHz and 100 kHz.

Most of the approaches to this problem can be categorised as mechanical or software-based solutions. While both may acquire the axial position of the sample by using a secondary imaging system of sorts, mechanical-based systems relay more often on them, feeding the axial position of the sample into a mechanical element, like a voice coil translation stage [2, 3] or a rapid scanning optical delay line [4], within the reference arm of the imaging interferometer to change its OPD and match the sample arm. They are characterised for being particularly accurate without any loss of sensitivity, but the extra motorised components raise costs and may suffer from inertia, as well as the inherent electrical response delay.

Software-based systems tend to follow a model of the movement or to analyse the changes between two acquisitions to decode the displacement experienced by the sample and compensate it in the images acquired, in some cases analysing the phase variance between spectra [5], correcting even intra A-scan. Some approaches involve analysing the variation rate between adjacent A-scans between two adjacent B-scans [6, 7], in other words, the A-scan at the same x coordinate after a step in the y axis. In angiography, it has been reported a method to calculate the axial displacement due to the Doppler shift in the blood vessels [8]. Software approaches tend to estimate the motion by comparison and sometimes cause flattening, but in this example, the motion is calculated more accurately and the surface shape was preserved, but the algorithm reported was a correlation-based algorithm with a histogram approach that reduced the accuracy of the correction and had some image degradation.

In this chapter a new axial motion compensation method based on the properties of MS-OCT is presented, taking advantage of the stored masks prior to examination. While lacking any mechanical element in the reference arm to compensate for the motion, a second interferometer is used as in conventional mechanical approaches in order to determine the axial displacement of the sample. This displacement is then used to modify the masks used for MS-OCT, mimicking the effect of physically displacing the reference arm to match the sample arm. For the validation of the method, two configurations will be explored, one intended for skin imaging and other for eye imaging, called configuration (s) and configuration (e). While these same configurations are used in Chapter 5, in this chapter we refer to this configurations for both the Imaging sub-system (IS) and Tracking sub-system (TS).

4.2 System description

The OCT set-up here presented combines two interferometers, referred to as Tracking sub-system (TS) and Imaging sub-system (IS), that share part of their respective sample arms. Both sub-systems use swept sources as the optical source, with the TS being a non-scanning SS-OCT, employing FFT to decode the A-scan, and the IS functioning as a point-scanning MS-OCT.

The TS Source is a 1300 nm swept source with a 10 kHz sweeping frequency (Santec HSL-2000-12-MDL). The resulting modulated spectra is detected by a balanced photodetector (BPD) with a 200 MHz cut-off frequency, and the corresponding electrical signal is digitised into the computer via a National Instruments PCI-5124 card with a 25 MS/s sweeping rate.

For the IS, the swept source is a Superlum Broadsweeper 840, with a sweeping rate of 2 kHz and centre wavelength of 850 nm and a tuning range of 50 nm. The resulting modulated spectra are detected by a custom-made BPD with a 1 MHz cut-off frequency and the corresponding electrical signal is digitised via an AlazarTech ATS0350 acquisition card, sampling at 2 MS/s. By setting appropriate spectral tuning ranges, both sub-systems have the same axial resolution in air of 6.7 µm.

In order to correct the axial motion artefacts of a given sample, 4 consecutive

A-scans of the TS are averaged together, and then the relative depth within the A-scan at which the main maximum is observed is sent as α to the IS processing module. In the IS, an arbitrary set of masks is pre-generated, with only a subset made of a p number of consecutive masks being used for the MS-OCT processing.

By shifting the subset of masks by α we recreate the same effect as applying a physical offset in the OPD by varying the reference arm length, with the downside of not improving the sensitivity back to values closer to OPD=0. A representative graph of this process is shown in Fig. 4.1.

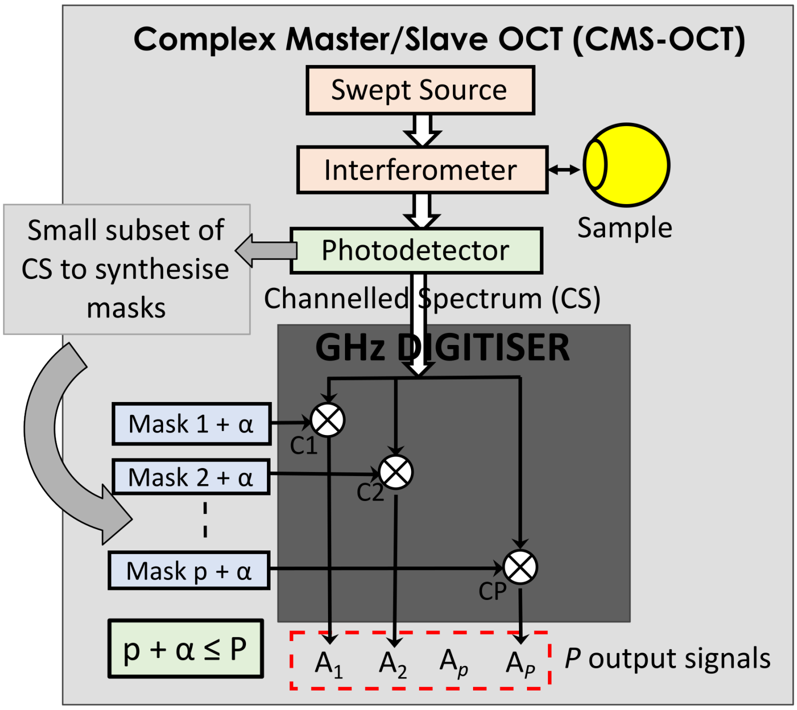

Figure 4.1: Schematic diagram of the modification over MS-OCT in the IS.

This principle of motion compensation via a shift of the subset of masks employed in MS-OCT was tested on two different applications: Dermal imaging and Retinal imaging, called configuration (s) and configuration (e).

4.2.1 Configuration (s)

For dermal applications, a configuration was devised in which both sample arms of each sub-system focuses on the same layer of the sample under investigation. A Dichroic filter is implemented in between the telescope in the Interface optics of the IS to avoid astigmatism in the IS. A schematic diagram is presented in Fig. 4.2.

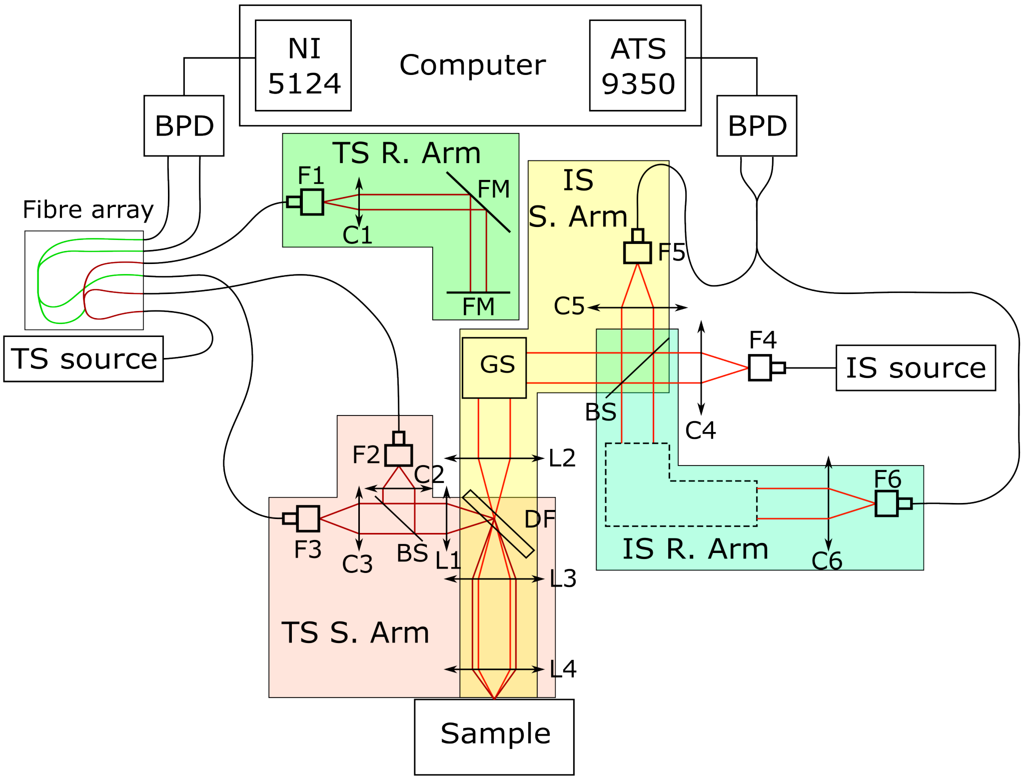

Figure 4.2: Schematic representation of the two sub-systems, TS and IS, for skin imaging. The fibre array can be considered as 2 connected fibre couplers, with the coupler represented in green as a 50/50 coupler, receiving inputs from reference and sample arms, while outputting to the BPD, and another red coupler as an 75/25 coupler with the 25% power sent to the sample arm. BPD: Balanced photodetector; BS: Beamsplitter; DF: Dichroic filter; C1-6: Collimators; F1-6: Fibre mounts; FM: Flat mirror; GS: Galvanometer scanners; TS: Tracking sub-system; IS: Imaging sub-system.

4.2.2 Configuration (e)

For Retinal applications, the L1 and L4 from 4.2 are removed. By removing L1 lens, the incident beam of the TS at the dichroic filter is now collimated, while the beam from the IS is focused, and by removing L4, the beam from the IS enters into the eye collimated, focusing on retina, while the TS beam focuses on the cornea. Assuming the eye moving as a bulk, this configuration allows to remove artefacts caused by head and breathing, while retaining those caused by blood flow or other internal processes, which can be beneficial in some applications.

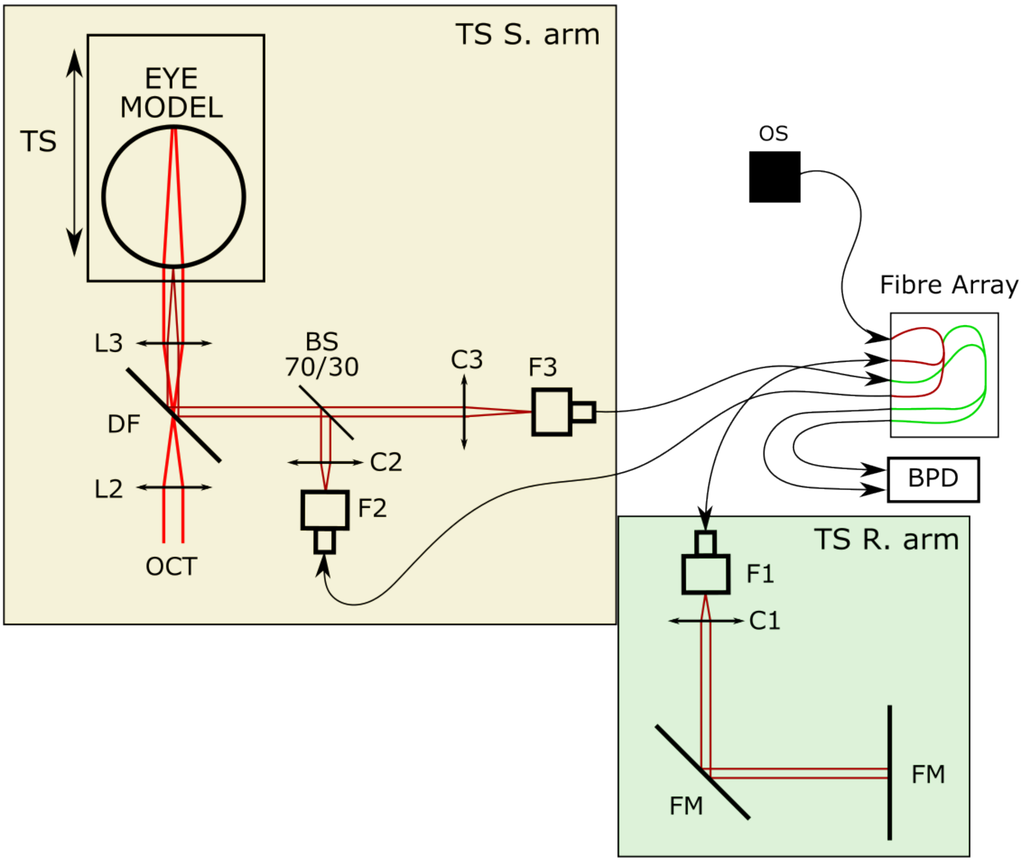

Figure 4.3: Schematic representation of the modified section of the sample arm of both sub-systems. In comparison with Fig. 4.2, L1 and L4 have been removed, so that the beam from the TS focuses on the cornea while the beam from the IS focuses on retina.

4.3 Results

Both configurations previously described can operate in Real-time or in Post-processing mode, since the axial position of the sample is stored at the same time as the channelled spectra.

4.3.1 Volumetric post-processing motion compensation

Figures 4.4 and 4.5 presents the results obtained on the (s) and (e) configurations respectively. In the case of skin, a thumb of a healthy volunteer was used as a sample. In order to keep the thumb within the coherence gate of the set-up while allowing some motion, the volunteer positioned their finger over a hollow optical mount and held the thumb vertical, with no support on the top area of the thumb. Since there was no control over lateral motion artefacts, only M-mode was used to prove the method.

For the configuration (e), the signal *in-vivo* from the cornea of a volunteer turned out to be too unstable and the tracking signal was lost most of the time. In order to still test the functionality of the correction, a retina model from ROWE Technical Design, Inc. [9] was mounted on top of a translation stage at the sample plane. At the beginning of the acquisition, the stage remained stationary, and midway during the volume acquisition, a triangular signal was applied to the stage, creating a ripple effect on the images.

4.3.2 Real-time compensation for single depth ***En-face*** imaging

The previous post-processing results can be applied to any type of OCT processing, as the offset α can be sent to a FFT processing unit and correct for such an offset.

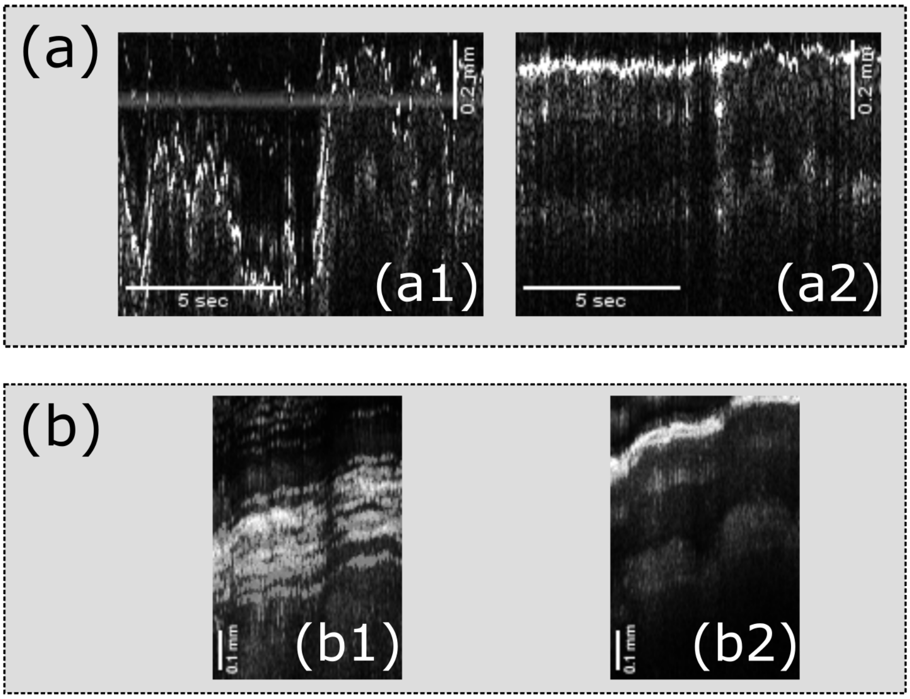

Figure 4.4: Results obtained from an *in-vivo* skin sample of the thumb of a healthy volunteer. The motion artefacts have been corrected post-processing. IS is operating in M-mode, acquiring approximately 10 seconds of A-scans of about 1 mm depth. in (a) the full volume is represented while in (b) the standard deviation of the whole set is calculated. The raw data is presented on the left, as (a1) and (b1), while the corrected images are on the right, as (a2) and (b2).

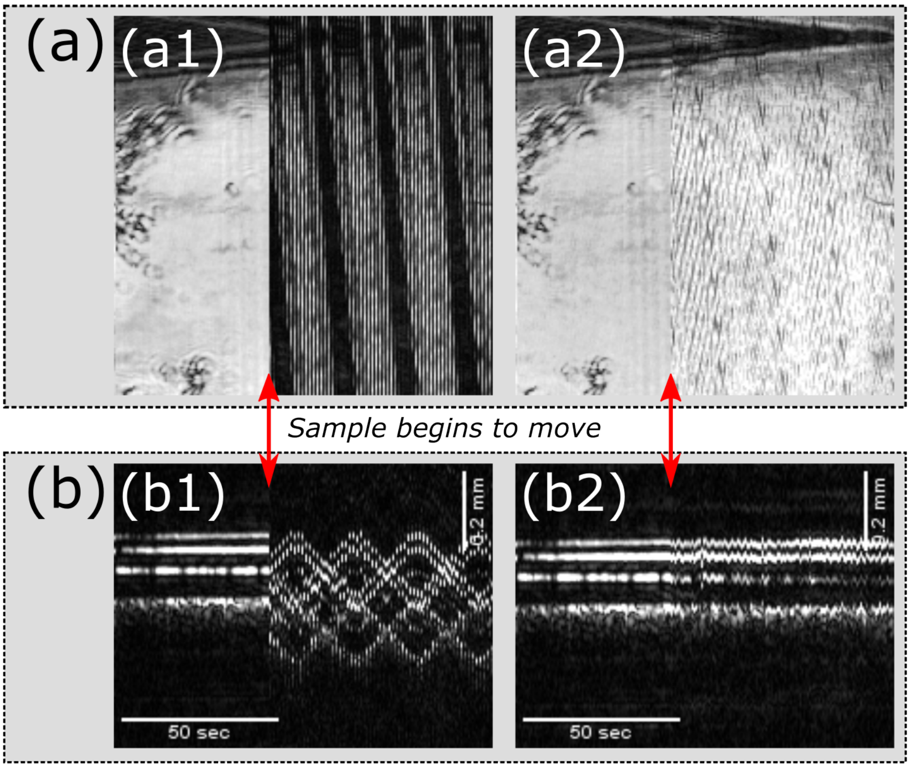

Figure 4.5: Results obtained from a ROWE retina model mounted on a motorised linear translation stage, with (a) corresponding to the *en-face* view of the volume while (b) are B-scans at the same vertical coordinate. At the beginning of the acquisition of the volume the translation stage is stationary, and a triangle function is applied to the stage mid-acquisition. As in 4.4, on the left are the raw results, as (a1) and (b1), while on the right the corrected dataset is presented as (a2) and (b2). Small high frequency artefacts remain after correction due to lateral vibrations caused by the motorised stage.

Nonetheless, as MS-OCT allows for the acquisition of *en-face* images without the acquisition of the whole volume, real-time imaging can be performed even at a 2 kHz sweeping rate.

With the TS offering depth control per A-scan, the mask used for the MS-OCT processing at each lateral position of the *en-face* can be individually selected, creating a reconstructed *en-face* of the correct depth, but with variable sensitivity across the x and y axis, proportional to the amount of axial displacement. Since the real-time regime is obtained with a video recording, Fig. 4.6 presents a snapshot of the thumb of a healthy volunteer in the same conditions as previously presented. This *en-face* has been obtained by averaging 10 adjacent depths, removing all artefacts up to roughly 60 µm. On the middle to bottom sections of the image can be observed what seems to be sweat ducts, while the dark section on the top is due to the curvature of the thumb going out of that depth.

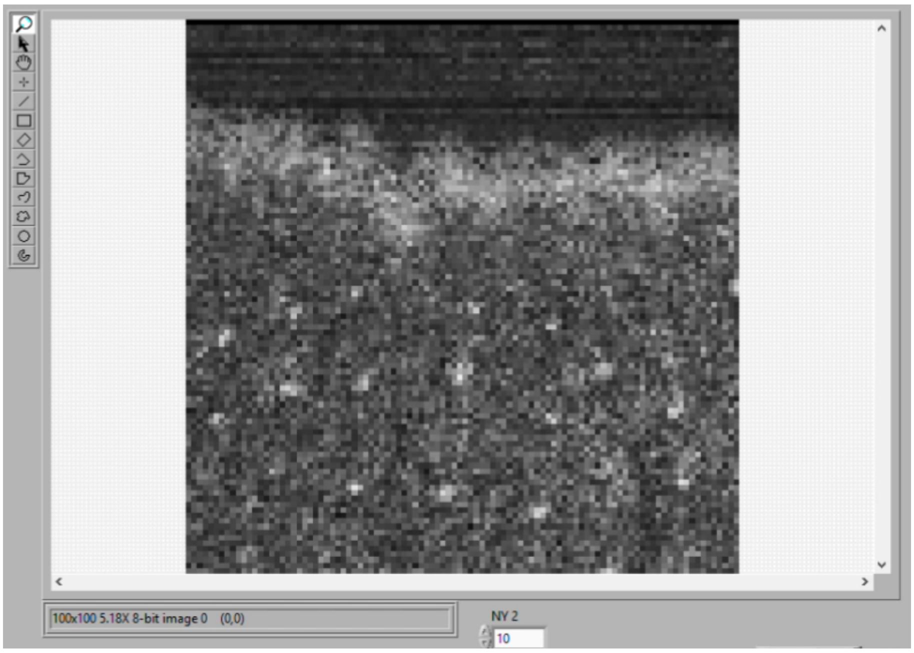

100x100 5.18X 8-bit image 0 (0,0)

NY 2
10

Figure 4.6: Snapshot of a recording of an *en-face* exploration of the thumb of a healthy volunteer acquired in real-time. Sweat ducts can be observed in the image.

4.4 Conclusions

Master-Slave OCT seem to offer new avenues to tackle artefacts related to the axial motion experienced by the sample, as the results on skin samples were really promising, with the real-time implementation for *en-face* images being its greatest advantage. While the methodology itself is not dependant on the physical configuration of the interferometer employed in the TS, as the results with the retina model showcase, the method here presented should be validated *in-vivo*.

While a free space OCT set-up might not offer much interest for dermal imaging, the artefact correction methodology can be implemented in endoscopic probes, as the TS and IS can share most of the sample arms pathways. Special attention must be taken when designing an application in delicate samples as the TS beam is stationary and could cause damages on the tissue.

References

1. Fernández, A., Marques, M. J., Bradu, A. & Podoleanu, A. *Non-mechanical Axial Motion Compensation Using Master-Slave Optical Coherence Tomography* in *Biophotonics Congress: Biomedical Optics 2020 (Translational, Microscopy, OCT, OTS, BRAIN)* (Optica Publishing Group, 2020), OTu1E.6. `https://opg.optica.org/abstract.cfm?URI=OCT-2020-OTu1E.6`.
2. Pircher, M., Baumann, B., Götzinger, E., Sattmann, H. & Hitzenberger, C. K. Simultaneous SLO/OCT imaging of the human retina with axial eye motion correction. *Opt. Express* **15,** 16922–16932. `https://opg.optica.org/oe/abstract.cfm?URI=oe-15-25-16922` (Dec. 2007).
3. Zhang, T., Kho, A. M. & Srinivasan, V. J. Improving visible light OCT of the human retina with rapid spectral shaping and axial tracking. *Biomed. Opt. Express* **10,** 2918–2931. `https://opg.optica.org/boe/abstract.cfm?URI=boe-10-6-2918` (June 2019).
4. Pircher, M., Götzinger, E., Sattmann, H., Leitgeb, R. A. & Hitzenberger, C. K. In vivo investigation of human cone photoreceptors with SLO/OCT in combination with 3D motion correction on a cellular level. *Opt. Express* **18,** 13935–13944. `https://opg.optica.org/oe/abstract.cfm?URI=oe-18-13-13935` (June 2010).
5. Hillmann, D. *et al.* Common approach for compensation of axial motion artifacts in swept-source OCT and dispersion in Fourier-domain OCT. *Opt. Ex-*

press **20,** 6761–6776. `https://opg.optica.org/oe/abstract.cfm?URI=oe-20-6-6761` (Mar. 2012).

6. Braaf, B. *et al.* Real-time eye motion correction in phase-resolved OCT angiography with tracking SLO. *Biomed. Opt. Express* **4,** 51–65. `https://opg.optica.org/boe/abstract.cfm?URI=boe-4-1-51` (Jan. 2013).
7. Capps, A. G. *et al. Correction of eye-motion artifacts in AO-OCT data sets* in *Ophthalmic Technologies XXI* (eds Manns, F., Söderberg, P. G. & Ho, A.) **7885** (SPIE, 2011), 78850D. `https://doi.org/10.1117/12.874376`.
8. Makita, S., Hong, Y., Yamanari, M., Yatagai, T. & Yasuno, Y. Optical coherence angiography. *Opt. Express* **14,** 7821–7840. `https://opg.optica.org/oe/abstract.cfm?URI=oe-14-17-7821` (Aug. 2006).
9. Rowe, T. S. *Phantom for rendering biological tissue regions* US Pat. 8,480,230. 2013. `https://patents.justia.com/patent/8480230`.

Chapter 5

Spatial distortions in swept source Optical Coherence Tomography due to lateral scanning

<u>Author's note</u>: All of the work presented here has been peer reviewed under the article "Spatial distortions in swept source optical coherence tomography due to lateral scanning" [1].

5.1 Introduction

The most modern OCT technology is based on processing of the optical spectrum at the interferometer output. In a spectrometer based OCT, this is done via a spectrometer and a broadband source [2, 3]. In Swept Source (SS)-OCT, this is achieved via a balanced photodetector and a tunable laser (a swept source) [4] scanned across the sample.

The chapter presents effects so far ignored in cross section SS-OCT images when performing lateral scanning. They affect the measurement of axial distances as well as the shapes of contours of the sample imaged, especially when the interface optics and the lateral scanner are not properly adjusted.

The importance of proper adjustment of the lateral scanner was identified early in the OCT evolution. Starting with time domain OCT, it was realised that optical path modulation due to lateral scanning can be used to generate *en-face* OCT images with no need of a phase or frequency modulator to create a carrier [5]. It was also known from the same imaging technology that offset position of the incident beam on the lateral scanner leads to optical path variation during scanning. This effect was already used in Newton rings imaging [6], enabling *en-face* OCT without an external phase modulator.

The off-pivot incidence of the beam on the line scanner was also employed in spectral domain OCT for elimination of the mirror terms [7], based on the associated Doppler effect introduced. Doppler frequency shifts due to movement of scattering centres was previously reported [8], however there was no anticipation of image distortion due to Doppler effects.

As consequence, the authors are not aware of any report on spatial errors in OCT along the axial direction due to lateral scanning. This study reports on such effects in a SS-OCT system. We show that incorrect adjustments of the interface optics, otherwise expected to affect lateral resolution performance, can also produce important effects in the axial direction in the A-scans and OCT cross section images (B-scans).

Let us consider a signal applied to the lateral scanner, where for a lateral deviation to address pixel m, the instantaneous voltage (for any shape of the signal, sinusoidal, sawtooth or triangular) is V_m. An axial deviation error (ADE) is introduced for each lateral pixel, m, in the B-scan OCT image, defined as the difference between the position in depth determined with the lateral scanner driven by the variable signal applied to the lateral scanner, and the position in depth determined with the lateral scanner at rest, but driven by a bias voltage $= V_m$.

The results obtained demonstrate that the ADE magnitude depends on the interface optics adjustments and on the number of sweeps within the lateral scanning interval. With reference to the interface optics, off-pivot errors or tilt of sample layers lead to ADE. The larger the amplitude of the lateral scanning, the larger the ADE. The ratio of the lateral scanning duration over the sweep duration gives the number of sweeps per lateral scanning interval. The larger the sweeping frequency in respect to the lateral scanning frequency, the smaller the ADE. For a given sweeping frequency, by increasing the frequency of lateral scanning, the number of sweeps per scanning interval reduces and ADE goes up.

For a given sweeping frequency and lateral scanning frequency, by enlarging the amplitude of the lateral scanning the ADE also goes up. This behaviour suggests a dependence of the ADE on the scanning speed, proportional to the speed of variation of the optical path difference (OPD), that can be altered by either lateral scanning frequency or by its amplitude.

This report also demonstrates that the ADE sign depends on the direction of lateral scanning, as well as on the direction of spectral tuning. The ADE, if not minimised, can lead to distortions of images delivered and to errors in the axial position of sample structure. When the ADE magnitude is larger than the axial resolution interval, this prevents correct superposition of B-scans obtained with both lateral scanning directions, or correct superposition of images obtained using both tuning directions, in case of bidirectional tuning swept sources.

5.2 Theory

The ADE is evaluated experimentally for two cases of flying spot OCT imaging, employing two widely used interface optics in the sample arm of an OCT interferometer, for imaging skin and imaging retina, as shown in Fig. 5.1 (s) and 5.1 (e) respectively. Let us consider a mirror M as an object, and let us see how the B-scan of a mirror is affected by the adjustment of the interface optics in the system as well as by the direction of sweeping in the optical source. For simplicity, a single galvo scanner (GS) is shown.

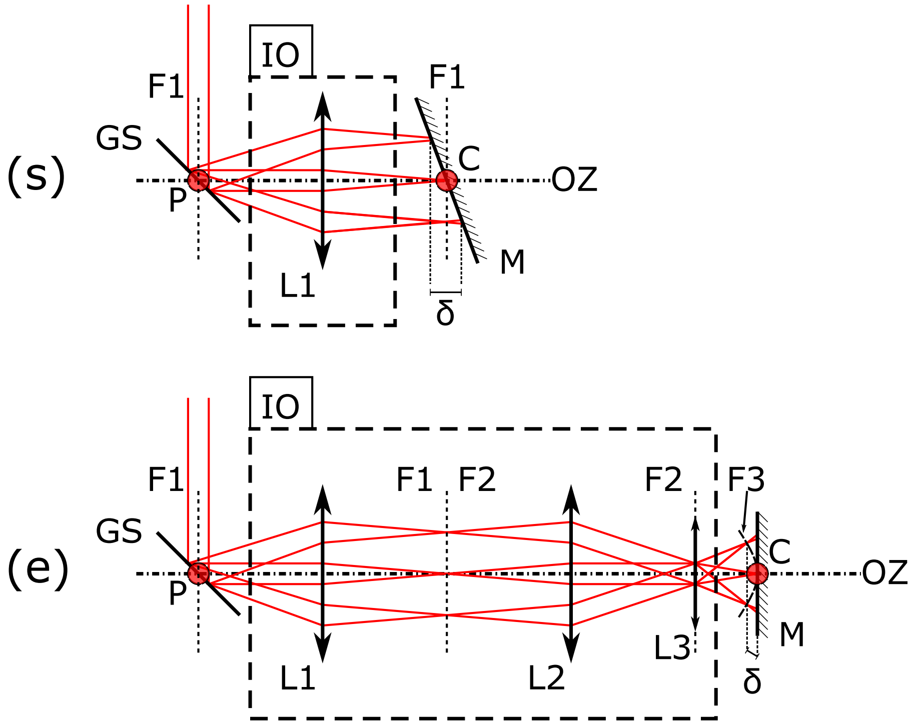

Figure 5.1: Schematic diagrams of the interface optics (IO) used for imaging skin (s) and for imaging retina in an eye (e). GS: Galvanometer scanner; L1, L2, L3: lenses: L3: lens mimicking the focusing effect of the eye lens and cornea; F1, F2, F3: Focal distances corresponding to the lenses L1, L2 and L3; M: mirror; P: Pivot point of the GS; OZ: Optic axis; C: intersection of the axis OZ along depth and the mirror; δ: axial path variation encountered during lateral scanning.

In a first configuration considered, such as that in Fig. 5.1(s), a single lens, L1, of focal length, F1, is used at F1 from the GS pivot, P, with a mirror M placed behind the lens L1 at F1. Let us also consider that the mirror is tilted, obtained by rotation around a direction perpendicular to the sketch plane. At the extremity of lateral scanning, the sample ray travels plus or minus $\delta/2$ distance more than the ray to the point C, of intersection of the mirror with the optics axis, OZ.

In a second configuration, in Fig. 5.1(e), a system composed of 3 lenses is used, placing L1 at F1 from P, L2 is placed at $F1 + F2$ from L1, and L3 is placed at

F2 from L2, being at the conjugate plane of the GS pivot, P. This is the preferred configuration for retina imaging, where the lens L3 plays the cumulative role of the cornea and eye lens of the eye under examination. In this configuration, the OPD variation shown by δ increases with deflection from on-axis, to either side of OZ. In Fig. 5.1(s), the OPD varies linearly with the deflection angle [5]. In Fig. 5.1(e), due to the curvature of the wavefront behind L3, the OPD varies quadratically with the deflection angle [6].

Let us consider the set-up in Fig. 5.1(s) first. When laterally scanning the beam from one side to the other of the sample, for the case of a tilted mirror, M, the speed of OPD variation can be estimated via:

$$v = \frac{\delta}{T} \tag{5.1}$$

where T is the duration of lateral scan from one edge of the scanned arc across the sample to the other edge. The arc scanned is the top of the B-scan, termed here as a 1D directional contour scanned, or a T-scan. A Doppler shift results, similar to the case of moving axially the reference mirror in the reference path, of frequency:

$$F = 2\frac{v}{\lambda} = 2\frac{\delta}{T \cdot \lambda} \tag{5.2}$$

The larger the tilt of the mirror, the larger δ, and the larger the Doppler frequency shift, F. The Doppler frequency shift combines with the frequency of the photodetected signal due to sweeping. For simplicity, let us consider linear variation of the optical frequency with the OPD (not affected by non-linear sweeping or dispersion). For each increase of the OPD by an axial resolution interval, $2a$, the number of peaks in the channelled spectrum, N, increases by one (eq. 22 in [9]). Hence, the number of peaks and troughs in the photodetected signal of the channelled spectrum can be written as:

$$N = \frac{OPD}{2a} \tag{5.3}$$

For N peaks read in the tuning interval τ, the frequency generated by sweeping is:

$$f = \frac{N}{\tau} \tag{5.4}$$

For a Gaussian spectrum shape of FWHM $\Delta\lambda$ in wavelength [10], the axial resolution in depth, a, is given by:

$$a = \frac{2\ln 2}{\pi}\frac{\lambda^2}{\Delta\lambda} \sim 0.44\frac{\lambda^2}{\Delta\lambda} \tag{5a}$$

However, the majority of swept sources exhibit a top hat spectrum shape, in which case the axial resolution interval is given by [11]

$$a \sim 0.6\frac{\lambda^2}{\Delta\lambda} \tag{5b}$$

The number of sweeps during the lateral scanning interval T is:

$$M = \frac{T}{\tau} \tag{5.6}$$

An axial deviation error, ADE, appears in the axial display of the T-scan of a mirror in the B-scan when the extreme point of the lateral angle is at a position along Z exceeding the correct position by more than an axial resolution interval:

$$ADE > a \tag{5.7}$$

This can happen when the Doppler frequency shift due to lateral scanning exceeds the frequency step $1/\tau$ in the spectrum of the photodetected channelled spectrum. For each added axial resolution interval to the OPD, the number of peaks in the channelled spectrum goes up by 1 and the frequency f goes up by $1/\tau$, hence using (5.2):

$$2\frac{\delta}{T\cdot\lambda} > \frac{1}{\tau} \tag{5.8}$$

Then using (5.6):

$$\frac{\delta}{M} > \frac{\lambda}{2} \tag{5.9}$$

In other words, when half of the OPD variation encountered by lateral scanning over a transversal pixel size exceeds half of a wavelength, it is expected that ADE becomes visible.

For good imaging, the number of sweeps in a T-scan, M should exceed several hundreds, however when M becomes so small that (5.9) is satisfied, errors become visible in the B-scan OCT image.

5.2.1 Phase variation

Let us consider the interface optics in Fig. 5.1 as part of the sample arm of an OCT interferometer. Due to lateral scanning with a velocity, v, the sample path length, L_S varies in time over an initial value L_{S0} according to:

$$L_s = L_{s0} + vt \tag{5.10}$$

The reference path length L_R in the OCT interferometer can be written respectively as:

$$L_R = L_{R0} \tag{5.11}$$

where L_{R0} is an initial length kept constant. When the sample beam is directed at $t = 0$ to the top edge of the object in Fig. 5.1 (s), above the centre of the image at C, half of the OPD can be written as:

$$L_{S0} - L_{R0} = z \tag{5.12}$$

whilst the OPD/2 with the beam deviated from the top edge due to lateral scanning is:

$$L_S - L_R = z + vt \tag{5.13}$$

At the extremes of lateral scanning, the axial deviation is $\delta/2$ or $-\delta/2$, separated in time from the moment when the scanning beam hits the point on axis, C, by half the period of the signal driving the galvo scanner (GS), $T/2$. Considering the time t within a τ interval, while the scanning beam is deflected over the pixel m (where m is between 1 and M), an expression can be obtained for the phase of the photodetected signal at the output of the OCT interferometer:

$$\varphi_m(t) = k(t)\left[z + (m-1)\frac{\delta}{M} + \frac{\delta t}{\tau M}\right] \tag{5.14}$$

where the wavenumber variation during each sweep of duration, τ, in time can be written as:

$$k(t) = K_1 + \frac{\Delta K}{\tau} t \tag{5.15}$$

Here K_1 is the initial wavenumber and K_2 is the final wavenumber after a tuning time interval τ

$$\Delta K = K_2 - K_1 \tag{5.16}$$

When tuning from a small wavelength, λ_1 to a large wavelength, λ_2, $\Delta K < 0$ whilst when tuning from a large wavelength to a small wavelength, $\Delta K > 0$. Using

$$\frac{\delta}{M\tau} = \frac{\delta}{T} = v \tag{5.17}$$

(5.14) becomes:

$$\varphi_m(t) = k(t)\left[z + (m-1)\frac{\delta}{M} + vt\right] \tag{5.18}$$

Introducing (5.15) into (5.14) and performing a time derivative, the instantaneous frequency of the photodetected signal is obtained as:

$$\frac{d\varphi_m}{dt} = \frac{\Delta K}{\tau}\left[z + (m-1)\frac{\delta}{M} + vt\right] + k(t)v \tag{5.19}$$

In the middle of a sweeping interval τ corresponding to lateral scanning over the lateral pixel m, i.e. for:

$$t = \frac{\tau}{2} \tag{5.20}$$

(5.19) becomes:

$$\omega_m = \frac{\Delta K}{\tau}\left[z + (m-1)\frac{\delta}{M} + v\frac{\tau}{2}\right] + k\left(\frac{\tau}{2}\right)v \tag{5.21}$$

Given the fact that:

$$k\left(\frac{\tau}{2}\right) = K_1 + \frac{\Delta K}{2} = \frac{K_2 + K_1}{2} = K_c \tag{5.22}$$

where K_c is the central wavenumber, (5.19) becomes:

$$\omega_m = \frac{\Delta K}{\tau}\left[z + (m-1)\frac{\delta}{M} + v\frac{\tau}{2}\right] + K_c v \tag{5.23}$$

The first term determines the frequency of the photodetected signal due to the sweeping, proportional to the OPD, i.e. due to the modulation of the spectrum into a channelled shape, hence denoted as ω_{CS}:

$$\omega_{cs} = \frac{\Delta K}{\tau}\left[z + (m-1)\frac{\delta}{M} + v\frac{\tau}{2}\right] \tag{5.24}$$

As

$$v\frac{\tau}{2} = \frac{\delta}{2M} \ll \delta \text{ and } \delta \ll z \tag{25a, 25b}$$

$$\omega_{cs} \sim \frac{\Delta K}{\tau} z \tag{5.26}$$

The last term in (5.23) can be put under the form:

$$\omega_D = vK_c = 2\pi F_D \tag{5.27}$$

and represents the Doppler shift. This shows that the Doppler shift is proportional to the velocity of varying the OPD, as expected. This depends on the amplitude and frequency of the driving signal applied to the GS.

If the beam would be stationary on C, ω_{CS} would be the only frequency term and the tilt of the mirror would be correctly displayed by the B-scan. Due to lateral scanning, the frequency of the photodetected signal varies from ω_{CS} by ω_D.

5.2.2 Predicting the profile of Doppler shift variation during lateral scanning

Let us consider the signal driving the GS as triangular, of period 2T, as illustrated in the top row of the table in Fig. 5.2. Let us also consider that the target is a mirror, that in the case of (s) configuration is tilted. For the sake of illustration, an exaggerated tilt of 45 degrees was considered and the variation of optical path, δ, calculated in the table in Fig. 5.2, middle row left. In configuration (e), the mirror was considered oriented normally to the optical axis. The path variation is quadratic in this case, hence δ will vary along a parabola. δ is considered zero at the beginning of the lateral scan for both (s) and (e) configurations. In the middle of the lateral scan, for 0.5T, when the scanning beam reaches point C (Fig. 5.1) in (s) $\delta = 0.5$ while in (e) is maximum, 1 (considered as a normalised value to maximum deviation). At the end of the lateral scan, at time equal to 1, i.e. for T, in (s) deviation δ is maximum, i.e. 1 while in (e) deviation returned to zero.

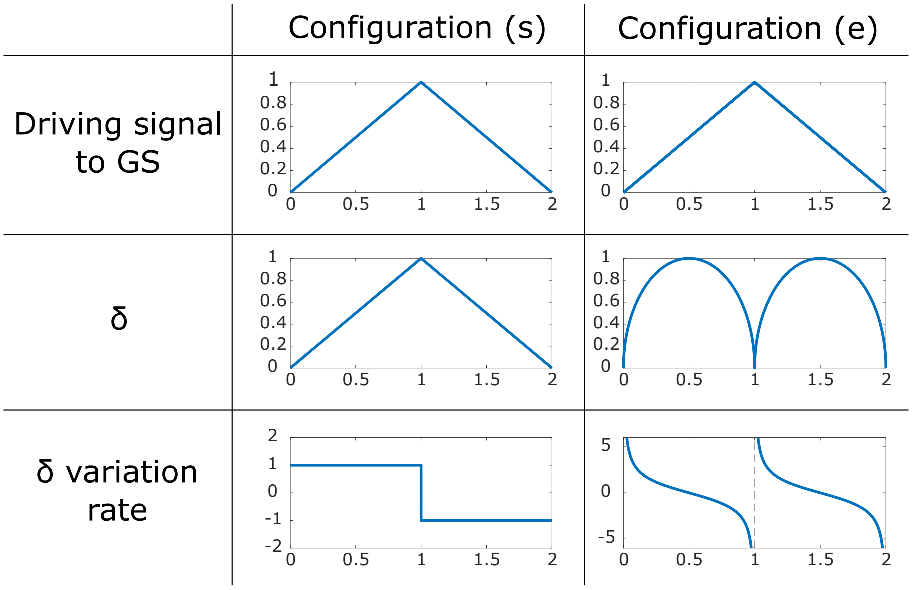

Figure 5.2: Approximate illustration of the δ and its variation rate for each configuration in Fig. 5.1 versus time during lateral scanning. Doppler frequency shifts due to variation of δ in the middle row are shown in the bottom row.

The time on the horizontal axis in all illustrative graphs in Fig. 5.2 is in units of T, where T is the half period of the triangular signal applied to the GS. What determines the Doppler shift is the variation rate of δ, illustrated in the third row. In configuration (s), the variation rate is expected to be constant, which will lead to a constant ADE across the B-scan. This ADE will change signs depending on the scanning direction. In configuration (e), due to the parabolic shape of δ, the

ADE will be larger at the edges than at the centre of the B-scan, and the sign will remain the same regardless of the scanning direction. The resulting B-scans for a mirror will be distorted, following the profile obtained by adding the contours in the middle and bottom rows in Fig. 5.2

5.3 Experimental set-up

The schematic diagram of the OCT set-up is shown in Fig. 5.3. This consists in an interferometer based on a beamsplitter, BS, and a 50/50 fibre coupler, FC, terminated on a balanced photodetector, BPD. The photodetected signal delivered by the BPD is sampled by an ATS 9350 AlazarTech card digitiser placed in a computer. A lateral 2D scanning head scans the beam over the sample via an interface optics, IO, such as shown in Fig. 5.1. The 2D scanning head is composed of two orthogonally placed galvanometer scanners, (not shown), determining the line in the raster and the frame rate. The theory presented above refers to the galvanometer scanner determining the line, labelled in continuation as GS, that is driven faster than the frame galvanometer scanner. Depending the case, the role of GS was played by one or the other galvanometer scanner in the scanning head.

To fully evaluate the conditions that lead to ADE, the GS was driven with triangular signals at different amplitudes and frequency and for most data collections here the frame galvo scanner was set at rest. The interface optics (IO) discussed in Fig. 5.1 were evaluated under the excitation of three swept sources (SS). (i) CSU-SS, a commercial slow unidirectional tuning SS, Broadsweeper BS-840-2 (Superlum) with a sweep rate of 2 kHz. The spectral emission is centred at 850 nm, starting at 872 nm and finishing the sweep at 828 nm; (ii) RSB-SS, an own assembled bidirectional SS using a resonant scanner driven at $1/(2\tau) = 16$ kHz [12], sweeping between 850.5 nm and 859.5 nm, equivalent to tuning at a frequency of 32 kHz during each half pe-

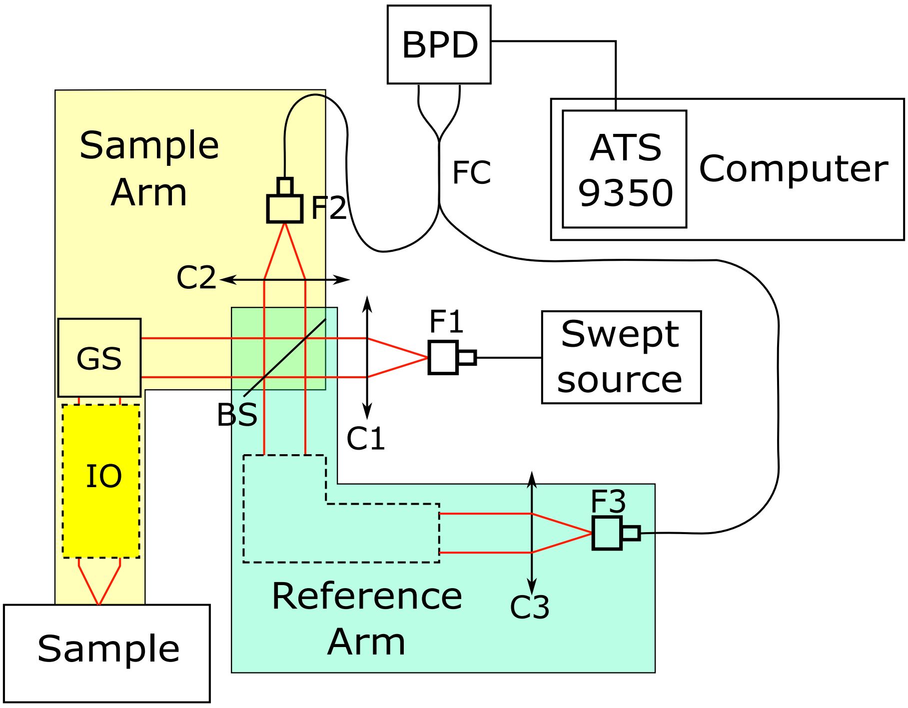

Figure 5.3: Schematic diagram of the OCT set-up employed. IO: interface optics; F1-3: fibre mounts; C1-3: collimator; BS: Beamsplitter; FC: 50/50 fibre coupler; GS: Galvanometer scanner; BPD: Balanced photodetector.

riod, τ; (iii) CFU-SS, a commercial fast unidirectional tuning SS, Axsun sweeping at 100 kHz, central wavelength 1060 nm

The CSU-SS exhibits a top hat spectrum, in which case applying (5b) for a bandwidth $\Delta\lambda = 44\,\text{nm}$, $a \sim 10\,\mu\text{m}$. The RSB-SS exhibits a Gaussian spectrum, hence using (5a) and $\Delta\lambda \simeq 9.5\,\text{nm}$ gives $a \sim 33\,\mu\text{m}$. The CFU-SS exhibits a $\Delta\lambda =$ 100 nm according to its data sheet, that should have a top hat spectrum, resulting in $a \sim$6 µm using (5b), however, its spectrum is a combination of two Gaussian peaks, resulting on a reduced axial resolution of $a \sim 9\,\mu\text{m}$. The axial resolution measured of the three SSs were respectively: $a \sim 10$, 33 and 9 µm.

The resonant scanner driver of the RSB-SS delivers a TTL trigger to synchronise external instruments, with two sweeps per trigger. This can be conveniently delayed in relation to the sinusoidal signal applied to the resonant scanner by actuating on a front panel potentiometer. Fig. 5.4 presents 3 traces. The TTL signal shown

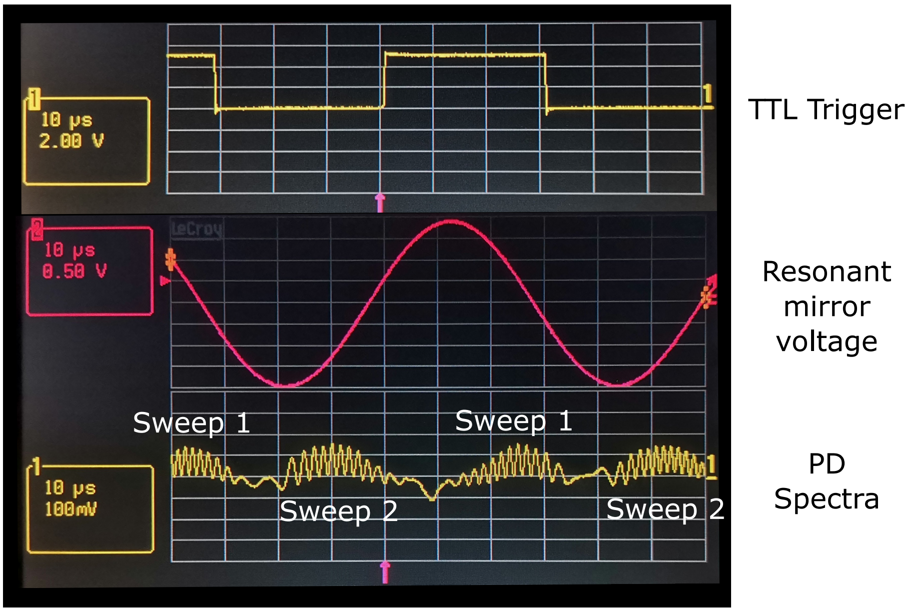

Figure 5.4: Channelled spectrum (bottom trace, yellow) versus the sinusoidal signal applied to the resonant scanner (middle trace, red) in the RSB-SS and the trigger signal (top trace, yellow).The GSs were kept at rest.

in yellow on the top trace is the trigger sent to the digitiser. In red, middle trace represents the sinusoidal signal sent to the resonant mirror used for the sweeping in the RSB-SS. The bottom trace in yellow shows the photodetector signal at the interferometer output. This presents a channelled aspect, where the larger the optical path difference in the interferometer, the denser its modulation [13].

Because electrical cables used to convey the three signals to the scope are of different lengths, the transitions on the trigger signal are slightly displaced laterally in respect to the other two waveforms in Fig. 5.4. In LabVIEW, trigger is delayed digitally in order to shift the fly-back outside of the displayed image.

One sweep falls under the 5 V part of the trigger, while the second sweep falls under the 0 V part of the trigger. The spectrum is split in half and the sweep under 5 V is denoted as "Sweep 1" whilst the sweep under 0 V is denoted as "Sweep 2". Later below these sweeps will be put in correspondence with the backwards and forward sweeping performed by the RSB-SS.

5.4 Experimental results

The estimated behaviour for δ and its variation presented in Fig. 5.2 can be confirmed by performing *en-face* TD-OCT in both configurations and observing the pattern formed in the image due to the interface optics. These patterns can be seen in Fig. 5.5. The images were obtained with the CSU-SS source emitting a narrow spectral emission (non sweeping) and driving both galvanometer scanners, obtaining a 2D *en-face* time domain OCT image. In configuration (s), a regular pattern of parallel lines are obtained [5]. The tilt of lines is due to the mirror surface being inclined in respect to both X and Y axes. In configuration (e), Newton rings [6] appear, where the distance between adjacent rings decreases for rings further away from the centre. Some artefacts can be observed at the edges of both images. In the case of configuration (s), these artefacts are due to the acceleration of the galvo scanners, while in the configuration (e), the artefacts are due to aliasing effects.

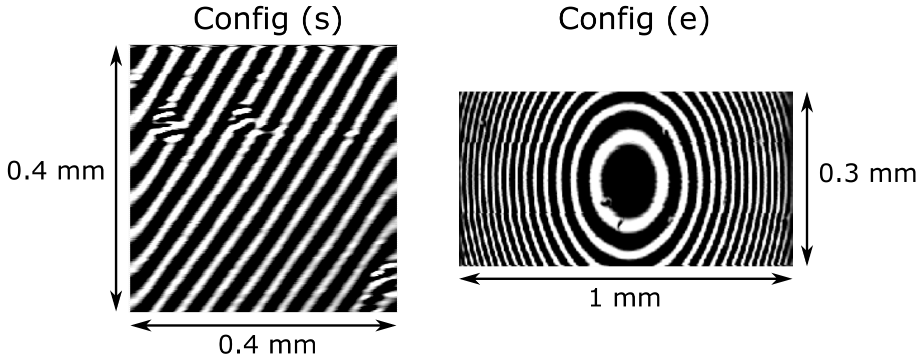

Figure 5.5: *En-face* TD-OCT image obtained from a flat mirror using configurations (s) and (e). In the configuration (s) the size scanned horizontally is similar to that scanned vertically, of 0.4 mm, corresponding to an amplitude of 0.1 V applied to both galvanometer scanners. The frequency of the triangle signal applied to the galvanometer scanner (line) for scanning horizontally was 500 Hz (T = 1 ms) while the frequency of the signal driving the galvanometer scanner for scanning vertically (frame) was set to 1 Hz (i.e. leading to a C-scan made from 500 T-scans). In the configuration (e), the voltages applied to the two galvanometer scanners were1 V and 0.2 V respectively, and the image was cropped to show the central rings. The frequency of the triangle signal driving the line galvanometer scanner was 80 Hz (T = 6.25 ms) and that of the signal driving the frame galvanometer scanner was 0.4 Hz.

5.4.1 Configuration (s)

SS-OCT where the swept source performs unidirectional sweeping

In order to evaluate the distortions affecting the B-scan OCT images based on the SS-OCT method, three different measurements in each configuration are performed using the CSU-SS: the first measurement consists of a 1D TD-OCT image obtained by driving the line galvanometer scanner only, in contrast to the 2D TD-OCT image from Fig. 5.5, in order to isolate the distortions in a single scanning axis only; the second measurement is obtained from an electrical Spectrum Analyser that measures the RF spectrum of the photodetected signal; the third measurement consists of a B-scan obtained with the full tuning bandwidth of the CSU-SS. In the first two measurements, the line galvanometer scanner, playing the role of GS in Fig. 5.1, was driven at the same rate of 80 Hz, while in the 3rd set at both 80 Hz and 160 Hz as detailed further below. These results are presented in Fig. 5.6 for the configuration (s) and later on, in Fig. 5.9 for configuration (e).

From the TD-OCT image presented in Fig. 5.6, a prediction of the ADE value expected in SS-OCT can be made. With a slit size of 1 mm, which is a 43 % of the image size, the number of fringes is reduced by a factor of 0.43. 27 fringes are seen in the image in Fig. 5.6 top left. This means that within a lateral scan, there are ~ 63 fringes. The number of fringes corresponds to a path variation $\delta = 63\lambda/2 = 27\,\mu\text{m}$. For $2T = 1/80\,\text{Hz}$, this leads to a speed of z variation of $v = \delta/T = 4.3\,\text{mm/s}$. Then a Doppler shift $= F = 2v/\lambda \sim 10\,\text{kHz}$ can be evaluated. As this is larger than the sweeping frequency of 2 kHz, an ADE is expected according to (5.8).

Indeed, the spectrum analyser in Fig. 5.6 right shows the main component at 10 kHz. In the SS-OCT B-scan image in Fig. 5.6 bottom left, a peak to peak depth variation of 20 kHz is measured. This is because each ramp of the GS leads to ADEs of opposite signs, so the frequency shift corresponding to ADE during each GS ramp

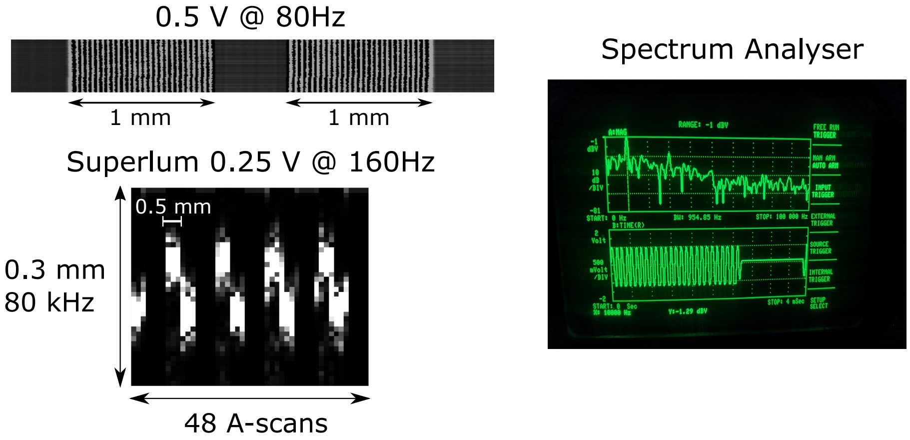

Figure 5.6: Three procedures to evaluate the ADE in configuration (s) using the CSU-SS. Only the line galvanometer scanner, playing the role of GS in Fig. 5.1, is driven, while the other galvanometer scanner is at rest. Top left: TD *en-face* fringe pattern from a mirror behind a 1 mm slit with CSU-SS non sweeping; Right: frequency spectrum at the top and temporal evolution at the bottom of the photodetected signal in TD *en-face* OCT with non sweeping CSU-SS (the spectrum analyser display corresponds to both cases of either 0.5 V at 80 Hz or 0.25 V at 160 Hz); Bottom left: cross section (B-scan) image obtained by sweeping the CSU-SS.

is 10 kHz. The agreement of the two ADE values obtained by using either procedure in Fig. 5.6 suggests that in practice either TD or SS-OCT method can be used to evaluate the number of fringes per lateral scan, and consequently, the correct adjustment of the interface optics (tilt of mirror and hence δ).

For each increase of OPD by an axial resolution interval ($a = 10\,\mu$m), according to eq. (5b), the frequency of the read signal increases by the sweeping frequency, i.e. by 2 kHz. Therefore, for any of the 3 methods above, the ADE can be ignored if the Doppler shift is less than the frequency pixel of 2 kHz. This determines a maximum speed of $(\lambda/2)\cdot 2$ kHz $= 0.85$ mm/s, when speed exceeds this values, then distortion takes place. For the case in Fig. 5.6, speed is 4.3 mm/s, i.e. larger, so an ADE is expected. Obviously, a Doppler shift of 10 kHz exceeds by a factor of 5 the frequency pixel of 2 kHz. This factor is similar to that obtained by the ratio of the current speed of 4.3 mm/s over the maximum speed value evaluated above of 0.85 mm/s.

SS-OCT where the swept source performs bidirectional sweeping

Swapping the CSU-SS with the RSB-SS presents a new effect, as portrayed in Fig. 5.7 (a). Since the RSB-SS performs bidirectional sweeping, as presented in Fig. 5.4, to generate a B-scan, the A-scans due to each sweep need to be intercalated. Therefore, if the A-scans from Sweep 1 are labelled as S11, S12, S13,... S1n and the A-scans from Sweep 2 are named as S21, S22, S23,... S2n, a B-scan obtained with the RSB-SS will be composed of A-scans S11, S21, S12, S22,... S1n, S2n.

Whilst previously with the CSU-SS the ADE was constant over the half period of lateral scanning T, now in Fig. 5.7 (a), with the RSB-SS, the ADE changes sign between each A-scan, causing breaks in the B-scan. If the A-scans are separated according to their sweeping direction, as shown in Fig. 5.7 (b), the Sweep 1 experiences an opposite ADE in respect to the ADE of Sweep 2.

When obtaining data from the RSB-SS, we recorded every other trigger and used the time of the second trigger to split and construct the A-scans. This means that for each pair of sweeps, that were obtained, sweep 1 and sweep 2 (as labelled in Fig. 5.4), the next pair was not recorded. This means that for example, if the recording time is set to 1 ms, given $2\tau = 1/(16\,\text{kHz})$, we retain and record 8 pairs of A-scans, instead of 16.

To obtain Fig. 5.7, only the line galvanometer scanner, GS, is driven. A triangular signal was applied to GS of 1 V amplitude and $1/(2T) = 666\,\text{Hz}$, scanning laterally $\sim 4\,\text{mm}$ of a flat mirror as a sample for each half period $T = 0.75\,\text{ms}$. For the B-scan display, both ramps are recorded 4 times, obtaining a total of 8 B-scans in 6 ms. During each period 2T of the GS signal, there are M = 12 A-scans, summing up to 48 A-scans for each sweeping direction. Due to bidirectional sweeping of the RSB-SS, there are 96 A-scans in the display of the 8 B-scans. Considering the size of the B-scan along axis Z of 960 µm, the top of the B-scans corresponding to the two sweep direction are axially shifted in respect to each other by 192 kHz.

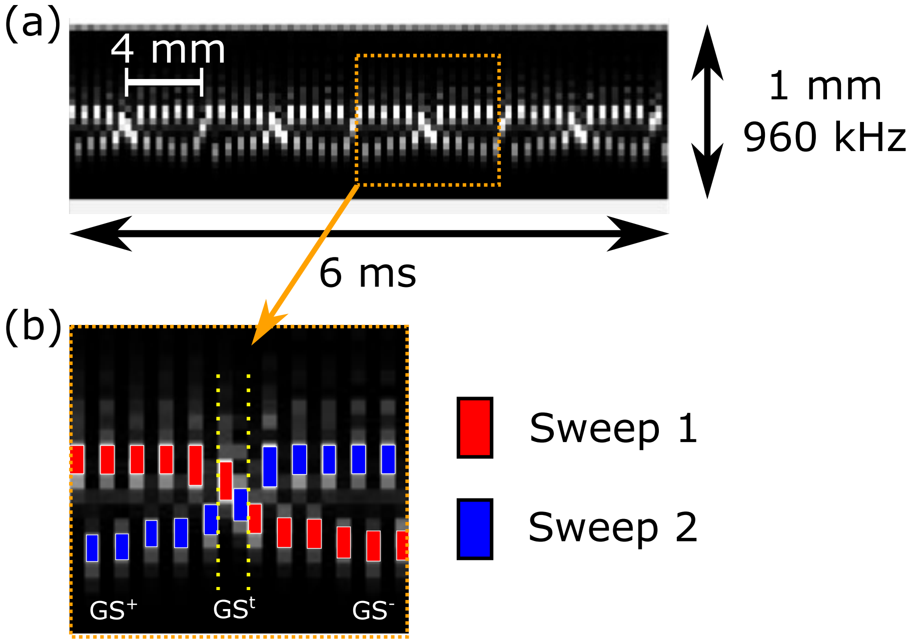

Figure 5.7: B-scans from a mirror obtained using SS-OCT employing the RSB-SS: (a) The image contains 4 full periods of the GS driven at 666.67 Hz and 1 V amplitude, creating a total of 8 B-scans per image of 4 mm lateral size of the mirror (extending for 6 ms). Vertical axis represents 960 kHz (∼ 1 mm). (b): a zoomed section of the third period is presented. The A-scans corresponding to Sweep 1 are shown in red, while the A-scans from Sweep 2 are shown in blue. The positive slope of the GS is marked as GS^+, its negative slope as GS^-, and the transition between both slopes is marked as GS^t. In the mid of the transition, the speed of the GS approaches 0 and the ADE disappears. As the GS accelerates, the ADE increases again.

This corresponds to an ADE for each sweep of 96 kHz, i.e. of ~ 3 axial frequency pixels (determined by the resonant scanner half period of 1/32 kHz). Clearly, such high ADE level prevents generating a correct B-scan, with a single, contiguous well defined image contour.

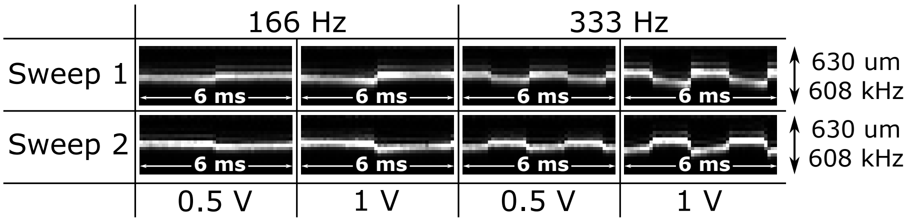

Figure 5.8: Comparison of B-scans obtained using SS-OCT employing the RSB-SS, for two values of voltage and frequency of the signal applied to the GS. The vertical size in all B-scans is 630 µm along the axial coordinate Z, corresponding in frequency to 608 kHz.

To understand the nature of the ADE, several experiments were performed by changing the different parameters at which the GS is moved, with B-scans obtained as shown in Fig. 5.8, and measuring the axial separation between consecutive B-scans, each obtained from a different slope of the GS. First, the GS was run at 166 Hz where a small variation on OPD was noticed, giving an error in axial positioning between contours of 32 kHz (33 µm) in the first column. When doubling the amplitude of the driving signal from 0.5 V to 1 V, the amplitude of the ADE doubled. Then by doubling the frequency to 333 Hz while reducing to 0.5 V amplitude the same ADE value was obtained.

A slip between contours value of 64 kHz (66 µm), corresponding to an ADE of 32 kHz (33 µm), at 166 Hz and 1 V is similar to that obtained for 166 Hz and 0.5 V, presented in both the 2nd and 3rd column respectively. This implies that the ADE is directly proportional to the angular speed of the GS, that can be modified either by frequency or amplitude of the signal applied. Obviously such a behaviour can be attributed to the Doppler shift coming from the lateral scanning imprinted by the GS in the system, which depends on both the amplitude and frequency of the lateral scanning when the target is a tilted mirror. In the last column, with a frequency of 333 Hz and an amplitude of 1 V, the distance between contours is $\sim$ 128 kHz (132 µm).

In the 1st column in Fig. 5.8, the ADE is almost equal to half of the axial resolution interval of $a = 33\,\mu\text{m}$. For each advance in z by a, the electrical signal spectrum advances by a frequency pixel interval of $1/\tau = 32\,\text{kHz}$. In the 2nd an 3rd column, the distance between contours is $\sim$ 2 frequency pixels = 2 axial resolution pixels, $2a$, while in the 4th column it is $\sim 4a$. This correlates with an ADE for each ramp of the GS of $1a$ and $2a$ respectively. The acquisition time for each B-scan is 6 ms. The 166 Hz group covers the full period 2T of the driving signal, while the 333 Hz group covers two periods, i.e. 4T. Each image is comprised of 48 A-scans, having 24 A-scans per half period T when $1/(2T) = 166\,\text{Hz}$ and 12 A-scans per half period T at 333 Hz. At 0.5 V, the scanned lateral size over the mirror was 2 mm, while at 1 V it was 4 mm, as in Fig. 5.6.

The larger the velocity of lateral scanning, the larger the frequency deviation of the frequency spectrum read by the photodetector during a sweeping time interval, τ. In the case of the interface optics in Fig. 5.1 (s), a tilt of the mirror leads to a Doppler shift that is constant during each lateral deflecting interval T. Obviously, during the next deflecting interval T, the direction of OPD variation changes, meaning that the frequency spectrum of the electrical signal (read at the photodetector output by sweeping through the spectrum) will suffer deviations in opposite directions during the two lateral scanning intervals T given by half period of lateral scanning, of period 2T, as illustrated in Fig. 5.4. The shapes of B-scans in Fig. 5.6, 5.7 and 5.8 are in line with the expectations predicted by the bottom row in Fig. 5.2 left.

5.4.2 Configuration (e)

SS-OCT where the swept source performs unidirectional sweeping

In the examples above, the velocity in OPD variation is constant during the lateral scanning half period, T. This is also proven by the uniform separation of the fringes in the TD OCT image in Fig. 5.6.

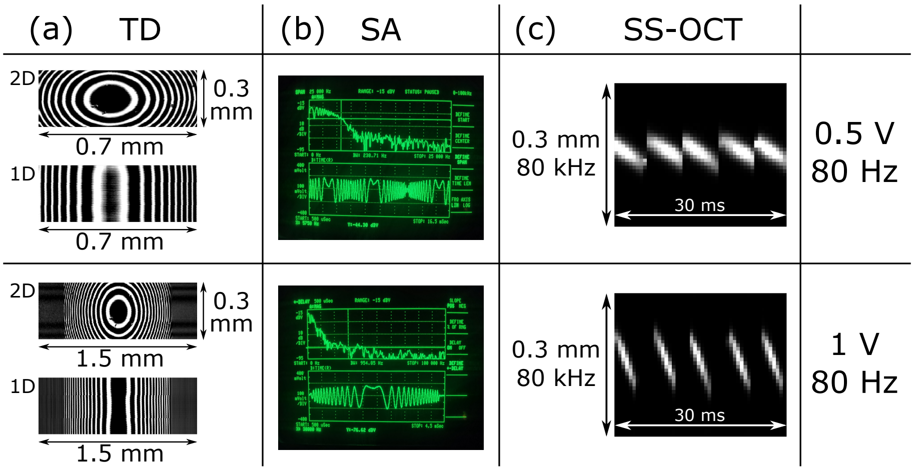

Figure 5.9: Three procedures to evaluate the ADE in configuration (e) using the CSU-SS. (a): 2D and 1D TD *en-face* fringe pattern from a mirror behind a 1 mm slit with CSU-SS non sweeping, top with both galvanometer scanners driven, bottom using the line galvanometer scanner only, acting as GS from Fig. 5.1; (b): frequency spectrum at the top and temporal evolution at the bottom of the photodetected signal in TD *en-face* OCT with CSU-SS non sweeping; (c): cross section (B-scan) images using SS-OCT. First row corresponds to driving the GS at 80 Hz with 0.5 V amplitude, while in the second row the GS was driven at 80 Hz with 1 V amplitude.

For the case of imaging the eye, as shown in Fig. 5.2(e) , the velocity varies non-linearly, as presented in [6]. As the OPD varies via a square law in relation to the angle of scanning [6, 14], during each lateral scanning interval T, the velocity is either positive or negative, going through zero on axis (if the incident beam is exactly on the GS pivot).

As in Fig. 5.6 for configuration (s), we started by comparing TD-OCT, B-scans and the electrical spectrum analyser signal. These results are presented in Fig. 5.9. The source employed for all the sets was the CSU-SS. This time, since we expect the ADE to not be constant (according to Fig. 5.2 right bottom), we also compared results for two different GS speed rates. First row corresponds to 0.5 V amplitude and 80 Hz frequency, same as in Fig. 5.6, and the second row corresponds to doubling the lateral scanning speed by applying double of amplitude, 1 V at 80 Hz. The mirror object scanned was set behind a slit of 1 mm width as in Fig. 5.6.

This time, both TD-OCT and the spectrum analyser procedure display a chirp in periodicity. This makes the exact calculation of ADE dependent on the position of the pixel in the T-scan. The B-scans in the 3rd column in Fig. 5.9 show a tilt in agreement with the predictions in Fig. 5.2 bottom row right.

To study the relationship between the tilt of contours in Fig. 5.9 (c) column, and the speed of the scanner, we repeated similar measurements as performed for the configuration in Fig. 5.1 (s).

Using the CSU-SS, we obtained Fig. 5.10, in which 2.5 periods of the driving signal are shown, i.e. 2.5 B-scans. Within each half period, for small voltages, the profile in Fig. 5.2 bottom left is visible, similar to that in configuration (s), i.e. from one half period to next, the T-scans jumps axially. This may be due to a small tilt of the mirror, in which case, when the amplitude is small, all lateral scan is within one side of point C in Fig. 5.1. At larger amplitudes, the lateral scan crosses the other side of point C and the offset is less visible.

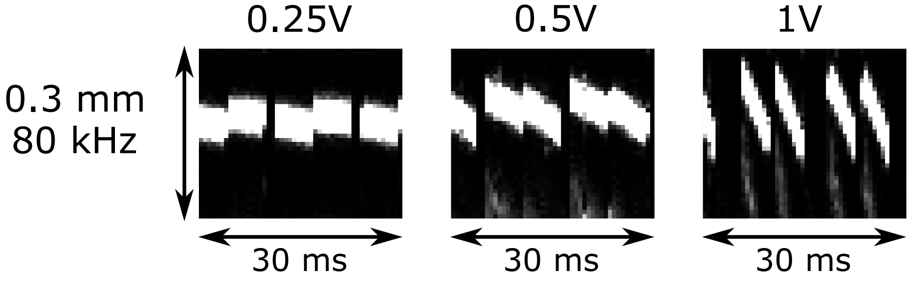

Figure 5.10: Comparison of B-scans of a flat mirror covered with a slit using the CSU-SS in configuration (e). The frequency of the signal used for lateral scanning was kept constant at 80 Hz, while the amplitude of scanning was increased in double steps.

Number M of A-scans in each half period T = 6.25 ms is M = 2 kHz/160 Hz = 12 A-scans. At 0.25 V, when M is larger than 12, ADE can be ignored. Otherwise, more than M = 48 A-scans are needed at 1 V to ignore the ADE, requiring a reduction of the lateral scan rate to less than 20 Hz.

SS-OCT where the swept source performs bidirectional sweeping

Using the RSB-SS, Fig. 5.11, is obtained, where the tilts of the T-scans are shown. The higher the voltage, and the higher the scanning frequency of the triangular signal applied to GS, the larger the tilt. The contours displayed are, to some extent, similar in shape with the profiles predicted in the right sketch of the bottom row in Fig. 5.2. As they extend over a few pixels in depth only, they cannot follow the exact shape predicted. However, for each half period T, the tilt is evident. At 160 Hz frequency (corresponding on each ramp to 320 Hz) and 1 V amplitude, the ADE is 250 µm, $\sim$ 240 kHz. A conversion C = 1.04 µm/kHz relates the frequency deviation to the ADE. In the RF spectrum of the photodetected signal, pixels are separated by $1/\tau = 32$ kHz and along depth by 33.28 µm. A variation in frequency of 240 kHz means an ADE of 240/32 = 7.5 axial resolution pixels, of size a each, along the depth coordinate, z.

In Fig. 5.11 (a), there are M = 16/0.32 = 50 A-scans per each ramp in either sweeping direction. ADE is barely perceptible. This means that for M > 50, the error can be ignored. However if the amplitude of scanning is increased, as shown in (b), the number of A-scans, M, should be increased accordingly (for instance by at least doubling the sweeping speed, if that would be possible) in order to maintain the ADE below the axial resolution interval, a, where it could be ignored. In order to compare the tilts experienced with both sources, Fig. 5.12 presents tilts of T-scans in the B-scans obtained for a GS driving signal of different scanning frequency with the RSB-SS (a) and the CSU-SS (b) against the T-scan obtained with the sample

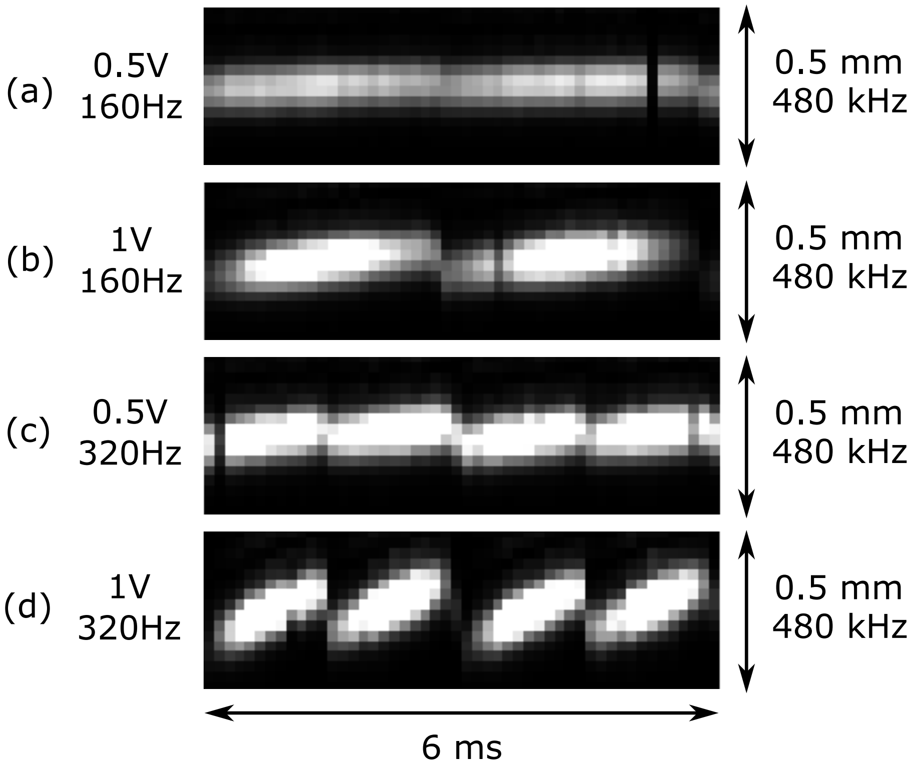

Figure 5.11: Comparison of B-scans obtained with the RSB-SS in the configuration (e), only the B-scans from the blue to red (forward) sweep are being presented for different settings of the signal driving the line galvanometer scanner only, considered as GS in Fig. 5.1. By doubling the frequency of the signal applied to the GS but halving the amplitude, the speed of the galvanometer scanner remains the same, which in theory should lead to the same ADE value. In (a) and (b), the full period of the driving signal is shown, while in (c) and (d), twice that period.

beam stationary. The larger the scanning speed, the larger the tilt.

The data corresponding to the CSU-SS are obtained from Fig. 5.10 while the data obtained with the RSB-SS are obtained from Fig. 5.11. Each colour represents a linear fit of a single B-scan from each of the settings used for each figure. The base angle deviation of the GS mirror was measured by applying offsets of $-0.5\,\mathrm{V}$, $0\,\mathrm{V}$ and $0.5\,\mathrm{V}$, to its driver. Finally, the base angle was subtracted from the fits to measure strictly the deviation produced by the ADE,leaving the base line constant at 0 (presented in solid black-line in both figures).

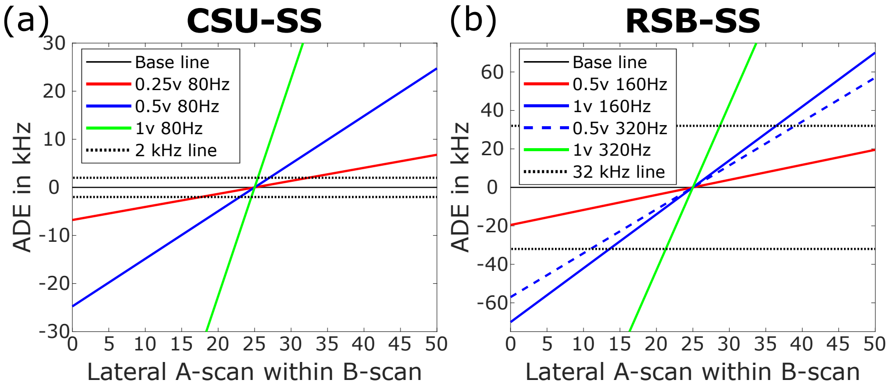

Figure 5.12: Tilt of T-scans in the B-scans obtained for different frequency of the signal applied to the GS with the CSU-SS (a) and RSB-SS (b) against the T-scan obtained with the sample beam stationary (base line) calculated in configuration (e). The vertical axis corresponds to the ADE in kHz while the horizontal axis corresponds to the lateral position in the B-scan. The insets show the settings used for the GS driving signal. The horizontal dotted lines correspond to the frequency resolution of the spectrum sampling, as determined by the sweeping frequency of each source, 32 kHz for the RSB-SS and 2 kHz for the CSU-SS. Any value between these dotted lines in each graph would not be lead into visible ADEs in the B-scans.

These curves are specific for the sweeping rates of the two swept sources employed. By increasing the swept source rate, the interval between the two dashed lines in both figures increases, and correspondingly, the number M of A-scans as a manifestation of better accomplishment of inequality (5.9).

5.5 Prediction of the sweep direction

As seen in previous figures, the Doppler shift adds to or reduces the frequency of the photodetected signal due to the two sweeps, sweep 1 and sweep 2 as labelled in Fig. 5.4. The ADEs in the two sweeps are of opposite signs. The ADE also changes sign based on the slope of the ramp of the signal applied to the GS, with one ramp experiencing a reduction of the observed OPD and the other an increase. For ease of calculations, the analysis in this section is restricted to the configuration (s), where a constant ADE is present during each half period T.

When the spectral filter in the swept source uses a resonant scanner (RS), the instantaneous sweeping direction during each half period, τ, of the signal applied to the RS, in term of lowering or increasing the wavelength generated, cannot be easily determined, as any optical spectrum analyser produces a spectrum for an average of sweeps. The RS cannot be tuned to lower frequency rates in order to enable the use of an optical spectrum analyser. Synchronising an optical spectrum analyser at 16 kHz would be difficult. It is demonstrated here that by using a galvanometer scanner in the OCT interface optics and a tilted mirror as an object, by measuring the resulting ADE, the sweeping direction of a swept source can be determined. Differences in the B-scans due to sweeping direction are evident, but from these images the sweeping direction nor the direction of deflection can be estimated. As the combination of f (due to sweeping) with F (Doppler shift) depends on both signs of the lateral scanning and of the sweeping, a simple procedure was developed to identify the direction of lateral scanning in the images produced. To this goal, the measurements described below are presented.

As illustrated in Fig. 5.13 (a), first, one of the edges of the scanned area of the sampled mirror is covered partially using an opaque screen, OS, in order to differentiate between each ramp of the galvo scanner driven, from now on, considered as GS in Fig. 5.1. If the right side of the object imaged, when the GS scans from left to right is covered, then the part of the image end of the ramp will be black. When the GS scans from right to left, the beginning of the ramp will be missing in the image. In this way some relation can be established between time and lateral position. The swap of scanning direction from left-right to right-left will not be seen, but the transition from right – left to left – right will remain visible, therefore named Visible Transition, VT.

This procedure allows us to quickly determine in a set of consecutive B-scans which B-scan corresponds to which ramp of the triangular driving signal, by simply looking at the transition between B-scans and the location of the black sectors in the images so produced.

In Fig. 5.13, the effect on the B-scans obtained using the RSB-SS is documented. In (b), a photo of the set-up is shown while in (c,d), the B-scans without the opaque screen are (c) while (d) are the B-scans with the opaque screen in place. The VT changes shape between Sweep 1 and Sweep 2, consequence of a different ADE sign for each sweep as shown.

The 4 consecutive B-scans presented in Fig. 5.13 were obtained at 333 Hz (i.e. 2T = 3 ms). On the top row there are B-scans obtained with sweep 1, while on the bottom there are B-scans obtained with sweep 2. During the VT, those in sweep 1 follow a pattern “down-up” while the others in sweep 2 follow a pattern “up-down”.

In order to determine the sign of the ADE based on the sweeping direction, the RSB-SS was replaced with the CSU-SS, for which the direction of sweeping is known, and the measurements covering the mirror were repeated as performed in the process of obtaining Fig. 5.13. The Superlum Broadsweeper 840 sweeps from red to blue (backwards), starting at 873 nm and finishing the sweep at 828 nm, at a maximum 2 kHz sweeping rate.

The GS was run with a triangular ramp of 2T = 3 ms. Since the CSU-SS sweeps

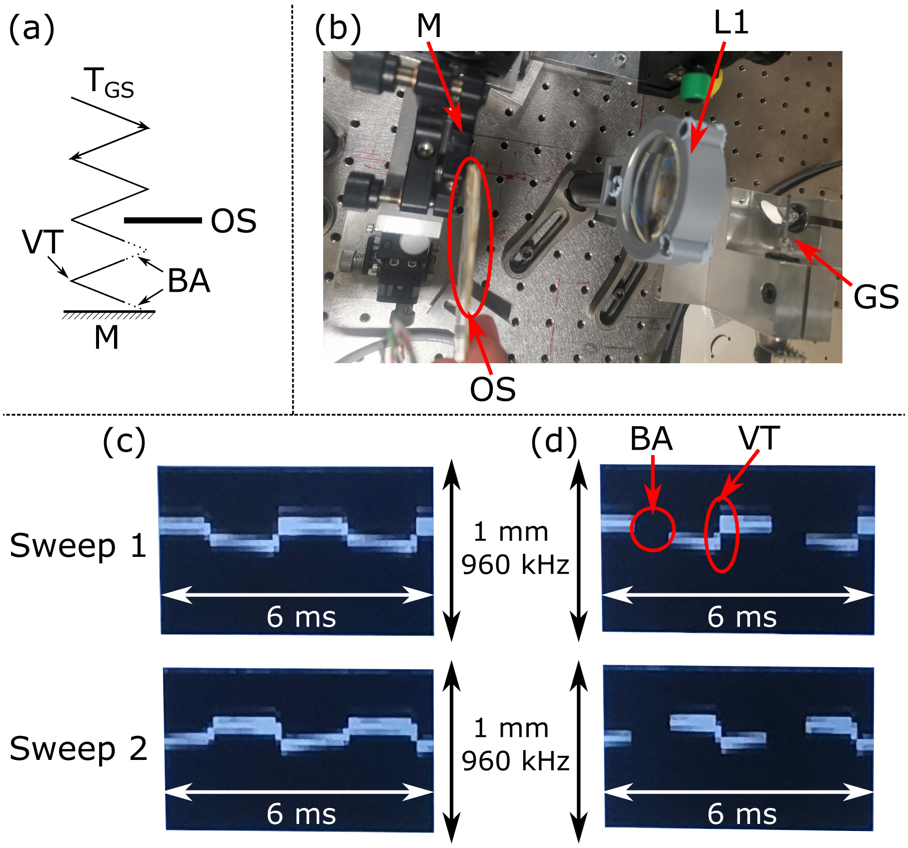

Figure 5.13: Procedure to determine the sweep direction. (a) Schematic representation of time associated to a lateral portion of the T-scan in the B-scan. T_{GS}: trajectory of laterally scanned beam by GS in time; An opaque screen (OS) blocks partially the scanned area; BA: black area in the image due to the OS; VT: visible transition. (b) Aerial view of the interface optics showing the galvanometer scanner head (with the frame scanner axis horizontal and fixed and the line scanner vertical, used as GS in Fig. 5.1, determining horizontal deflections), the lens L1, the mirror M and the OS covering one of the edges of the scanned area; (c) B-scans separated for the two sweeps of the RSB-SS; (d) The same images on the left but displaying the effect of the OS, obscuring the area marked as BA and leaving only a portion of the object as the visible transition, VT, in the B-scan image between the deflection from right to left and deflection from left to right.

at a slower rate of $\sim 1.8\,\text{kHz}$, instead of the 32 kHz for the RSB-SS, images are generated by compounding up to 20 consecutive B-scans in Fig. 5.14, to enhance both "down-up" and "up-down" transitions. Each B-scan is composed from a number of A-scans that is obtained by: $\text{M} = 1.8\,\text{kHz}/0.66 = 2.7$ A-scans per each half period $\text{T} = 1.5\,\text{ms}$.

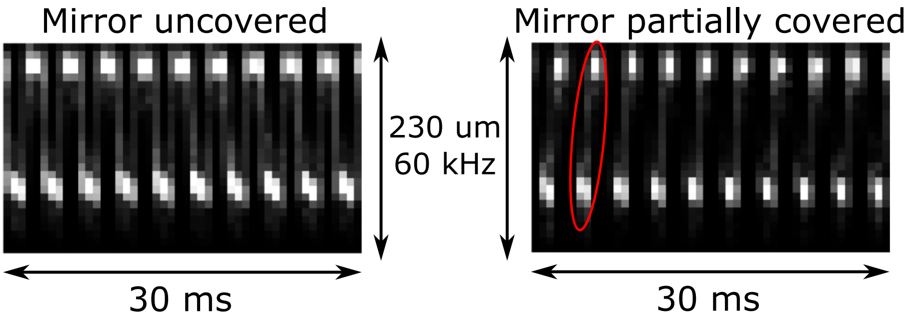

Figure 5.14: Results obtained from 20 consecutive B-scans with the CSU-SS at 333 Hz and 0.2 V amplitude. When partially covering the mirror as shown in Fig. 5.13, CSU-SS replicates the pattern "down-up" marked in red. The measured ADE peak-peak is 32 kHz.

Since the set-up can only record full A-scans, 2.7 means that sometimes we will record 2 A-scans per B-scan and sometimes 3, hence we collected 20 B-scans. A video is recorded from which 9 frames of 20 B-scans each are acquired, and averages were produced with them. Otherwise, transitions are not visible in the compounded images due to the slow acquisition speed.

The results are presented in Fig. 5.14. The B-scans present a peak to peak ADE interval of 122 µm or 32 kHz, i.e. 16 kHz per each sweeping direction. On the left, there are B-scans obtained with the mirror uncovered, and on the right there are B-scans obtained by blocking the right side of the mirror under imaging, same side as in Fig. 5.13. The transition shown within the window VT, after blocking the mirror with the opaque screen as illustrated in Fig. 5.13 top is "Down-Up", the same transition as we observed in the sweep 1 in Fig. 5.13 when using the RSB-SS. We can then infer that on the RSB-SS, the sweep 1 in Fig. 5.13 corresponds to a sweep from red to blue (backward), while the sweep 2 corresponds to blue to red (forward). This represents an interesting application of the current study, an optical spectral characterisation made possible by employing an interferometer, a deflector and an opaque screen.

It can be noticed that the ADE is larger on the CSU-SS, which runs at $\sim$ 2 kHz, than for the RSB-SS, running at 32 kHz, but this is expected, as the ratio 2 kHz/666 Hz is 16 times smaller than 32 kHz/666 Hz, in agreement with Eq. (5.6).

5.6 ADE validation using a fast swept source

While sources at 850 nm are more limited on their speed, higher sweeping frequencies are achieved at longer wavelengths [15, 16]. A valid question would be if ADE is also relevant for swept sources widely used by the OCT community at 1060 and 1300 nm, sweeping at over 100 kHz. Unfortunately, we did not have any bidirectional swept source to perform the study apart from the swept source own assembled at 32 kHz used above, at 850 nm. Hence, in this section we do not intend to reproduce all the steps presented above at 850 nm, but to prove only that axial distortion of B-scan contours still occur at faster sweeping rates.

We acquired data in a set-up similar to that of Fig. 5.3, designed for imaging the eye and paired with a commercial fast unidirectional swept source (CFU-SS) from Axsun at 1060 nm sweeping at a 100 kHz sweeping rate. A rigorous study with quantitation of tilt using a broadband source as in previous sections was not possible and therefore simply placing the mirror as a target could not guarantee an exact (s) or (e) configurations due to the large spherical aberrations of the interface optics in such a system. The line (fast) galvanometer scanner, playing the role of GS in Fig. 5.1 of the set-up was driven with a triangular signal at different frequencies, ranging from 100 Hz to 1 kHz. The results are presented in Fig. 5.15, and were obtained by scanning 2 V amplitude across a slightly tilted mirror from which only 1 mm was

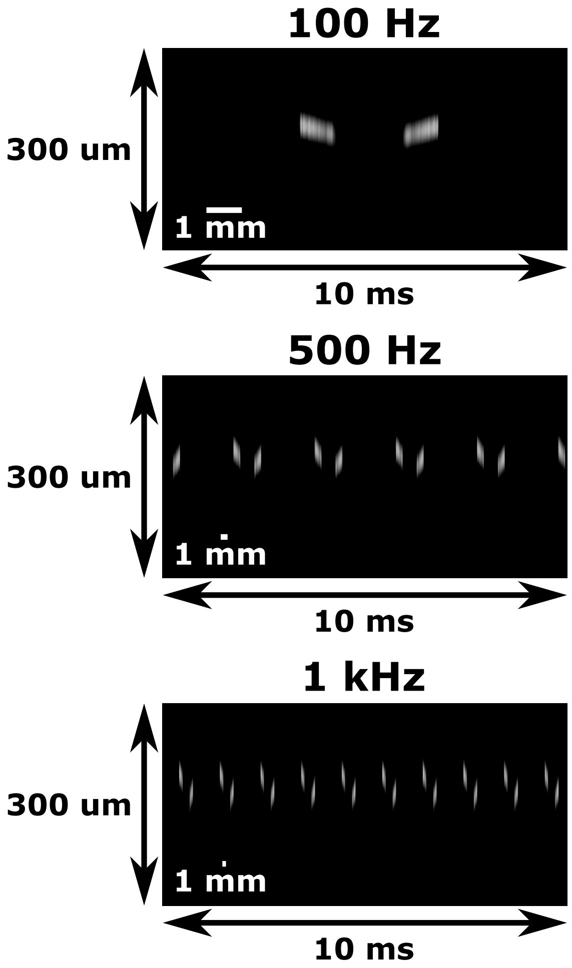

Figure 5.15: B-scans obtained from a 1 mm section of a slightly tilted mirror with the CFU-SS Axsun source operating at 1060 nm and 100 kHz sweeping rate. All images are obtained in 10 ms and span 300 µm in depth. From top to bottom, different lateral scanning frequencies, $1/2T$ are presented, with first at 100 Hz, second 500 Hz and third 1 kHz.

exposed by placing a slit in front of the mirror to minimise the effect of the large aperture, creating an approximation of the configuration (s), and presenting pairs of consecutive B-scans corresponding to each slope of the GS. The B-scans in Fig. 5.15 show a tilt of 80 µm of the mirror measured from one edge to the other of its lateral size.

At 100 Hz no ADE is perceptible, the B-scan image for the other side of the ramp of the triangular signal shows the top of the B-scan at a similar axial position. However, by increasing the lateral scanning frequency, the two contours slips in relation to each other as shown for 500 Hz and 1 kHz. The deviation of contours became apparent at 200 Hz, with minimal deviation, and at 500 Hz where the deviation is better visible. The distance between the two contours corresponding to the two ramps is $\sim 13\,\mu\text{m}$, which implies an ADE of $\sim 6.5\,\mu\text{m}$ in each B-scan. The ADE approximately doubles up to $\sim 13\,\mu\text{m}$ when doubling the frequency to 1 kHz, leading to a total deviation of $\sim 26\,\mu\text{m}$, that represents $\sim 2.9a$, considering the axial resolution $a \sim 9\,\mu\text{m}$. At the top, where no ADE is visible, M = 500, while at the bottom, with M = 50 only, where ADE is clearly manifest.

5.7 Conclusions

The chapter presents a distorting effect of contours in the B-scan OCT images that happens in SS-OCT when the number of sweeps per lateral scanning interval is small and specular layers are tilted in respect to the wavefront established by the scanning beam. Two swept sources at 850 nm were evaluated, one unidirectional at 2 kHz (CSU-SS), the other bidirectional at 32 kHz (RSB-SS), in two configurations, as used for imaging skin or imaging the retina. A third unidirectional fast source at 1060 nm (CFU-SS) at 100 kHz was used in a skin configuration to prove that the ADE may present a problem even when using fast swept sources. With continuous progress in the technology of swept sources, more bidirectional sources will be reported, in which case the error documented here doubles in comparison to that for unidirectional sweeping.

The distortion manifests in displacement of structure in the B-scan along its depth, due to the Doppler shift imprinted by lateral scanning. For each lateral pixel, its depth position is altered axially by an ADE. As long as ADE is less than the axial resolution interval, a, such error is not visible. As a rule of thumb, the ADE affects all systems depending on the threshold of path difference δ due to tilt, established by equation (5.9): when δ/M exceeds $\lambda/2$, where M is the number of lateral pixels, given by the ratio T/τ. The ADE is observable at slow as well as at fast sweeping rates, and the deciding factor is not the sweeping speed, $1/\tau$ but the ratio M. For instance, for the three systems used: in Fig. 5.6, at 2 kHz, M $\sim$ 13, in Fig. 5.8, using the 32 kHz bidirectional, M $\simeq$ 48 at 333 Hz, and using the fast source at 100 kHz, in Fig. 5.15, M = 500, 100 and 50 in the three cases shown, depending on the lateral scanning frequency.

So irrespective of sweeping speed, ADE becomes insignificant if larger M values are used. In general, the OCT community employs large number M of pixels and perhaps this is why such an effect has not been documented so far. There is some fundamental value in equation (5.9), that OCT developers should be aware of, as the number of half wavelengths exceeded by δ/M is equivalent to the number of axial resolution intervals in the ADE.

The authors are unaware of prior reports documenting such axial errors of contours of specular tilted targets described here, depending on the direction of the lateral scanning, direction of sweeping and object layer tilt.

The ADE demonstrated here have been kept at minimum values by proper adjustment of the interface optics and with due attention given to the beam incident on the two galvanometer scanner, each to be placed on the rotation axis of the respective galvo scanner. However larger deviations were observed for improper adjustment of the interface optics which were not included here. The variations in OPD during scanning can be exacerbated by incorrect lateral adjustment of lens position L1 in Fig. 5.1 (s) or of the telescope of lenses L1 and L2 in Fig. 5.1 (e). As noticed in the TD-OCT practice, more fringe cycles are created in the C-scan time display in Fig. 5.5 if the incidence of the beam is moved away from the pivot of the GS, or the mirror used as a sample is tilted. Only the simplest cases of a tilted mirror in the (s) configuration and of a horizontally flattened contour of the retina in the (e) configuration have been considered. In practice however, equivalent path deviations, as δ here can be created by off axis placement of lenses or incidence beam not exactly on the rotation pivot of either galvanometer scanner, with the most attention needed to the line scanner, that is driven faster. Therefore it is expected that ADE to be larger than that estimated by the equation (5.9) due to improper adjustment of lateral scanners and interface optics. Similar studies as presented here for the two simplified cases of (s) and (e) in Fig. 5.1 can be performed by writing explicit dependence of optical path versus deviation angle.

Driven by the need for quantitate the ADE, we have also noticed that ADE generation can find some useful application. In this respect, the chapter also shows how the direction of sweeping can be determined without using an optical spectrum analyser. This is important in determining the sweeping direction when employing resonant scanners, where a spectrum analyser cannot be used to check the sweeping direction. By observing which transitions in the B-scan due to the ADE are observed depending on the direction of lateral scanning, the direction of sweeping can be predicted. Hence this study shows that a simple method can be devised to establish the tuning laser direction, based on a lateral scanner and an interferometer only.

While the effects described in this chapter are not normally encountered in the SS-OCT practice, it is expected that they may be easier observed if more bidirectional sweeping lasers are developed, as the ADE is double to that of unidirectional sweeping sources. As the development of bidirectional lasers progresses, users should be aware of such errors introduced and image distortions, that may prevent accurate measurements of axial position of contours and image presentation of moving targets, such as blood molecules in vessels inspected by OCT Angiography.

References

1. Uceda, A. F., Venugopal, G. & Podoleanu, A. Spatial distortions in swept source optical coherence tomography due to lateral scanning. *Opt. Express* **32,** 22817–22836. `https://opg.optica.org/oe/abstract.cfm?URI=oe-32-13-22817` (June 2024).
2. Haeusler, G. & Lindner, M. W. "Coherence radar" and "Spectral radar"- new tools for dermatological diagnosis. *Journal of Biomedical Optics* **3.** Publisher: SPIE, 21–31. ISSN: 1083-3668, 1560-2281. `https://www.spiedigitallibrary.org/journals/journal-of-biomedical-optics/volume-3/issue-1/0000/Coherence-radar-and-Spectral-radar--new-tools-for-dermatological/10.1117/1.429899.full` (2023) (Jan. 1998).
3. Taplin, S., Podoleanu, A. G., Webb, D. J. & Jackson, D. A. Displacement sensor using channelled spectrum dispersed on a linear CCD array. en. *Electronics Letters* **29.** Publisher: Institution of Engineering and Technology, 896–897. ISSN: 1350-911X. `https://digital-library.theiet.org/content/journals/10.1049/el_19930598` (2023) (May 1993).
4. Golubovic, B., Bouma, B. E., Tearney, G. J. & Fujimoto, J. G. Optical frequency-domain reflectometry using rapid wavelength tuning of a Cr^{4+}:forsterite laser. EN. *Optics Letters* **22.** Publisher: Optica Publishing Group, 1704–1706. ISSN: 1539-4794. `https://opg.optica.org/ol/abstract.cfm?uri=ol-22-22-1704` (2023) (Nov. 1997).

5. Podoleanu, A. G., Dobre, G. M. & Jackson, D. A. En-face coherence imaging using galvanometer scanner modulation. EN. *Optics Letters* **23.** Publisher: Optica Publishing Group, 147–149. ISSN: 1539-4794. `https://opg.optica.org/ol/abstract.cfm?uri=ol-23-3-147` (2023) (Feb. 1998).

6. Podoleanu, A. G., Dobre, G. M., Webb, D. J. & Jackson, D. A. Coherence imaging by use of a Newton rings sampling function. EN. *Optics Letters* **21.** Publisher: Optica Publishing Group, 1789–1791. ISSN: 1539-4794. `https://opg.optica.org/ol/abstract.cfm?uri=ol-21-21-1789` (2023) (Nov. 1996).

7. An, L. & Wang, R. K. Use of a scanner to modulate spatial interferograms for in vivo full-range Fourier-domain optical coherence tomography. EN. *Optics Letters* **32.** Publisher: Optica Publishing Group, 3423–3425. ISSN: 1539-4794. `https://opg.optica.org/ol/abstract.cfm?uri=ol-32-23-3423` (2023) (Dec. 2007).

8. Hendargo, H. C., McNabb, R. P., Dhalla, A.-H., Shepherd, N. & Izatt, J. A. Doppler velocity detection limitations in spectrometer-based versus swept-source optical coherence tomography. EN. *Biomedical Optics Express* **2.** Publisher: Optica Publishing Group, 2175–2188. ISSN: 2156-7085. `https://opg.optica.org/boe/abstract.cfm?uri=boe-2-8-2175` (2023) (Aug. 2011).

9. Podoleanu, A. G., Taplin, S. R., Webb, D. J. & Jackson, D. A. Theoretical study of Talbot-like bands observed using a laser diode below threshold. *Pure and Applied Optics: Journal of the European Optical Society Part A* **7,** 517. `https://dx.doi.org/10.1088/0963-9659/7/3/013` (May 1998).

10. *Optical Coherence Tomography: Technology and Applications* en (eds Drexler, W., Fujimoto, J. G. & Greenbaum, E.) ISBN: 978-3-540-77550-8. `http://`

link.springer.com/10.1007/978-3-540-77550-8 (2023) (Springer, Berlin, Heidelberg, 2008).

11. Fingler, J. P. *Motion Contrast Using Optical Coherence Tomography* en. phd (California Institute of Technology, 2007). https://resolver.caltech.edu/CaltechETD:etd-05242007-121638 (2023).

12. Venugopal, G., Dobre, G., Chamorovskiy, A., Anikeev, A. & Podoleanu, A. *Development of a 850nm swept source based on a resonant scanner spectral filter* in *Optical Coherence Imaging Techniques and Imaging in Scattering Media V* **12632** (SPIE, Aug. 2023), 222–224. https://www.spiedigitallibrary.org/conference-proceedings-of-spie/12632/126321X/Development-of-a-850nm-swept-source-based-on-a-resonant/10.1117/12.2670660.full (2023).

13. Podoleanu, A. G. Optical coherence tomography. en. *Journal of Microscopy* **247.** _eprint: https://onlinelibrary.wiley.com/doi/pdf/10.1111/j.1365-2818.2012.03619.x, 209–219. ISSN: 1365-2818. https://onlinelibrary.wiley.com/doi/abs/10.1111/j.1365-2818.2012.03619.x (2023) (2012).

14. An, L., Subhash, H. M. & Wang, R. K. Full range complex spectral domain optical coherence tomography for volumetric imaging at 47 000 A-scans per second. en. *Journal of Optics* **12,** 084003. ISSN: 2040-8986. https://dx.doi.org/10.1088/2040-8978/12/8/084003 (2023) (July 2010).

15. Huang, D., Li, F., Shang, C., Cheng, Z. & Wai, P. K. A. Reconfigurable time-stretched swept laser source with up to 100 MHz sweep rate, 100 nm bandwidth, and 100 mm OCT imaging range. *Photon. Res.* **8,** 1360–1367. https://opg.optica.org/prj/abstract.cfm?URI=prj-8-8-1360 (Aug. 2020).

16. Pfeiffer, T., Petermann, M., Draxinger, W., Jirauschek, C. & Huber, R. Ultra low noise Fourier domain mode locked laser for high quality megahertz optical

coherence tomography. *Biomed. Opt. Express* **9,** 4130–4148. `https://opg.optica.org/boe/abstract.cfm?URI=boe-9-9-4130` (Sept. 2018).

Chapter 6

Outlook and further work

Throughout this thesis I have explored various scenarios in which axial displacements cause artefacts to OCT images, and how their severity in some scenarios can be detrimental to the application the device was designed for. Each source of artefacts requires its own considerations, which may determine the actions to be taken to correct them, when possible, as for high resolution imaging devices these artefacts can be a big limiting factor. These scenarios have been described with the handheld probe in chapter 3 and with the axial tracking system in 4, in which the motion, either from the sample or from the imaging device, was corrected with different approaches, catered to the specifics of the OCT devices.

Due to the constraints present in compact systems, like the handheld probe in chapter 3, software approaches with few modifications are preferred over mechanical or secondary detection systems, such as the solutions presented in chapter 4. While a second detection system can increase the precision of the motion correction, as well as reduce the processing time required for the calculation of the corrections, the added cost and complexity can be difficult to balance for some applications. Nonetheless, the flattening effect obtained with the approach in the handheld probe can also be desired in specific applications, such as dermatology and other medical conditions usually analysed through biopsies. In both chapters, the motion was a limiting hurdle that was successfully overcome, and while the tracking system would benefit from *in-vivo* testing for ophthalmological applications, the results were positive with the retinal model, and they lined up with those of the skin configuration, which worked in both *in-vivo* and with a mirror. The last barrier to be breached is the curvature of the surface combined with its specular properties, which requires more work on the optical design of the tracking subsystem to improve its reliability.

In line with the constraints of some applications, depending on the budget available for high resolution systems, there are modern advances in swept sources and cameras that, by increasing the acquisition speed, can reduce or mitigate the artefacts defined in chapters 3 and 4, but most commercially available sources still benefit from motion compensation as their acquisition speed is still comparable to the motion of living samples, especially at shorter wavelengths like 850 nm and below. Improvements in motion compensation could extend the usage lifetime of these devices, as well as allowing better results with low-cost OCT devices. While there is always room for improvement and research, the approaches discussed in those chapters are ready to be translated into industry, being able to be deployed as upgrading packages to different potential users in commercial applications.

However, one type of artefact, described in chapter 5, currently does not have a found correction. The nature of the artefact is complex enough that it depends on the sample under examination, and since we were the first ones to describe it, more research is necessary to fully comprehend the limitations and possible approaches depending on the application. For such a purpose, we performed preliminary experiments on other types of samples that should be expanded upon. The sample used in chapter 5 is a flat specular mirror, which reflects the light in an easy to predict fashion, so we could evaluate the deviation of the obtained signal from the expected one. More complex surfaces that are scattering rather than specular, having a closer resemblance to biological tissue, need to be examined. Therefore, I prepared a sample made by folding paper and adding a layer of tape on top, having a combination of scattering and specular sections. The experiment couldn't be fully finished, so the initial results were scrapped for this thesis, but the initial results seemed to indicate that the scattering layers not only displayed similar distortions, but also seemed to grow in thickness with a larger ADE. In the future, I'd like to be able to expand on this topic, evaluating properly the thickness and material used for the scattering layers so that the thickness variation can be measured correctly. Another interesting follow-up experiment would be the proper evaluation of irregularities in biological surfaces, since the sudden jumps on the surface would be magnified due to ADE, being able to measure the small initial variations accurately could help with early detection of different conditions, such as macular degeneration, in which drusen are formed in the inner layers of the retina that create bumps over the surface. This surface irregularities are also heavily present in angiography, in which the different veins and arteries produce mountains and valleys. It could be of interest to confirm if ADE alters any results predicted, such as blood flow or ischemic regions, as these two events would cause a sudden increase or reduction of the diameter of the blood vessels.

Other experiment which the preliminary results were omitted here consisted on corroborating the existence of ADE in SD-OCT devices. The preliminary results seemed to indicate that the SD-OCT devices do not experience the same ADE we perceive in SS-OCT. If this is to be confirmed, the ADE observed would be confirmed to be dependant on the sequential nature of a swept source, as the photodetector would detect the spectral signal one wavelength at a time. It would also present a strong benefit of SD-OCT over SS-OCT in some applications in which determining accurately the changes in the surface or the shape of the sample is crucial. In elastography, for example, could present different results for the same material in

SS-OCT than SD-OCT depending on the speed of the imaging, as the ripples experienced by the sample could have different thickness and heights in each setup. And current lines of research are employing AI to develop quick and precise diagnosis, if different techniques or optical designs experiment different ADE, the training data for these AI models could incur in over or underestimations of the severity of the disease. If ADE varies too much between systems, a method to control and minimise it would be necessary for these applications to reach a proper gold standard.

There is still much that we don't understand for the ADE presented in chapter 5, but while I could not come up with a solution when doing the research corresponding to these chapters, I do not discard the idea of a way to correct these artefacts. A possible approach could be first to obtain a calibration of the imaging system with a flat mirror, understanding the intrinsic ADE of the optical system. Secondly, we could stop the scanning at randomised points of the volume, obtaining consecutive A-scans with no motion at a particular point. This would give us a discrete shape of the surface, that combined with the calibration measurements, could compensate for follow-ups on that sample. Studying different interpolation options of the discrete shape of the surface could also be of interest, as it may render a realistic surface without any distortion at faster rates. Overall, the research on ADE has just started and I hope that the results presented on the paper that got published will impact the OCT community enough that other groups will not overlook these distortions, ensuing the correct development of further OCT technologies.

List of Figures